Simulation of evolving thermal conductivity in lithium ceramic breeder materials for nuclear fusion

Megha Sanjeev

This thesis is submitted for the degree of

Doctor of Philosophy

at Lancaster University

School of Engineering

July 2024

Simulation of evolving thermal conductivity in lithium ceramic breeder materials for nuclear fusion

Megha Sanjeev

Abstract

The effect of defects on heat transfer through plasma facing components must be predicted in order to make decisions about the materials which will be chosen and estimate their potential lifespan. The breeder blanket is particularly important for its three essential jobs: breed tritium *in situ*, defend the more fragile reactor components, and effectively transfer heat for eventual electricity generation. The thermal conductivity is a measure of the effectiveness of heat transfer through a material and can be calculated using atomistic simulation methods. This work focuses on a leading ceramic breeder material, Li_2TiO_3. It is expected that the inevitable radiation damage to the breeder blanket from the high-energy neutrons escaping the fusion plasma will affect heat transfer in the material.

In this thesis, the high anisotropy in the thermal conductivity of Li_2TiO_3 is shown, with the z-directions displaying much lower thermal conductivity than x or y. The mechanisms for accommodating non-stoichiometry in Li_2TiO_3 are investigated, and its effect on the thermal conductivity in scenarios of 1% Li excess and 1% Li loss. It is found that while there is a significant decrease in the thermal conductivity at room temperature, at higher temperatures the impact of deviations from stoichiometry is limited. The effect of voids and porosity is investigated, predicting that increasing porosity leads to a decrease in thermal conductivity. This is in good agreement with previous experimental observations. However, we do no observe the increase

in thermal conductivity at high temperatures that is observed in some experiments. Therefore, we argue that this increase is a consequence of sintering or some other modification of the experimental sample rather than a fundamental change in the heat conduction mechanism in the crystal matrix.

From these results we hope to contribute to estimates on the lifetime of a Li_2TiO_3 breeder blanket.

Acknowledgements

I would like to extend my deepest appreciation to the institutions and organisations that have supported me throughout my research journey. I thank Lancaster University and UKAEA for providing me with the resources necessary to embark on this project.

I am also very grateful for the significant computing resources utilised in this work. My thanks go to the HEC at Lancaster University for its reliable service, and to CSD3 at Cambridge for providing resources when needed. A profound thanks to the HEC MCC, and ARCHER/ARCHER2 for providing the computing power used to complete the bulk of the simulations in this thesis.

I extend my profound gratitude to the individuals who have supported and guided me throughout this journey. I owe my sincerest thanks to my supervisor, Samuel Murphy, for his unwavering support, mentorship, and invaluable insights. I also thank my second supervisor at CCFE, Mark Gilbert, for his guidance and encouragement. Their combined expertise and support have been crucial to the successful completion of this thesis.

My deepest gratitude goes to Gerry Courtney whose support and encouragement during my time in her secondary school science class left an indelible mark on my academic journey. The confidence and self-assurance she instilled in me enabled me to pursue Physics despite persistent prejudicial comments. I wish I could have expressed to her the profound impact she had on me while I had the chance. Thank you, Ms Courtney.

Special thanks to my colleagues in the Murphy Materials Modelling Group for

creating a wonderful academic environment. In particular, thanks to Becky for her warm welcome when I moved far from home for the first time, and a huge thanks to Jade for being my dearest friend and confidante for these past few years.

I would also like to thank my dearest friends Krishna and Nathalie, with whom I have had the honour of growing up from young undergrads to PhDs. Your constant love, support, and friendship have been invaluable.

I also extend my heartfelt thanks to my Amma and Acha, for always encouraging me to pursue my studies. Thank you for giving me everything I could need to succeed. Thank you to my sister Bhavya for always being there for me. Thank you to my Achamma, Apachi, and extended family for their encouragement and inspiration to strive in my educational pursuits. Thank you to my Achachan for giving our family the opportunities which allowed me to study at some of the top institutions in the world.

Finally, my deepest thanks to Jon for being my constant companion and support during this journey. I am so grateful to have you by my side.

Declaration

I hereby declare that this thesis is my own work and has not been submitted for the award of a higher degree elsewhere. Any sections of this thesis that have been published are clearly identified within the text.

Megha Sanjeev

July 2024

Table of Contents

List of Figures

List of Tables

List of symbols

A cross-sectional area xiii, 76

a vector acceleration 65–67

α thermal diffusivity 25, 133

A_{ij} potential parameter 71, 72

C heat capacity 25, 31

c specific heat capacity 25

c_{ij} potential parameter 71, 72

C_p heat capacity at constant pressure 135, 151

C_v heat capacity at constant volume 31

D deuterium 1, 2, 7, 13

D-D deuterium-deuterium 8

D-T deuterium-tritium 5, 6, 8, 16

E energy 68, 70–72

ϵ_0 permittivity of free space 70, 72

e elementary charge 73

F force vector 64

H hamiltonian 62, 64

H enthalpy 135

K kinetic energy 68, 69

k thermal conductivity 25, 27, 31, 79

k_B Boltzmann constant 68, 69

L thickness in the direction of heat flow xiii, xiv, xvi–xviii, 27, 76, 78, 79, 85–87, 89, 90, 94, 102, 103, 136, 138–141, 143, 145, 149, 150

l phonon mean free path 31

m mass 5, 25, 62, 64, 68, 135

N number of particles 62, 64, 68, 69

n neutron 8

P pressure 69

p momentum vector 62, 64

p proton 8

Q ficticious mass 69

Q heat energy 25, 36

q heat energy per unit area 27

q charge 70, 72, 73

r position vector 62, 64–67

r_{ij} the interatomic separation between two ions i and j 70–72

ρ material density 25, 31

ρ_{ij} potential parameter 71, 72

σ fusion collision cross-section x, 7, 10

T temperature xiii, 25, 27, 29, 36, 68, 69, 76, 85, 135

T tritium xi, 1, 2, 7, 13, 16, 18, 19, 37, 47, 48, 50, 51, 54, 55

t time 64–69

T_D the Debye temperature 29

U potential energy 62, 64, 68, 69, 72

V volume 68

v velocity vector 62, 65–67

v velocity 31, 68

List of abbreviations

BZ Brillouin zone xi, 33, 34

DEMO Demonstration power plants xi, 7, 11, 18, 20, 37

DFT Density Functional Theory 33, 47, 48, 59, 73, 96, 100, 104, 105, 107, 109, 157

DIII-D Doublet III-D 7

HCPB Helium-Cooled Pebble Bed xi, 18, 20, 50, 159

HF Hartree-Fock 59

HLW High-Level Waste 6

ITER International Thermonuclear Experimental Reactor xi, 7, 11, 14, 18, 37, 159

IUPAC International Union of Pure and Applied Chemistry 119

JET Joint European Torus 7, 11

LAMMPS Large-scale Atomic/Molecular Massively Parallel Simulator xvi, 62, 102, 137, 139

LHD Large Helical Device 12

MAST Mega Ampere Spherical Tokamak 7, 11

MD Molecular Dynamics 26, 48, 59–62, 64, 67, 70, 72, 73, 75, 77, 83, 99, 101, 102, 109, 128, 132, 133

NEMD Non-Equilibrium Molecular Dynamics xiii, 75, 85, 90, 116, 136, 156

NIF National Ignition Facility 7, 12

NPT constant pressure and temperature xiii, xviii, 68, 69, 75, 77, 83, 102, 133, 153

NVE constant volume and energy 68, 77, 83

NVT constant volume and temperature 68, 75

OVITO the Open Visualization Tool xv, xvi, 120, 121, 134, 137, 139

PKA primary knockon atom 48, 49

ST40 Spherical Torus 40 7

STEP Spherical Tokamak for Energy Production 11

TBM Test Blanket Module 18, 37, 159

TBR tritium breeding ratio 14, 50, 99

TD theoretical density 50, 51, 53, 54, 56, 57, 96

TFTR Tokamak Fusion Test Reactor 11

1

Introduction

The potential for producing large quantities of low carbon energy has made the prospect of fuelling the world using fusion power an attractive concept. As nations across the world strive toward carbon neutrality and sustainable development goals, fusion energy emerges as an indispensable component of the transition to cleaner energy production and, in turn, a cleaner and brighter future. The achievement of fusion energy would mark a turning point in the pursuit of sustainability, offering a clean and near-limitless source of power. Unlike fossil fuels, fusion produces minimal waste and does not emit greenhouse gases, thereby mitigating the detrimental effects of climate change. Its potential to provide abundant and reliable energy without reliance on finite resources or further contributing to environmental degradation is crucial to ensuring energy security and in turn reducing geopolitical tensions over energy access.

Fusion reactors use fuel in the form of two hydrogen isotopes, deuterium (D) and tritium (T). D has a small natural abundance, sufficient to fuel a fleet of fusion reactors, and can be easily extracted from seawater. Naturally occurring T, however, is very rare. The scarcity of tritium poses a significant challenge in the development of a viable fusion reactor. With prices for tritium exceeding $25,000 per gram [1], obtaining sufficient tritium for sustained operation is a considerable obstacle. To

achieve long-term functionality, a fusion reactor must therefore produce its own tritium once receiving a seed supply. Extensive research efforts have been made to address this crucial aspect of fusion reactor technology with estimates of ∼10 kg of seed tritium still being required for each proposed reactor design, leaving the T problem in two parts: obtaining the seed T, and breeding T *in situ* within the reactor itself [1]. Tritium breeding is achieved using a breeder material, typically containing lithium. The plasma in a fusion reactor is then surrounded in a blanket of this material. This module is called the breeder blanket [2].

In the plasma, D and T fuse together to produce an alpha particle and a neutron. The neutrons produced are not constrained by the magnetic field due to their lack of charge; therefore, they escape the plasma and enter the blanket where they can transmute lithium atoms to produce another alpha particle and tritium. This tritium is then extracted from the blanket, reprocessed and fed back into the plasma. The tritium reaction-creation life-cycle within fusion systems is illustrated in Fig. 1.1. The breeder blanket also serves as the channel for energy conversion in the reactor, transforming the kinetic energy of the neutrons into heat (along with producing an additional energy multiplication factor between 1.2 and 1.3 themselves via nuclear reactions [3]) to generate the electrical output of the reactor [4]. Hence, the overall electrical generating efficiency of a reactor is strongly tied to the effectiveness of heat transfer through the breeder blanket.

The final role of the blanket module is to act as a shield, preventing the high-energy neutrons from damaging other components of the reactor, in particular the superconducting magnets used for the plasma confinement [3] and the vacuum vessel, which must last for the entire life of a reactor and is the primary safety barrier [5]. Therefore, the breeder blanket must withstand the extreme conditions inside the reactor, where materials are exposed to high-energy neutron irradiation and incorporation of transmutation products, which must not compromise the integrity or efficiency of the reactor, in order to achieve sustainable long-term fusion.

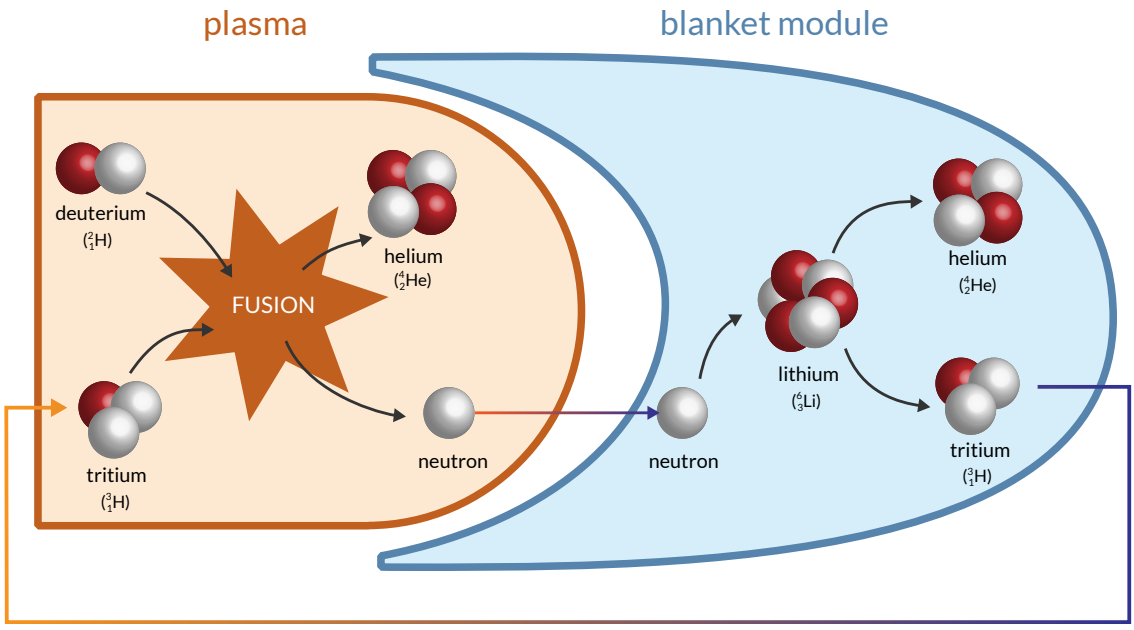

Figure 1.1: Schematic diagram of how tritium is bred inside a fusion reactor by using a breeding blanket containing lithium. The fusion reaction between the deuterium and tritium fuel produce an alpha particle and a high energy neutron, which escapes the plasma and enters the blanket module. These neutrons transmute Li atoms in the blanket to produce an alpha particle and tritium. This tritium is extracted from the blanket and fed back into the plasma.

It is possible, and indeed likely, that this neutron irradiation will reduce heat transfer through the breeder blanket, directly reducing the energy that is harvested from the reactor. It is therefore essential to understand how heat transfer is affected by various possible damage scenarios in order to choose the breeder blanket design itself, and to estimate any required reactor maintenance. Therefore, it is necessary to know the thermal conductivities of all of the materials contained in the blanket, and how these may evolve during reactor operation.

Thermal conductivity is a direct measure of how well heat is transferred through the material. To estimate the effect of radiation damage on the blanket module, we turn to simulation to allow us to link the atomic scale features of the material to its macroscopic thermal conductivity. With the use of simulation, we are able to model the effects of particular defect types and understand the intrinsic effects on heat transfer through the material by studying it on the atomic scale. This also allows the investigation of separate effects and their impact on the thermal conductivity, which cannot necessarily be isolated using experiment alone.

There are multiple ideas in development for the design of the breeder blanket module. One of the most popular is the use of lithium ceramics in the form of pebbles, which are then located in pebble beds in the blanket. There are several candidate lithium ceramics currently being investigated. This thesis focuses on one of the leading candidates, Li_2TiO_3, for its many benefits, which are discussed in the next chapter.

The objective of this thesis is to develop a model to predict how the thermal conductivity of Li_2TiO_3 changes during reactor operation, by modelling the different defect scenarios. As a starting point we develop a model for the idealised Li_2TiO_3. We then move on to examine how changes in the stoichiometry of the crystal, arising from Li burn-up, degrade the thermal conductivity. Finally, we explore how heat transfer is impacted by the introduction of porosity, initially focusing on individual voids, and then using a more representative random distribution of voids.

2

Literature review

2.1 Fusion reactors

Nuclear fusion is the counterpart of the more widely employed nuclear fission. In nuclear fission heavy nuclei, such as uranium, are split apart, releasing energy in the process. In contrast, nuclear fusion combines light elements together, merging them to form heavier elements. In the case of fusion, the positively charged nuclei must be brought sufficiently close together to enable the short-range nuclear strong force to bind the large nucleus together. This requires the ions to overcome the electrostatic repulsion between them, which requires heating the nuclei to extremely high temperatures so that the kinetic energy of the particles is high enough. In the case of D-T reactions, the required temperature is ∼10 keV (∼100 million °C) [6, 7].

In both nuclear processes, it is the reduction in the mass of the products that is released as energy. This is due to the conservation of energy, as well as mass-energy equivalence as described by Einstein's famous equation, $E = mc^2$, where, the energy released, E, is equal to the mass, m, times the square of the speed of light, c. The binding energy per nucleon is lowest for very light and very heavy nuclei, with highest binding energy for nuclei of mass ∼60 amu (see Fig. 2.1). The amount of energy released during a fusion reaction is significantly greater (by a factor of

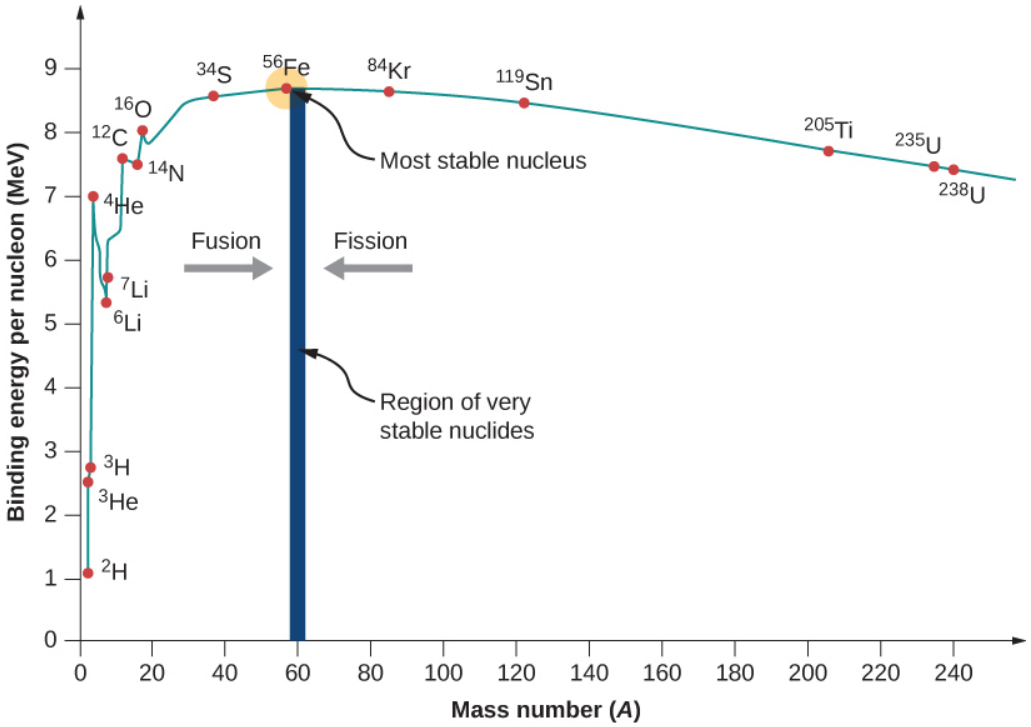

Figure 2.1: Binding energy per nucleon as a function of atomic mass number. The regions in which energy production is possible from fusion or fission are indicated. Figure from [8].

$\sim 10^6$) than that released by chemical reactions. This is due to the fact that the binding energy holding the nucleus together is much greater than the energy that binds atoms and molecules together through electronic bonds. For example, the energy required to ionise a hydrogen atom by stripping a single electron is 13.6 eV, compared to the 17.6 MeV released by the D-T reaction [7]. Another important factor in favour of fusion reactors is that unlike nuclear fission reactors, there is no risk of uncontrollable reactions of nuclear meltdowns as are possible and infamous in fission reactors [6]. Furthermore, careful consideration in the choices for reactor components and structural materials will allow fusion reactors to avoid producing High-Level Waste (HLW); limiting radioactive waste to Low-Level Waste (LLW) and Intermediate-Level Waste (ILW). HLW, requires very careful long-term disposal due to its high radioactivity and significant heat generation. However, the total volume of radioactive waste produced by fusion power remains significant, and comparable to fission reactors [9].

The Sun is powered by the slow thermonuclear fusion of protons (p-p reactions), where the immense gravitational force, due to its large mass, is sufficient to counteract thermal expansion. On Earth, uncontrolled fusion reactions in the form of thermonuclear explosions have been achieved, thus, proving the possibility of generating significant energy via fusion. However, it is not possible to reach a high enough mass on Earth to mimic the Sun and other stars, making gravitational confinement impractical for a reactor. Therefore, the challenge lies in achieving controlled fusion in a confined plasma, which can then be used for electricity production. Steady progress has been made over the years in fusion research, with the National Ignition Facility (NIF) even reaching the break-even condition of outputting energy greater than the required input energy to initiate the reaction [10]. Over the course of the last few decades, numerous fusion experiments have been constructed and extensively studied, including JET [11], DIII-D [12], MAST [13], and ST40 [14], with construction in process on future fusion experiment, ITER [15], and design and development already underway on its successors, DEMO [16].

An essential part of the recipe for fusion, D, is abundant in nature, comprising 0.015% of the hydrogen found in seawater as heavy water (D_2O), with a volume of $\sim 1.35 \times 10^9\,\mathrm{km}^3$ [6]. This is enough to be considered inexhaustible for use in energy generation by fusion [7]. However, T is naturally extremely rare, due to its short half-life of $\sim$12.6 years limiting its natural accumulation. Though pure D fusion is possible, the smaller fusion cross-section means that successful exploitation is more difficult (see Fig. 2.3). The fusion cross-section, or fusion collision cross-section, is the effective size of a particle in a collision, i.e., it is the probability that a fusion reaction will occur.

The relative abundance of D has the added benefit of improving accessibility to all countries, compared to the uneven distribution of fossil fuel sources, which has led to many disputes in humanity's history.

The collision cross section, σ, is a function of the energy of the ions in the

proposed reaction. Combined with the velocity, v, of the ions, the fusion reaction rate is defined. By including in the density of ions, the probability of fusion reactions per unit time is defined (see Fig. 2.3). Some of the largest cross section fusion reactions in consideration for use as fuel in fusion reactors are listed in Eqs. 2.1 to 2.4, alongside the energy produced by each reaction (where the energy of the products is inversely proportional to the mass of the products, leading to high-energy neutrons) [6, 7].

$$\mathrm{D} + \mathrm{T} \longrightarrow {}^{4}\mathrm{He}\,(3.52\,\mathrm{MeV}) + \mathrm{n}\,(14.06\,\mathrm{MeV}) \tag{2.1}$$

$$\begin{aligned} \mathrm{D} + \mathrm{D} &\longrightarrow \mathrm{T}\,(1.01\,\mathrm{MeV}) + \mathrm{p}\,(3.03\,\mathrm{MeV}) \\ &\longrightarrow {}^{3}\mathrm{He}\,(0.82\,\mathrm{MeV}) + \mathrm{n}\,(2.45\,\mathrm{MeV}) \end{aligned} \tag{2.2}$$

$$\mathrm{D} + {}^{3}\mathrm{He} \longrightarrow {}^{4}\mathrm{He}\,(3.67\,\mathrm{MeV}) + \mathrm{p}\,(14.67\,\mathrm{MeV}) \tag{2.3}$$

$$\mathrm{T} + \mathrm{T} \longrightarrow {}^{4}\mathrm{He} + 2\mathrm{n} + 11.3\,\mathrm{MeV} \tag{2.4}$$

where, p is a proton (hydrogen ion) and n is a neutron.

The D-T reaction, shown in Eq. 2.1, is widely considered the most promising for use in the first fusion reactors. It produces a significant amount of energy and has a relatively low ignition temperature, as determined by the Lawson criteria [17], compared to other reactions (see Fig. 2.3). Eq. 2.2, describing D-D fusion, is also attractive due to the abundance of D. However, the higher temperature and pressure requirements make it more difficult to achieve. There is also the added complication of two possible reactions each with 50% likelihood meaning that both must be taken into account. The aneutronic D-^{3}He reaction is also attractive, for its reduced risk of radioactive products due to producing charged protons as opposed to neutrons. However, ^{3}He is also extremely rare. It has been proposed that ^{3}He could be harvested extraterrestrially, e.g. from the moon [18]. This may make this reaction viable for future generations of reactors.

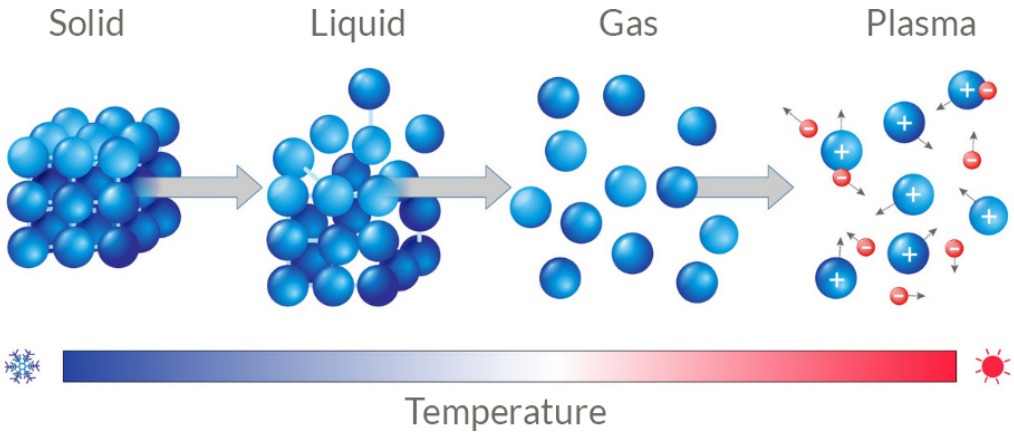

Figure 2.2: The four states of matter, illustrated by their respective arrangement atoms or ions, in order of increasing temperature i.e. increasing energy. Figure from [19].

In order for fusion to occur, the fusion fuels must be subjected to high temperatures and pressures, which transforms them into a plasma. Plasma is the fourth state of matter after solid, liquid, and gas (see Fig. 2.2). By increased heating and, therefore, reaching the ionisation of gas, we obtain plasma, which is made up of positively and negatively charged particles [20]. For this reason, plasma is often referred to as an ionised gas, although its properties differ from those of gas in several important ways because of its charged nature. Unlike gases, the presence of free charge carriers make plasmas highly conductive, with theoretically infinite conductivity. In addition, long-range Coulomb interactions of charged particles are highly influential on the entire plasma, leading to collective motion such as waves through the plasma. Plasma is similarly also influenced by magnetic fields. It is the highest energy state of matter and its high temperatures are what cause, or rather allow, nuclear reactions to occur [20]. In a fusion reactor, the fusion process takes place in a contained plasma, made up of chosen fuels.

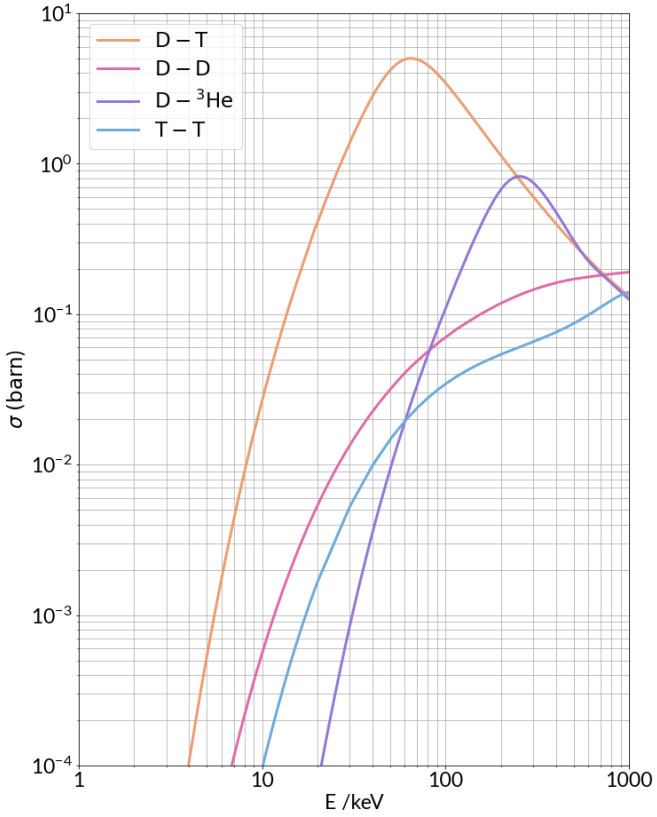

(2.3a)

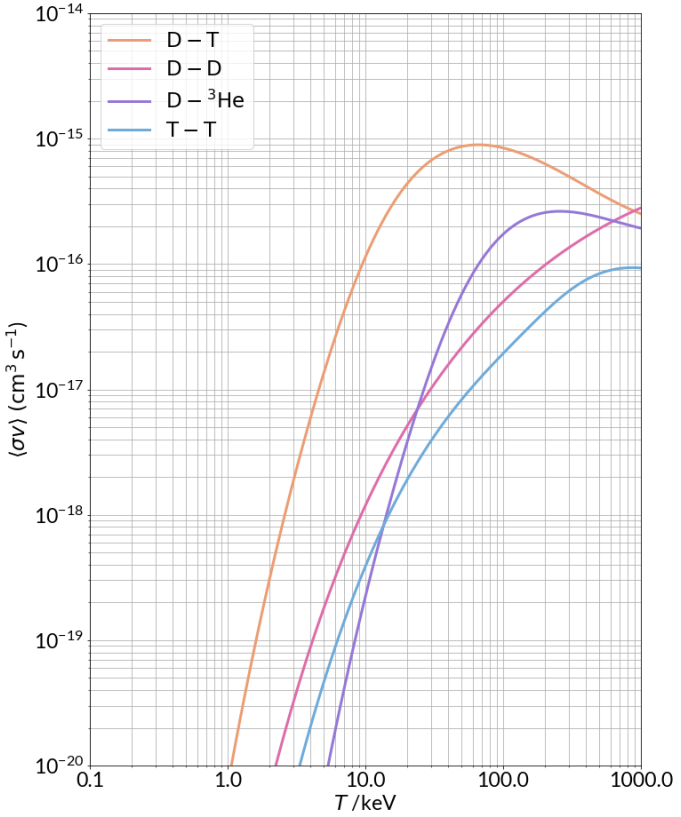

(2.3b)

Figure 2.3: a) The dependence of the fusion cross section, σ, on the kinetic energy E of colliding nuclei and b) the dependence of the fusion rate, $\langle \sigma v \rangle$, on the ion temperature T. Figures generated using data from the Evaluated Nuclear Data File (ENDF) [21]. (1 barn = 10^{-24} cm^2)

The field of fusion energy research is highly dynamic and new advancements in reactor designs are constantly emerging. The extreme temperatures required to achieve a plasma state make reactor designs complex engineering challenges due to the fact that no material can touch the plasma or it will be destroyed as well as pollute the plasma. There are several proposed reactor designs, which are largely defined by the method of plasma confinement, i.e. magnetic or inertial.

Magnetic confinement devices exploit the Lorentz force experienced by charged particles in a magnetic field to contain the plasma and prevent it from cooling by dispersing. The most widely researched and developed reactor design is a magnetic confinement device called the tokamak. Some of the most notable uses of the tokamak concept are JET [11], at Culham Centre for Fusion Energy (CCFE) in the UK, and TFTR [22], at Princeton Plasma Physics Laboratory (PPPL) in the USA. Currently, the world's largest tokamak fusion reactor, ITER [15], is under construction in France as a collaboration between 35 countries. With the aim to build on the findings of ITER, its successor DEMO [16], a fleet of reactor experiments, is already in the design phase. All of these experiments use the conventional tokamak design, which is toroidal. Tokamaks generate energy from fusion reactions in the volume of the plasma and lose energy from the surface. Therefore, by increasing the volume to surface area ratio of the tokamak by increasing its size, it becomes easier to keep energy in the plasma. A relatively new variation on the tokamak is the spherical tokamak, which has a more compact design and has magnet arrangement with a much greater aspect ratio and a smaller central column as shown in Fig. 2.4. The plasma is formed into a rounder 'cored-apple' shape compared to the torus or 'doughnut' shape in conventional tokamaks. MAST [13] and MAST Upgrade in the UK are examples of a spherical tokamak experiment, with STEP [23] to follow.

Another design using magnetic confinement is the stellarator, a more complex magnet design that uses superconducting magnetic coils in a mainly toroidal formation to induce a helical magnetic field which allows for a steady-state plasma and longer

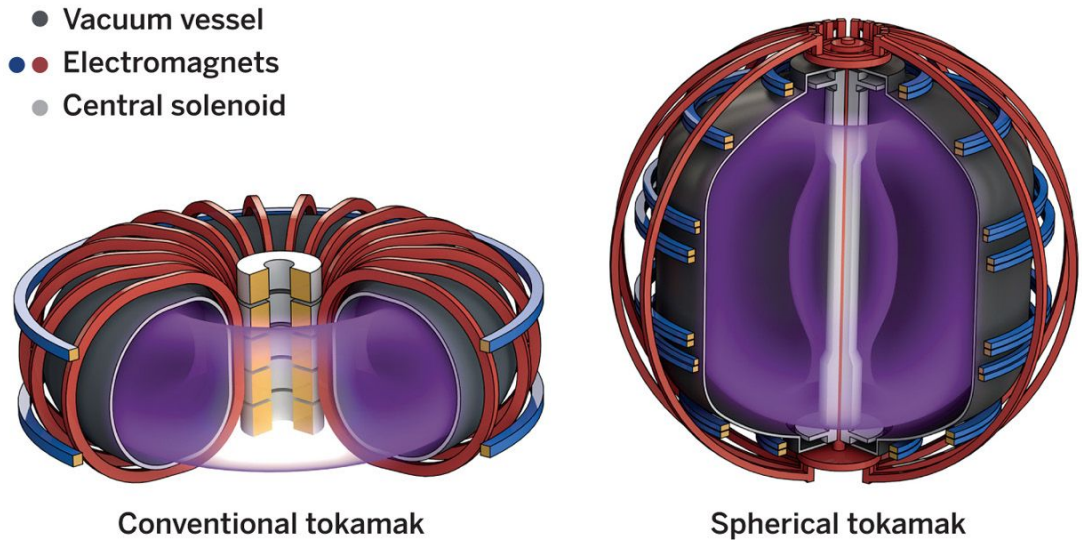

Figure 2.4: Comparison of conventional and spherical tokamak reactor designs. Figure from [24].

plasma confinement time. Large stellarator work includes the LHD [25] in Japan and the Wendelstein 7-X (W7-X) [26] in Germany. However, most fusion research follows the tokamak because of its relative ease and safety for research and testing.

Inertial confinement fusion is the leading alternative to magnetic confinement. It employs the use of an intense laser or pulse of heavy ion beams to compress and heat a small hollow fuel pellet. This compression generates the high pressure and temperature required for fusion to occur. Because of the inertia of the hot fuel, confinement is achieved for a finite time. The NIF in the United States holds the record as the largest operational inertial confinement fusion experiment. However, inertial fusion plasmas produce pulsed energy compared to the near steady state energy produced by magnetic concepts [7]. This can make electricity generation more difficult compared to a continuous process. However, while stellarators could be fully continuous, tokamak reactors will likely still produce pulsed energy to some extent, due to induced current being pulsed.

The work presented in this thesis is guided by research on the leading reactor concept: tokamak fusion reactors, and considers tokamak reactor designs and the

material engineering requirements for tokamak reactor components.

2.1.1 Anatomy of a tokamak fusion reactor

The tokamak fusion reactor is composed of several critical components that work together to confine and regulate the plasma, with the goal of encouraging the fusion process (see Fig. 2.5). In a tokamak, the plasma is enclosed in the vacuum vessel, which is a toroidal chamber made of strong material, such as steel, that can withstand high temperatures and maintain a low-pressure vacuum environment. The plasma is shaped and controlled by strong magnetic fields induced by field coils made of superconducting materials, each carrying a very large current. The combination of toroidal and poloidal fields results in helical magnetic field lines through the plasma, which is confined to a toroidal shape [6]. The D and T fuel is inserted as a gas and heated until it forms a plasma. A central solenoid is used to manipulate the induced magnetic fields to generate and control a strong electric current in the plasma. This central column together with the plasma act as a transformer. This electric current increases the activity of the electrons and ions, ultimately leading to an increase in the temperature of the plasma through a phenomenon known as Ohmic heating. In addition, other heating methods are used to create the optimal conditions required for the fusion of deuterium and tritium ions into helium. Common heating methods include electromagnetic radiation or neutral beam injection [6].

The divertor is situated at the bottom of the tokamak and plays a role in safeguarding the vacuum vessel walls from excessive heat and particle flux by extracting heat as well as He ash and other impurities from the plasma, which also minimises possible plasma contamination [6]. The inner walls of the vacuum vessel are protected by the blanket module from high-energy neutron irradiation. The neutrons are slowed by the blanket, transforming their kinetic energy into heat, which is then collected by the coolant between the double walls of the vacuum vessel. The blanket, divertor, and first wall are plasma-facing components, which makes the engineering to satisfy

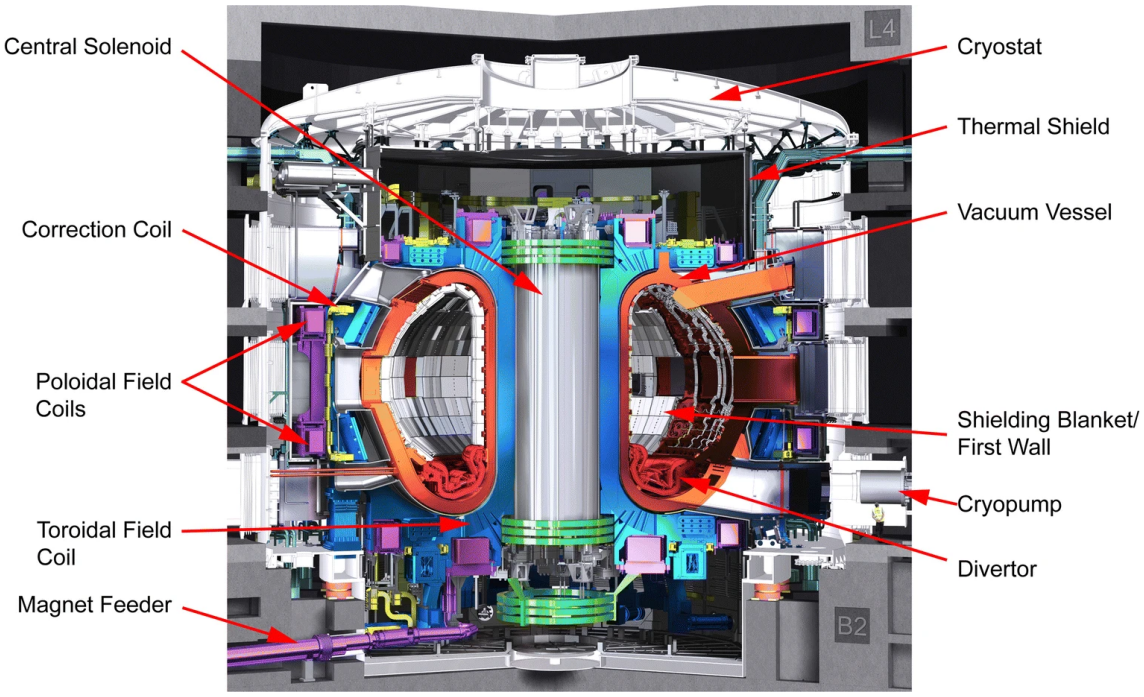

Figure 2.5: Cutaway diagram of the ITER tokamak, showcasing the primary components. The cryostat, which measures ∼29 m both in diameter and height, is also indicated. Figure from [27].

all requirements particularly challenging [6].

As well as heating systems for the plasma, cooling systems are required to dissipate the generated heat in the plasma facing components and ensure the magnets remain at superconducting temperatures. This is done by circulating coolants such as water or helium to remove excess heat. This must work to maintain the reactor components at their operating temperatures. The heat that is carried away is what will be used to generate electricity [6].

2.1.2 Breeder blankets

There are numerous properties that are either necessary or desirable for breeder blanket designs, the most important of which is the ability to offer a high tritium breeding ratio (TBR). The TBR is the ratio of the amount of tritium produced in the blanket relative to the amount that is used in the plasma. This is essential for

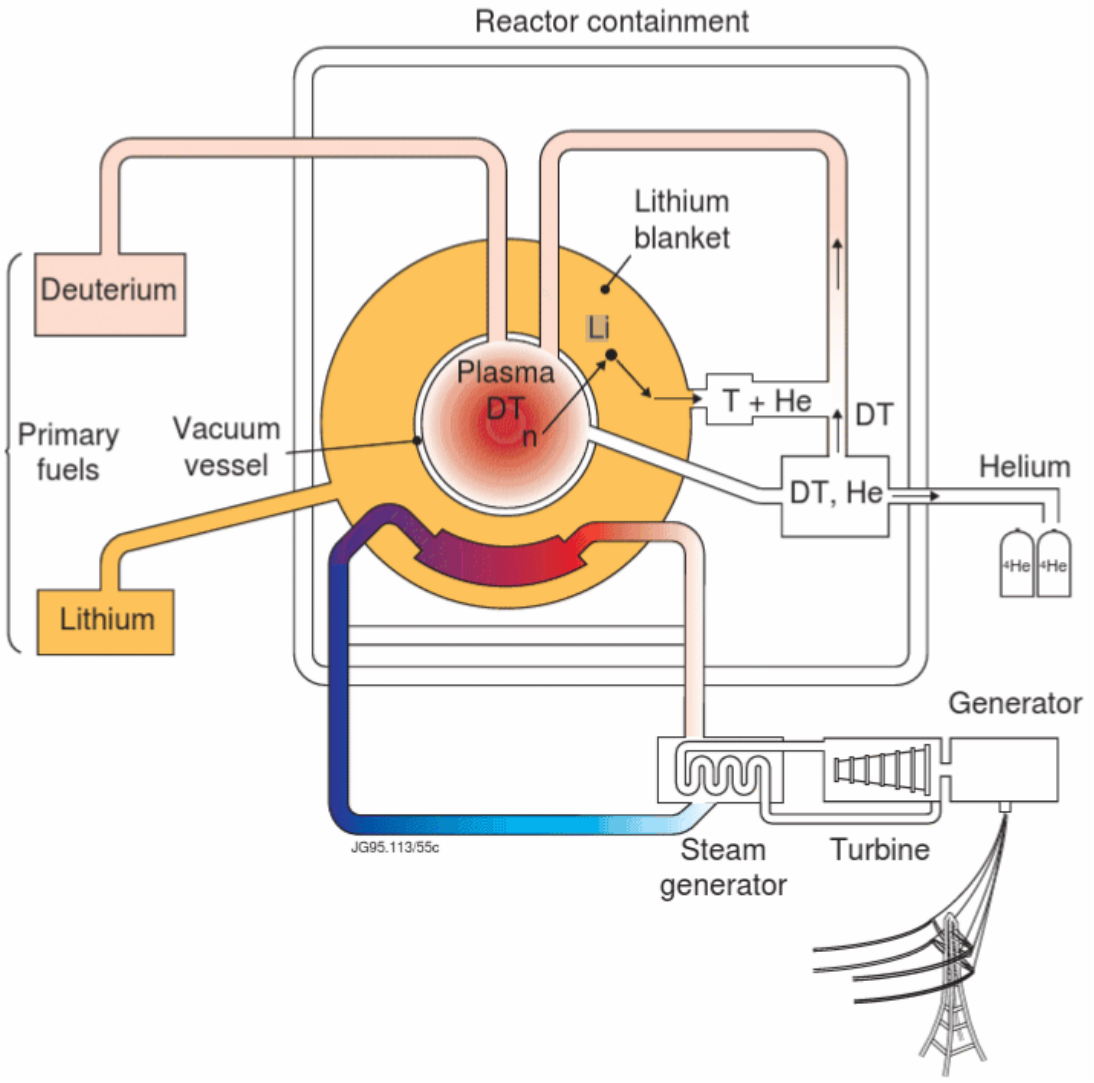

Figure 2.6: Schematic diagram of a proposed nuclear fusion power plant. The nuclear energy is converted to usable energy using a conventional stream-generating plant. The waste product of the reactor is helium. Figure from [28].

achieving self-sustaining fusion.

The breeder blanket also serves an important role in the electricity generation of the reactor. The kinetic energy from the neutrons that escape from the plasma is absorbed by the blanket and transferred through it as heat to the coolant, which can then be used in conventional means of energy production, such as heating water to produce steam to turn turbines in a generator and produce electricity (see Fig. 2.6). Therefore, the efficiency by which the blanket transfers heat is key to the efficiency of electricity generation. Therefore, the thermal conductivity of the blanket should be high to maximise the efficiency of the reactor.

There are a number of isotopes that can use the neutron released by the D-T reaction to produce more tritium. Among these, the associated high safety and security risks, mean that alternative T breeding pathways using thorium or uranium are largely discarded from design concepts, leaving lithium as the leading T breeder. ^{6}Li is an isotope of Li, with a large neutron capture cross-section, making it the ideal choice for T breeding (Eq. 2.5). The neutron capture cross-section, serves as a measure of the probability of a nucleus capturing an incoming neutron during a collision or interaction. This measurement quantifies the likelihood of a neutron being absorbed by a target nucleus, thereby resulting in the creation of a new nucleus.

Lithium-based materials also exhibit low activation levels, producing only short-life radioactive waste. This simplifies waste management and concerns about long-term environmental effects. ^{7}Li can also be used to breed T (Eq. 2.6), but has a lower cross-section, making reactions less likely than that of ^{6}Li.

The exothermic Eq. 2.5 is preferred, due to the higher probability of reaction compared to Eq. 2.6, but natural lithium abundance is 92.6% ^{7}Li and 6.4% ^{6}Li. This leads to the proposal of designs with lithium enrichment, that is, with an improved proportion of ^{6}Li compared to ^{7}Li, called advanced lithium ceramics. The T breeding efficiency can be improved through a variety of methods. The most effective is to raise the Li density. Different Li-based materials have different amounts of Li. The

higher the ^{6}Li content, the more likely breeding reactions will take place.

$$^6\mathrm{Li} + \mathrm{n} \longrightarrow {}^4\mathrm{He} + \mathrm{T} + 4.8\,\mathrm{MeV} \tag{2.5}$$

$$^7\mathrm{Li} + \mathrm{n} \longrightarrow {}^4\mathrm{He} + \mathrm{T} + \mathrm{n} - 2.5\,\mathrm{MeV} \tag{2.6}$$

Neutron moderators, can improve efficiency by moderating, i.e. slowing, the high-energy neutrons so that the breeding reactions are more likely. Similarly, neutron multipliers increase the number of neutrons available for reactions and also moderate fast neutrons into two slower neutrons. Beryllium is an example of both, making it a versatile choice. However, it is largely avoided due to its high toxicity. The ^{6}Li in the breeder material itself also serves as a neutron moderator.

Numerous concepts for breeder blanket designs have been considered. The most common designs can be grouped into either solid and liquid blanket concepts. Liquid blanket concepts, such as the Helium-Cooled Lithium Lead (HCLL) design, employ a liquid lithium-lead (Li-Pb) eutectic as the breeder and multiplier material [3, 29, 30]. This concept benefits from high thermal conductivity. However, the circulation of liquid metals through magnetic fields presents specific challenges due to magnetohydrodynamic effects. Conflicting fields can lead to dead points in the blanket, leading to inefficient heat transfer. Solid blanket designs employ a solid breeder material, typically a lithium ceramic [31]. Lithium ceramics are attractive because of their high lithium density, which allows for higher breeding ratios. In addition, these materials have low chemical reactivity, making them more easily compatible with the materials used in other reactor components, as well as with the various coolants and neutron multipliers that are being considered. However, ceramics have lower thermal conductivities compared to liquid options, leading to lower energy conversion efficiency. Solid concepts can be in the form of sintered pellets or slabs, or more commonly small pebbles. The latter designs are known as pebble bed concepts. The

two most common examples of these being Helium-Cooled Pebble Bed (HCPB) and Water-Cooled Pebble Bed (WCPB), which, as their names suggest, are differentiated by the coolant used. However, solid blankets are subject to radiation damage, which may impact their tritium release characteristics and also limit their lifetime in the reactor. Testing of a selection of T breeding concepts will be done during ITER operation in the form of Test Blanket Modules (TBMs).

2.1.3 Ceramic blanket designs

Designs for ceramic breeder blankets focus on the use of small spherical pebbles of solid lithium ceramic, typically ranging from ∼0.5–2.0 mm in diameter. This is done to reduce the thermal stress in the breeder material from the high thermal loads expected, as well as to prevent the pebbles from being crushed in the blanket module. The small pebble size as well as the space between them helps with efficient tritium extraction from the pebble bed because the tritium can diffuse to the surface of the pebbles and then easily travel through these spaces (see Fig. 2.7). Structural failure of the ceramic would impede this extraction. An alternative option of using large blocks of material would make tritium extraction more difficult because of the increased distance the tritium would have to diffuse through the material. Additionally, maintenance of pebbles is simpler than replacing an entire larger slab [31].

As well as the ceramic breeder, most concepts envisage a neutron multiplier to increase breeding efficiency. A depiction of the DEMO HCPB is seen in Fig. 2.8. Here, we see an example of a lithium ceramic being used alongside a beryllium neutron multiplier. The Be is also in pebble form.

Selection of the leading candidate material and development of the actual breeder blanket requires the ability to predict how the materials evolve during operation, where they will be exposed to high heat fluxes (with temperatures expected to be in the range 300–950 °C [33]) and irradiation by high-energy neutrons. Most importantly, it is necessary to be able to estimate how the key physical properties of

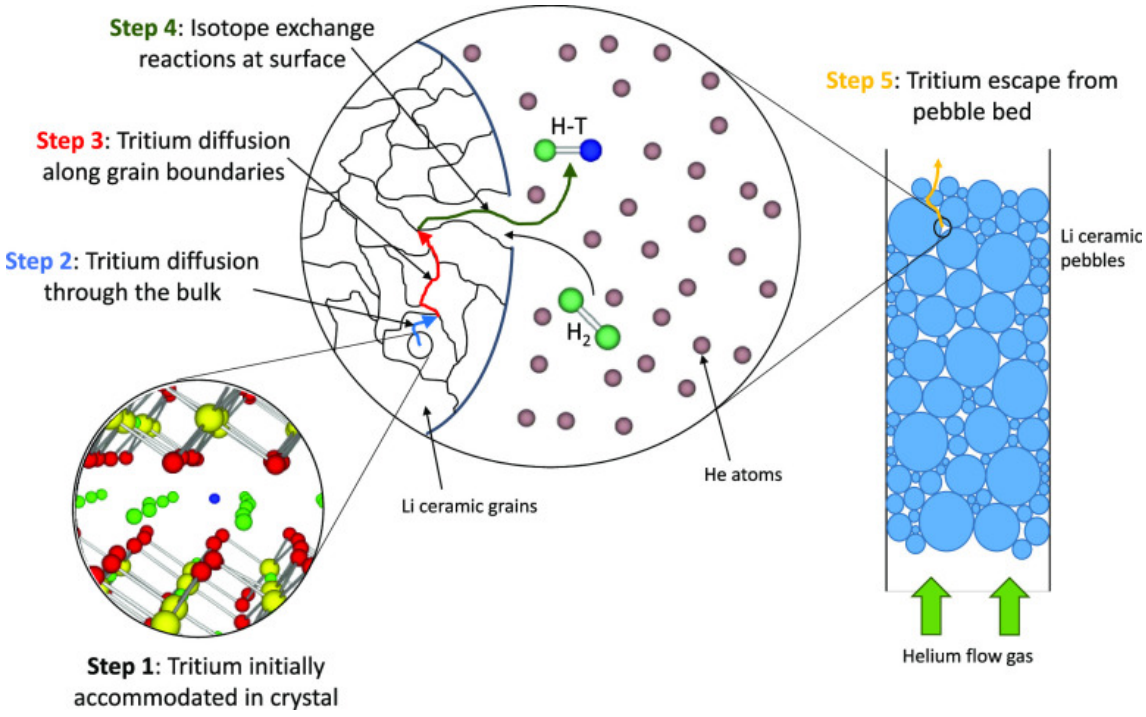

Figure 2.7: Diagram depicting the procedure involved in the T release mechanism from lithium ceramic pebbles within the breeder blanket using a He purge gas. Figure from [32].

the materials will change during operation.

The safe operation of a future reactor is highly dependent on a thorough understanding of how the characteristics of crucial functional materials evolve throughout its operation. As such, it is important to understand how thermal conductivity changes over time. The thermal conductivity of the blanket is a function of the thermal conductivity of the lithium ceramic pebbles themselves. Degradation in thermal conductivity may lead to temperatures in the blanket exceeding maximum allowable limits. Further, extensive degradation in the thermal conductivity could increase thermal stress in the pebbles, leading to fragmentation. Therefore, in this work we analyse the thermal conductivity of Li_2TiO_3, with the aim to describe the thermal conductivity of the entire module.

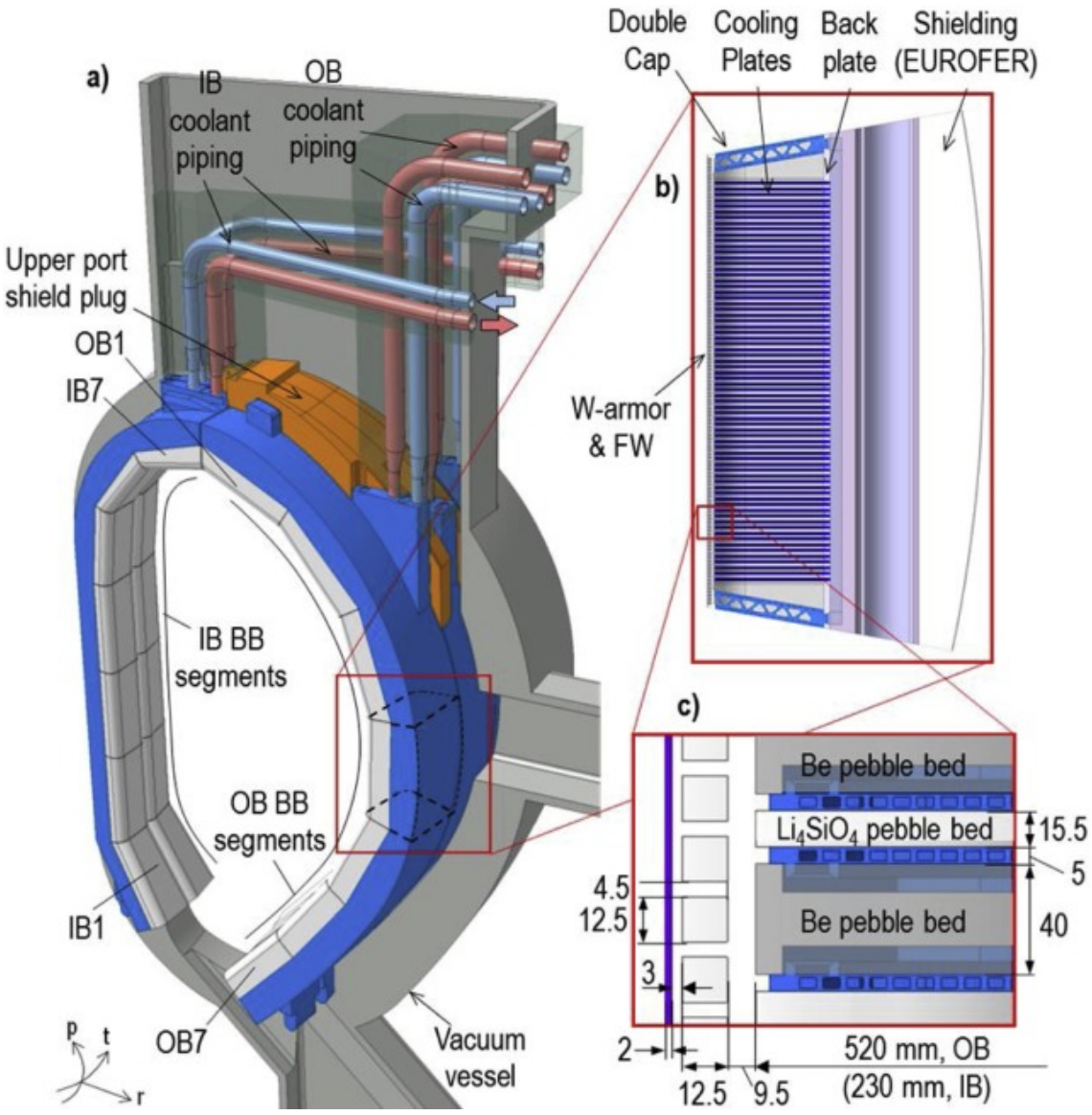

Figure 2.8: A depiction of the DEMO HCPB design from three different views: a) an elevation view which displays two inward and three outward segments per sector, b) a toroidal cross-section of the blanket is shown which highlights the breeding region at the front and the shielding region at the back, c) a detailed view of the ceramic breeder and Be multiplier elements located in the breeding blanket region. Figure from [3].

2.2 Thermal conductivity

2.2.1 Theory of heat transport

The theory of heat transport is fundamental in the field of thermodynamics and describes the movement of thermal energy from one region to another. Heat is the thermal energy transferred when there is a temperature difference between two bodies or regions. Heat naturally flows from the hotter region to the colder region until thermal equilibrium is achieved. From a macroscopic perspective, the primary mechanisms of heat transport are conduction, convection, and radiation [34].

Conduction is the transfer of heat through a material through direct contact between particles. Heat energy is transferred from higher-energy particles to lower-energy particles through elastic collisions. This creates a flow of heat energy through the material. Conductors are materials which allow the flow of electric current through their free electrons. These free electron transfer kinetic energy, and therefore heat, throughout the material. Conversely, the electrons in an insulator being tightly bound to their atoms, inhibiting the flow of electric current.

Convection is the transfer of heat through the bulk motion of a fluid, which may be in liquid or gas form. When a fluid is subjected to heating, its constituent particles gain energy, becoming less dense, causing them to rise. The rising particles carry their heat energy with them, while the cooler particles replace their position, creating a continuous flow of particles and heat energy.

Radiation transfers heat in the form of electromagnetic waves. A common example of this is infrared radiation. Unlike conduction or convection, radiation does not require a material or particles to transfer heat through, meaning it can travel in a vacuum. All objects emit varying amounts and wavelengths of radiation, which are determined by their respective temperatures. The higher the temperature, the more intense the radiation emitted, and the shorter the wavelengths. In solid

insulators, such as those studied in this work, the primary heat transport mechanism is conduction. Thermal radiation is not a significant factor in heat transfer in solid insulators [34].

The ability of a material to transfer heat is defined as its thermal conductivity, and represents a measure of its ability to transfer thermal energy across a temperature gradient. In other words, heat travels more quickly through a material with higher thermal conductivity [34]. Thermal conductivity is defined as the rate of heat flow through a unit cross-sectional area under a temperature gradient perpendicular to the area. The SI units for thermal conductivity are $\mathrm{W}/(\mathrm{m} \cdot \mathrm{K})$.

The thermal conductivity of a material can vary strongly with temperature. For gases at low pressures, thermal conductivity may rise, but for liquids and solids there is the possibility of both lower and higher thermal conductivity with increased temperature, as can be seen in Fig. 2.9 and Fig. 2.10.

In metals, electron scattering plays a significant role in determining thermal conductivity. When temperatures are high, electron-phonon scattering becomes the dominant factor, resulting in a reduction in thermal conductivity. However, at lower temperatures, the influence of electron-phonon scattering may decrease, enabling an increase in thermal conductivity [34].

The temperature dependence of thermal conductivity can strongly vary from material to material. Certain materials may demonstrate atypical trends. This behaviour can be attributed to intricate interactions between electrons and phonons, and present crystal lattice defects. Some materials, such as those with non-cubic crystal structure, may have anisotropic thermal conductivity, that is, different thermal conductivities along different directions.

A related thermal property is thermal diffusivity, which describes how quickly a material adapts to changes in temperature. It quantifies the speed at which heat can disperse or propagate within a material, accounting for its capacity to conduct and retain heat energy. Thermal diffusivity combines thermal conductivity and specific

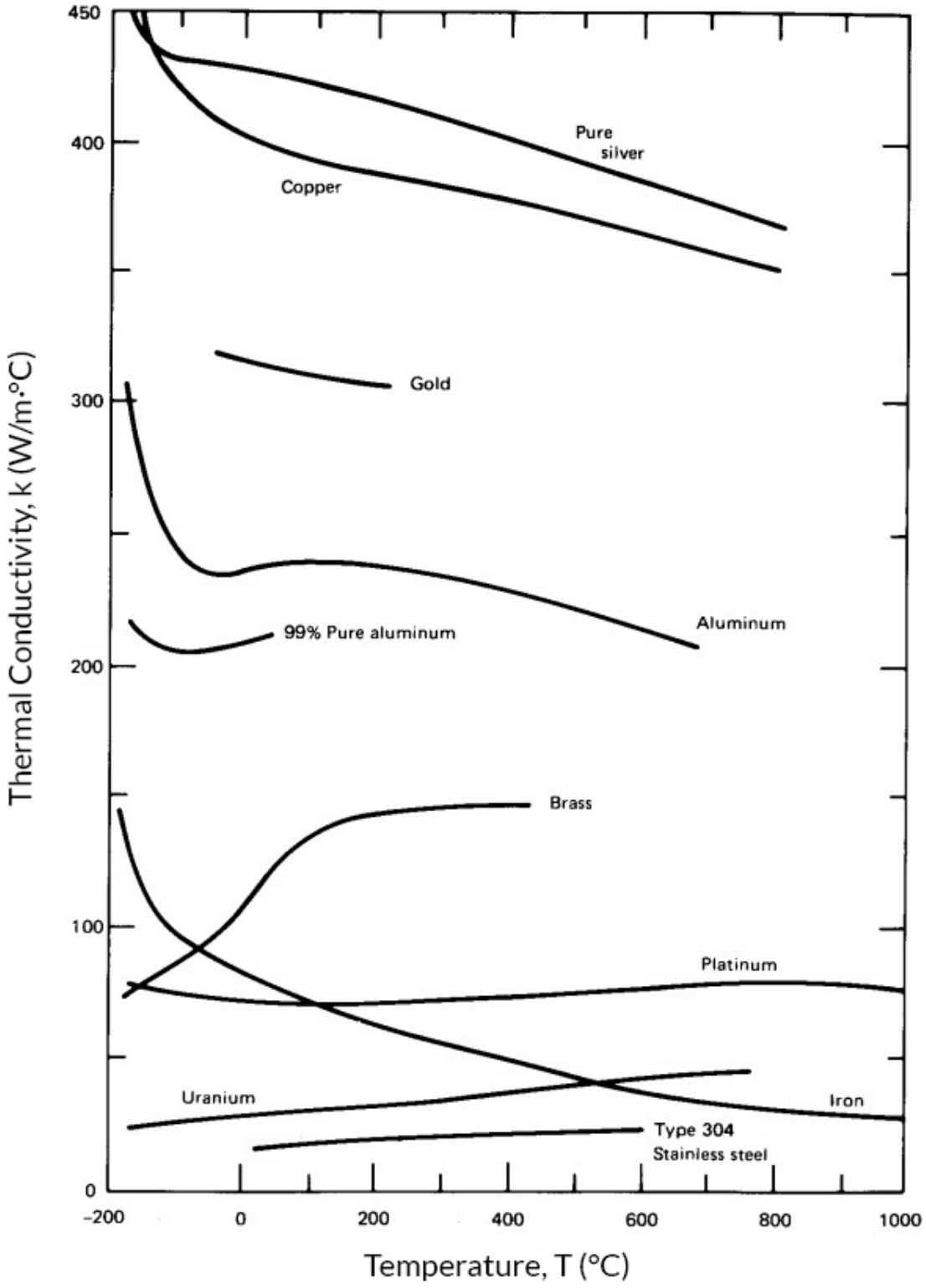

Figure 2.9: Variation of thermal conductivity of metallic solids with temperature. Figure from [34].

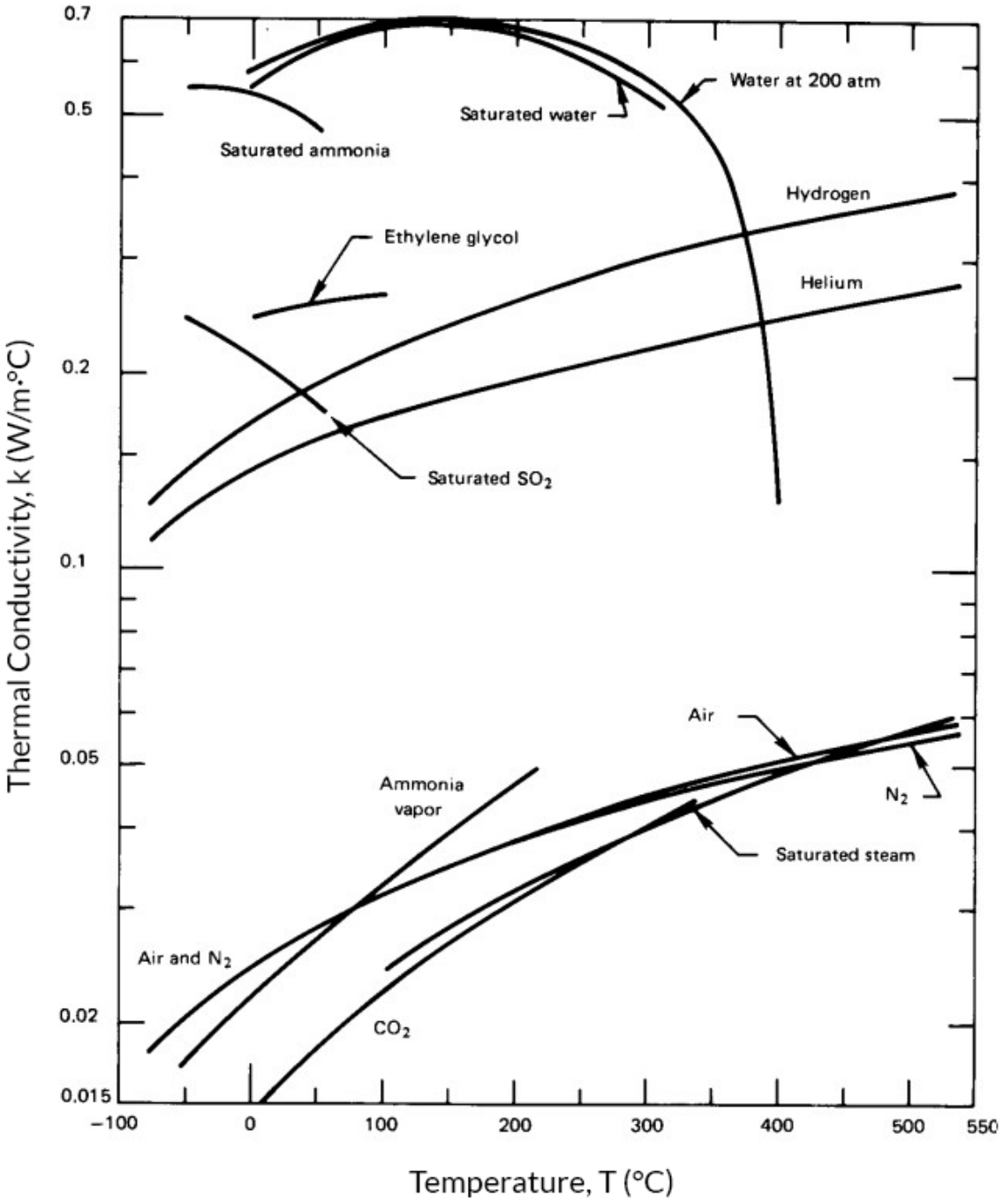

Figure 2.10: The temperature dependence of the thermal conductivity of liquids and gases that are either saturated or at 1 atm pressure. Figure from [34].

heat capacity to produce a comprehensive metric of a material's thermal properties.

The formula for thermal diffusivity, α, is as follows:

$$\alpha = \frac{k}{\rho c}, \tag{2.7}$$

where, k is the thermal conductivity, ρ is the material density, and c is the specific heat capacity [34]. The SI units for thermal diffusivity are m^2/s.

The heat capacity (C) of a material is the amount of energy required to raise the temperature of a given amount of substance by a certain amount. Specific heat capacity or specific heat, denoted by a lowercase c, is an intensive property and includes the mass in the definition; thus it is the energy required to increase the temperature of a unit of mass by one degree (Kelvin or Celsius). SI units for specific heat capacity are $J/(kg \cdot K)$ but $J/(g \cdot K)$ or the equivalent $J/(g \cdot °C)$ are also commonly used. Heat capacity is usually dependant on temperature and the phase of the material. The specific heat capacity of a material can be calculated using the following equation:

$$Q = mc\Delta T, \tag{2.8}$$

where, Q is the heat energy added to (or removed from) the substance of mass m, and ΔT is the change in temperature [34]. Specific heat varies from material to material and is determined via experimental methods. It also varies with the phase of the material and its temperature. Substances with high specific heat can absorb or release a large amount of heat energy without significant change in temperature. This is an important characteristic for temperature regulation and heat storage. Conversely, substances with low specific heat can undergo significant temperature changes when heat energy is added or removed. An example of a material with high specific heat is water, often used in both heating and cooling systems for this very reason.

The overall thermal efficiency of the reactor depends on the rate of heat transfer to the coolant, which is determined by a number of factors, including the thermal conductivity of the breeder material itself. In general, ceramic oxides have low thermal conductivities due to being insulators and so heat transfer is predominantly facilitated by phonons alone. Defects introduced into the ceramic breeder matrix during operation, either from lithium depletion or radiation damage, will act as phonon scattering centres, degrading the thermal conductivity still further. Snead *et al.* explored the relationship between defect density introduced by neutron irradiation and degradation of the thermal conductivity of ceramic materials [35]. They observed a sublinear dose dependence in the range 0.001 and 0.01 dpa at low temperature. Molecular Dynamics (MD) simulations of SiC suggested that the increase in thermal resistivity was proportional to the defect concentrations, however, the factor of this proportionality depended on the specific defect type [36]. At higher temperatures Snead *et al.* demonstrate that the thermal conductivity is closer to the bulk value due to the defect recovery [35]. However, MD simulations of Gd doped UO_2, also showed that impact on the thermal conductivity decreases as a function of temperature [37]. In these simulations the defect population remains roughly constant and so it is clear that recombination is not the sole reason for the recovery in thermal conductivity.

In addition to reducing the heat flow to the coolant the reduction in the thermal conductivity may result in increased thermal stresses in the pebbles that may result in loss of their structural integrity. Therefore, it is essential to be able to determine the thermal conductivity of the material as it is ages.

2.2.2 Phonon transport

The three modes of heat transfer have been briefly discussed: conduction, where heat is transferred by particles through a medium, due to a temperature gradient; convection, where heat is carried from a source by a moving fluid; and radiation, where all bodies at non-zero temperature emit heat by electromagnetic radiation [34].

This work concerns the mechanisms involved in heat flow by conduction in solids. Conduction is less seen in liquids and gases due to the larger distances between particles. The eponymous empirical law of heat conduction, defined by Joseph Fourier in 1822, states that "*the heat flux resulting from thermal conduction is proportional to the magnitude of the temperature gradient and opposite to it in sign*" [38]. We can write this using k to represent the constant of proportionality as:

$$q = -k\frac{dT}{dx}. \tag{2.9}$$

Where, q is the heat flow per unit area, known as the heat flux (with SI units of $\mathrm{W/m^2}$). This constant is known as the thermal conductivity, k [34]. This equation can be developed to describe three-dimensions as:

$$q = -k\nabla T. \tag{2.10}$$

The direction of heat flow is always clear when considering heat conduction in a single dimension, allowing the use of Fourier's law in the simple scalar form:

$$q = -k\frac{\Delta T}{L}. \tag{2.11}$$

Where, L is the thickness in the direction of heat flow, and both q and ΔT are positive.

We can describe a crystalline material using a lattice. A lattice describes the regular and repeating pattern in the arrangement of atoms in a solid [39]. Atoms in a solid have little freedom to move compared to liquids and gases, and thus vibrate at high frequencies about their lattice positions due to their thermal energy. These vibrations are coupled to their neighbours due to atomic bonding and thus form lattice vibrational waves which travel through the material at the speed of sound. The vibrational thermal energy is quantised, and one quanta is referred to as a phonon (analogous to a photon) [40]. Free electrons in the solid also carry heat

through their movement. Therefore, the transfer of heat by conduction is by both the movement of free electrons and phonons.

The phonon contribution to the thermal conductivity of a material is influenced by how these phonons interact with various imperfections in the lattice, such as defects, grain boundaries, and impurities in the material. When phonons encounter these defects, they can scatter in a number of ways, ultimately reducing their ability to transfer heat efficiently as they lose energy or alter their path due to collisions.

The phonon mean free path refers to the distance that a phonon can travel before it encounters a scattering event. When dealing with materials that possess high thermal conductivity, phonons have the ability to travel greater distances before encountering these scattering events, leading to more efficient heat transfer. In contrast, materials with lower thermal conductivity experience more frequent scattering of phonons, thus leading to less efficient heat transfer [41].

The thermal conductivity of a material is influenced by the efficiency with which phonons can transport heat. Materials that have strong atomic bonds and well-organised lattice structure, such as metals, typically exhibit high thermal conductivities. Materials which possess weaker bonds or more intricate lattice arrangements, such as insulators, generally have lower thermal conductivities due to the increase in the frequency of phonon scattering. The different types of phonon scattering are: phonon-phonon scattering, phonon-electron scattering, boundary scattering, and defect scattering [41].

There are two types of phonon-phonon scattering: normal scattering, and Umklapp scattering. Normal scattering does not significantly impede heat flow and thus does not significantly affect the thermal conductivity. The second type of scattering, Umklapp scattering is named for the German for "backfolding". This type of scattering involves non-linear processes in which phonons collide and scatter with one another, leading to a change in their wave vectors. Umklapp scattering is more dominant at higher temperatures and can limit thermal conductivity through causing

resistance to heat flow [41]. At high temperatures, Umklapp scattering processes dominate, while at lower temperatures, normal scattering dominates. This transition is described by T_D, which is a characteristic temperature of a material.

The behaviour of the phonon thermal conductivity dependence on temperature of crystalline materials can broadly be described by the following: At high temperatures (temperatures much greater than T_D) it should vary as T^{-1}, i.e. the phonon thermal conductivity decreases with increasing temperature. At high temperatures there are always enough phonons with enough energy for Umklapp processes so they dominate, and phonon-phonon scattering is significant. At intermediate temperatures above T_D, the thermal conductivity decreases as $e^{T_D/T}$. At intermediate temperatures below T_D, the thermal conductivity increases with decreasing temperature as T^2 to T^3, due to increasing phonon population, reaching a peak in this temperature range until phonon-phonon scattering takes over. At low temperatures (much less than T_D) the thermal conductivity increases as per the Debye law as T^3, due to the temperature dependence of the conductivity only depending on the heat capacity. The Umklapp processes are frozen out and the phonon mean free path becomes very long, leaving boundary scattering at the material surface to dominate [42]. A sketch of this behaviour can be seen in Fig. 2.11a.

The sharp peak observed in Fig. 2.11a from phonon-phonon scattering processes may be dampened by other phonon scattering processes to produce a resulting thermal conductivity more akin to Fig. 2.11b. Boundary scattering occurs in polycrystalline materials contain grain boundaries, which are the interface between two different crystal grains. Phonons can scatter at these boundaries due to the abrupt change in crystal structure disrupting the path. For nanoscale specimens, i.e. materials with a high surface area to volume ratio, the surface is another significant boundary at which phonon scattering takes place. This type of phonon scattering is particularly significant at low temperatures where the phonon mean free path is comparable to the size of the grains, or the size of the specimen.

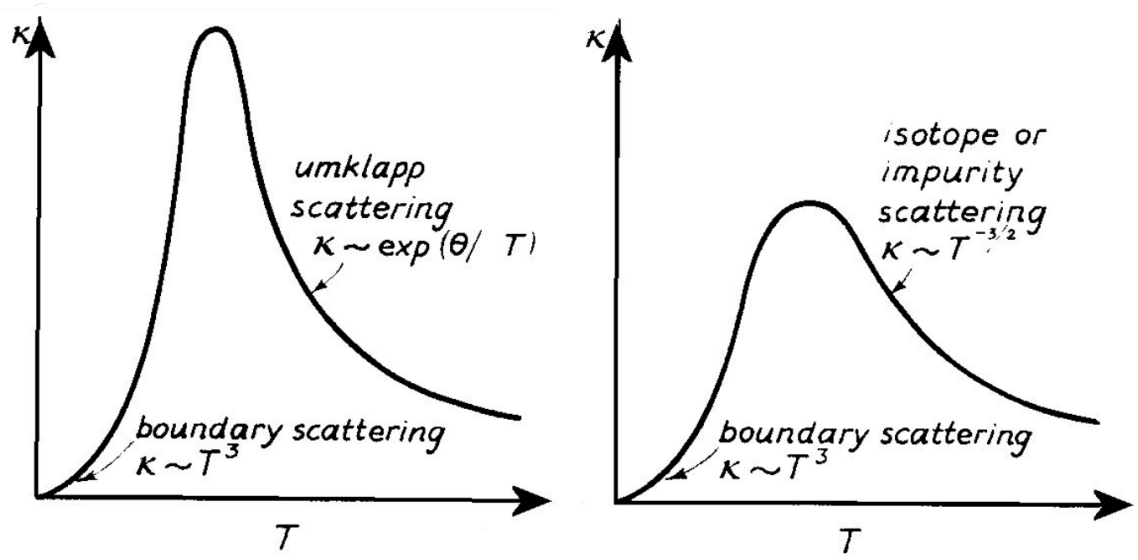

(2.11a) **(2.11b)**

Figure 2.11: Schematic variation in thermal conductivity with temperature for (a) isotopically pure and (b) impure material. [43]. Where, θ represents the Debye temperature.

Further to this there is defect or impurity scattering. The simplest of these are point defects, which refer to imperfections in the lattice structure such as vacancies (a lattice position missing an atom) or interstitials (extra atoms to the lattice). These point defects disrupt the regular lattice vibrations, leading to phonon scattering.

Line defects in the lattice structure are called dislocations. These can serve as relatively large scattering centres compared to smaller point defects, hindering more phonon movement. Impurities are foreign atoms in the crystal lattice. These can prove to be a larger disturbance than native interstitial atoms due to the possibility of a larger disruption to the crystal lattice. Anharmonic effects involve deviations from simple harmonic behaviour in the lattice vibrations. Anharmonic scattering processes, such as phonon-phonon interactions are what is responsible for Umklapp scattering [41].

Phonon-electron scattering describes when phonons scatter off free electrons in the material. This is particularly significant in metals and other materials with high amounts of free electrons [41].

Phonon scattering is a major factor that affects the phonon component a material's thermal conductivity. Strong scattering centres and frequent scattering events reduce the mean free path of phonons, making it more difficult for them to transport heat. As a result, materials with more scattering mechanisms tend to have lower thermal conductivities. These effects become all the more important when studying the thermal conductivity of a insulator such as Li_2TiO_3, due to its already limited thermal conductivity in perfect crystal form [41].

From the kinetic theory of gases, the thermal conductivity can be given as:

$$k = \frac{1}{3} C_v l v, \tag{2.12}$$

where, C_v represents C at constant volume, l is the phonon mean free path and v are the phonon velocities. Phonon velocities can be obtained from the Christoffel equation:

$$\left(\Gamma_{ij} - \rho v^2 \delta_{ij}\right) u_j = 0, \tag{2.13}$$

and,

$$\Gamma_{ij} = \sum_{k=1}^{3} \sum_{k=1}^{3} C_{ijkl} n_k n_l, \tag{2.14}$$

where, ρ is the density, u_j is the displacement in j, n_k and n_j are the direction cosines, C_{ijkl} is the elastic tensor, and δ_{ij} is the Kronecker delta defined as follows: $\delta_{ij} = 1$ if $i = j$, and $\delta_{ij} = 0$ if $i \neq j$. Therefore, there is a clear link between the elastic stiffness of the material and the thermal conductivity [44].

The connection between elastic stiffness and thermal conductivity lies in the fact that both characteristics are affected by the crystal structure and lattice vibrations within a material. The correlation between these properties is not simple, and their interdependence can vary greatly depending on the specific material.

The phonon dispersion relations within a material play a significant role in determining both its elastic stiffness and thermal conductivity. These dispersion relations describe the behaviour of vibrational modes (phonons), as they travel

through the crystal lattice of the material. When a material has strong covalent or metallic bonds, it tends to exhibit higher elastic stiffness, which is often accompanied by higher phonon frequencies and greater thermal conductivity. On the other hand, materials with weaker interatomic bonds may display lower elastic stiffness and consequently lower thermal conductivity [41].

Phonon dispersion relations, also known as phonon dispersion curves, are visual representations that depict the propagation of vibrational modes (phonons), within a crystal material based on their wave vector (or momentum) in the reciprocal lattice. These curves are valuable sources of knowledge regarding the thermal and vibrational characteristics of materials and are instrumental in understanding the dynamics of lattice vibrations.

Phonon dispersion relations are unique to crystalline substances, wherein the atoms or ions are organised in a consistent and repetitive manner. The wave vector is a measure of the momentum carried by a phonon and is connected to the regular pattern of the crystal lattice. These dispersion curves, which depict the behaviour of phonons, are commonly illustrated in reciprocal space, where the different elements of the wave vector are represented along the axes.

Phonon dispersion curves illustrate the connection between the frequency of phonons (represented by angular frequency ω) and their corresponding wave vectors, k. These curves depict various vibrational modes, each characterised by a unique frequency and wave vector. Phonon dispersion curves are composed of several branches, each representing a distinct type of phonon mode. In materials with a crystalline structure, there are three major types of phonon branches: acoustic. optical, and acoustic-optical mixed branches. The acoustic branches signify vibrations with lower frequencies and are linked to the mechanical properties of the material, such as its elasticity and speed of sound. Optical branches correspond to the vibrations with higher frequencies and are often associated with the material's electrical properties, such as its response to electromagnetic radiation. The acoustic-optical mixed branches

encompass a combination of both acoustic and optical modes [41]. The phonon dispersion curves and density of states for Li_2TiO_3 can be seen in Fig. 2.12.

The phonon dispersion curves are affected by the symmetry of the crystal, as well as the size and configuration of the Brillouin zone (BZ), a key concept in the field of solid state physics. The BZ serves as a representation of the permissible range of wave vectors that phonons can possess. The way phonons behave in a dispersion relation is impacted by various interactions and scattering events that occur between them. These interactions encompass phonon-phonon scattering, where phonons collide with each other, as well as phonon-defect scattering, where phonons interact with imperfections or defects in the material. Additionally, anharmonic effects also play a role in modifying the curvature and overall shape of the dispersion curves.

Phonon dispersion relations can vary with temperature. With an increase in temperature, the phonon dispersion may undergo alterations caused by the heightened thermal activity of atoms. This can result in modifications in the frequencies of phonons. They play a vital role in the understanding of a wide range of thermal and mechanical characteristics exhibited by materials, including the thermal conductivity, specific heat capacity, and thermal expansion. In order to investigate and analyse the phonon dispersion curves in specific materials, a combination of experimental techniques such an inelastic neutron scattering and Raman spectroscopy, along with theoretical methods such as Density Functional Theory (DFT) calculations. These dispersion curves offer valuable information about the vibrational patterns and thermal transport properties of crystals.

In most materials heat is conducted via two primary mechanisms, phonon heat conduction (as discussed above) and electron heat conduction. In metals, the thermal conductivity is influenced by the presence of a sea of delocalised or ‘free’ electrons, i.e. electrons that are not bound to individual atoms. These free electrons can move relatively freely through the material and contribute to the electrical conductivity

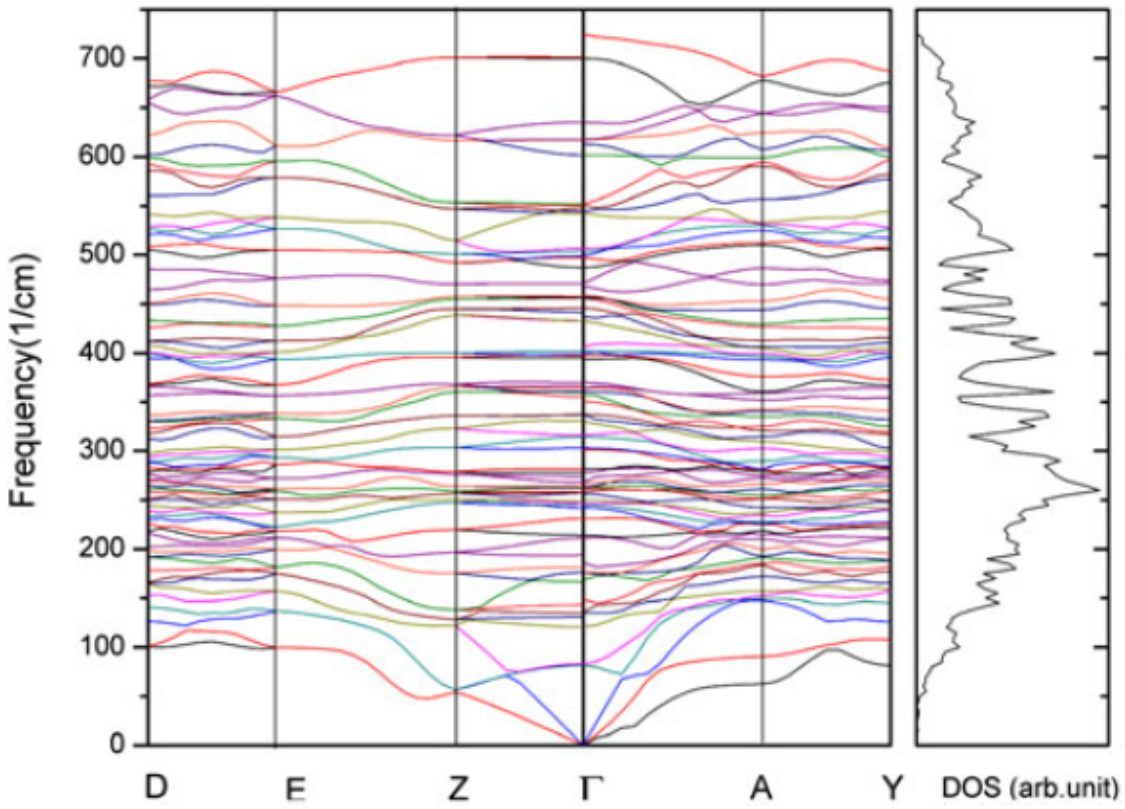

Figure 2.12: Phonon dispersion curves and density of states for $\beta-Li_2TiO_3$ along the main symmetry directions in the BZ [45].

as well as the thermal conductivity, by carrying both electrical current and thermal energy.

When a temperature gradient exists within a conducting metal, free electrons gain kinetic energy as they move from hotter regions to cooler ones. This kinetic energy, i.e. electron motion, contributes to heat conduction. The Wiedemann-Franz law is a fundamental relation in solid-state physics and relates electrical conductivity and thermal conductivity of metals. According to this law, in a metal at uniform temperature, the ratio of the thermal conductivity to the electrical conductivity is proportional to the absolute temperature and the Lorenz number [41].

Such as discussed for phonons, impurities and crystal defects can also scatter electrons, which will hinder the flow of both electrical current and thermal energy. Also, similar to phonons, electrons have a mean free path describing the average distance between scattering events.

In thermoelectric materials, the electron contribution to the thermal conductivity is intentionally manipulated to achieve higher electrical conductivity and low thermal conductivity, to achieve efficient conversion of heat into electricity or vice versa. In insulators, such as Li_2TiO_3, the thermal conductivity is primarily governed by phonon heat conduction, with the electron contribution being negligible. Unlike in metals, there are no free electrons available to carry thermal energy, so the electrons behave very differently. The large band gap (between the valence band and conduction band) and limited mobility of electrons in an insulator means they have little involvement in thermal transport. Electrons in an insulator may display some thermal motion, but they quickly come to thermal equilibrium with the lattice, and thus do not significantly contribute to heat transport [41].

2.2.3 Experimental measurement of thermal conductivity

There are a number of experimental methods that are used to measure the thermal conductivity of a material. A popular group of methods are steady-state methods.

In these methods, the temperature of the material remains constant over time. This may simplify measurement but also requires a precise experimental setup. Heat may be lost through radiation and convection. These methods work by applying a known heat flux Q to a sample with a specific surface area A and thickness x. For example, the heat can be applied by a hot plate on one side of the sample and a cooler plate on the other side. The accuracy of the sample thickness is vital to the calculation. Once the sample has reached steady state/thermal equilibrium, the temperature difference δT across the thickness of the sample is measured. Under the assumption of one-dimensional heat flow and an isotropic medium, Fourier's law (Eq. 2.11) [38] can be used to determine the thermal conductivity.

Another popular method is the laser flash method, which is well suited to measurements of solid materials. It exposes one side of a thin sample to a laser pulse and observes the temperature rise at the other side of the sample. By finding the rate of temperature increase, the thermal diffusivity can be obtained. The thermal conductivity can then be found by rearranging Eq. 2.7.

2.3 Lithium ceramics

Ceramics encompass a diverse range of materials that are created through the process of shaping and subsequent firing or sintering of an inorganic nonmetallic substance to high temperatures. Traditional ceramics include earthenware and porcelain and are made from clay for uses such as pottery. Ceramics possess a unique combination of properties that distinguish them from other materials. They are known for their hardness, high compressive strength, and resistance to very high temperatures. They are however also brittle, and weaker to shearing and tension. Beyond traditional use, advanced ceramic engineering has become a major field in materials engineering. These ceramics are carefully designed to possess the ideal properties required for specific applications. In contrast to traditional ceramics,

which typically rely on natural raw materials such as natural clay, that likely contain numerous impurities, ceramics can be crafted from highly purified raw materials. This careful selection of raw materials is followed by a complex manufacturing process that utilises significantly higher temperatures than in traditional use. The final result is a material with superior mechanical strength, thermal stability, and chemical resistance. Consequently ceramics are used in many industries such as electronics, automotive engineering and medical device manufacturing.

Numerous lithium ceramics have been considered for use in blanket concepts that employ a solid breeder, including Li_2O, $LiAlO_2$, $LiCoO_2$, Li_2ZrO_3, Li_2ZrO_3, Li_4SiO_4, and Li_2TiO_3 [46–49]. Among these, two leading candidates have emerged: lithium orthosilicate (Li_4SiO_4) and lithium metatitanate (Li_2TiO_3) [3, 50], which are being developed for testing in ITER, when it begins full performance operation.

These materials are particularly attractive compared to other candidate ceramic breeder materials, for their high Li density and good chemical stability [50, 51]. Due to its higher lithium density, Li_4SiO_4 offers higher T breeding ratios, however Li_2TiO_3 has better chemical stability, good T release, and low-activation characteristics [52], while also being insensitive to moisture [53]. Therefore, the best choice is not clear, as is evident in the differing approaches adopted by the international parties for development of TBMs [54]. Biphasic ceramic pebbles, consisting of both Li_4SiO_4 and Li_2TiO_3 have been proposed to enhance the mechanical properties of Li_4SiO_4 [55], leading to KArlsruhe Lithium OrthoSilicate (KALOS) as the current EU breeder material of choice for DEMO [56, 57].

The phase diagram of Li_2O-TiO_2 (Fig. 2.13) demonstrates that the Li_2TiO_3 phase has the ability to tolerate significant variations from its stoichiometric composition, ranging from 47 to 51.5 mol% TiO_2. This flexibility is advantageous in the production of Li_2TiO_3, as it allows the addition of excess lithium, which enhances the T breeding ratio. This is essential for advanced ceramic breeder designs [61]. Furthermore, the structure of Li_2TiO_3 can adapt to the loss of lithium caused by transmutation. On

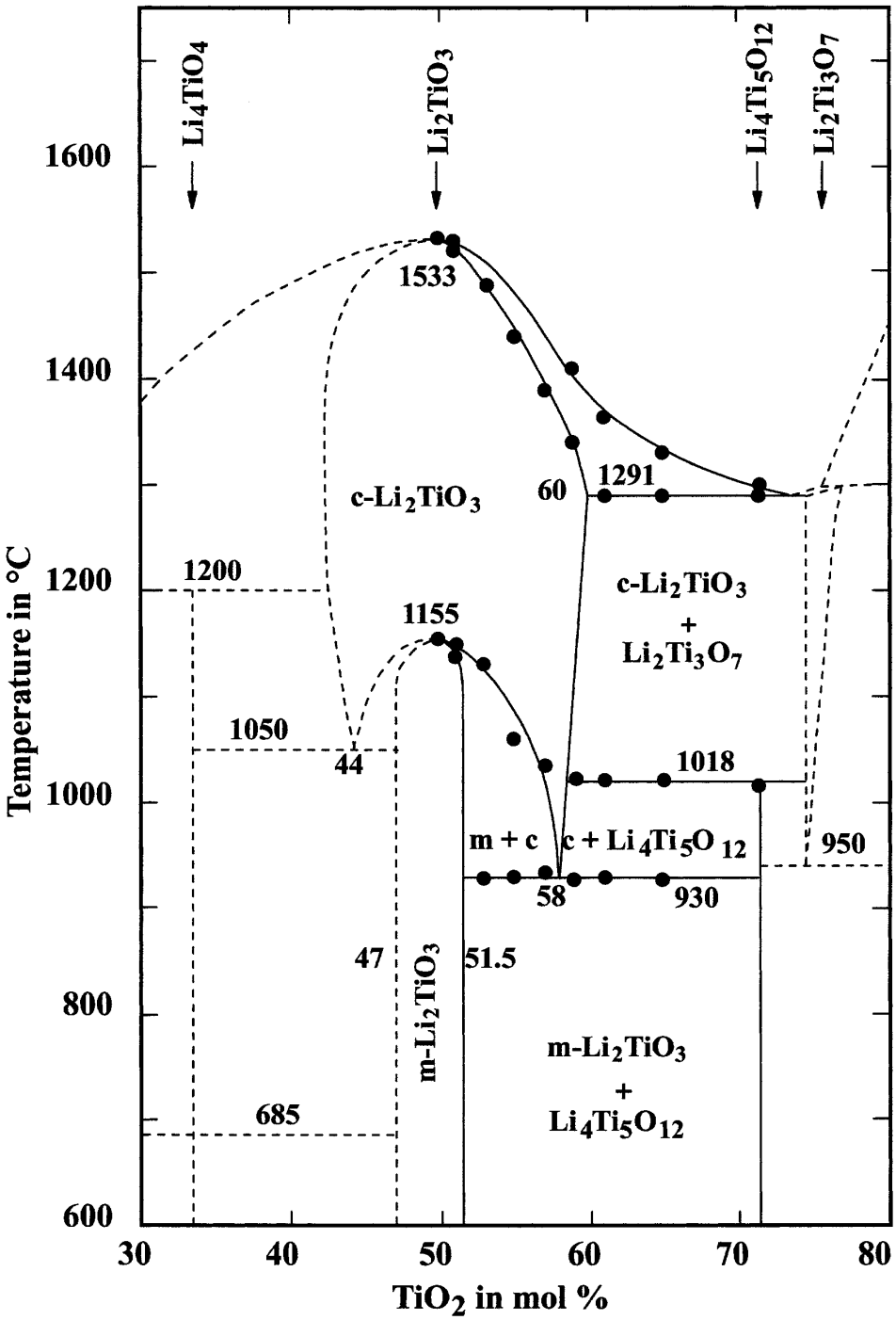

Figure 2.13: Phase diagram of the Li_2O–TiO_2 system; where the dashed lines are from Izquierdo and West [58], and Mikkelsen [59], and the solid lines are from Kleykamp [60]. Figure from [60].

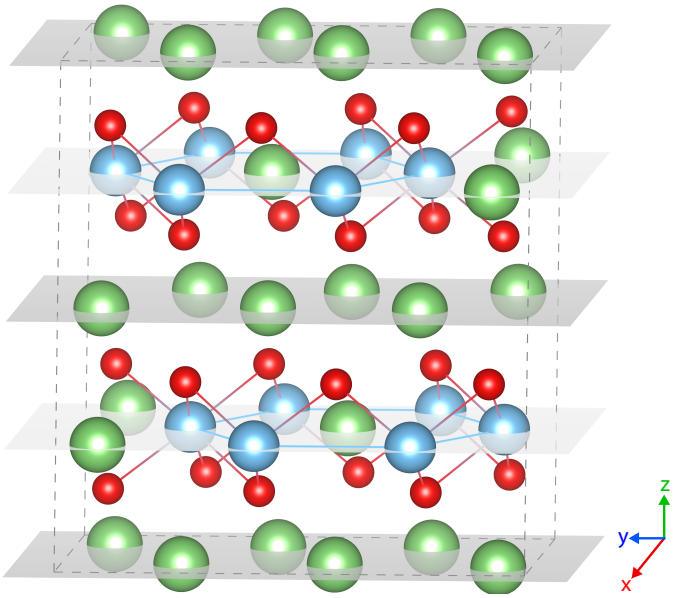

Figure 2.14: Unit cell of Li_2TiO_3, where green, blue and red spheres represent lithium, titanium, and oxygen atoms respectively. (The lattice constants of Li_2TiO_3 are as follows: $a = 5.06\,\text{Å}$, $b = 8.79\,\text{Å}$, $c = 9.75\,\text{Å}$, $\beta = 100.2°$ [63]).

the other hand, Li_4SiO_4 is a compound that cannot tolerate substantial deviations from stoichiometry [62]. Consequently, any excess lithium is incorporated into an Li_2SiO_3 secondary phase in Li_4SiO_4. This phase transformation could have implications regarding operation, for example, change the Li density. In this work, we focus on Li_2TiO_3, and the evolution of its thermal conductivity as a function of its stoichiometric composition and porosity, compared to the perfect crystal.

2.3.1 Lithium meta-titanate, Li_2TiO_3

The phase diagram of Li_2O-TiO_2 shows the three crystal phases of Li_2TiO_3 (Fig. 2.13). At low temperatures it forms the metastable α-phase until a phase transformation at 300 °C to the monoclinic β-phase, which is the stable phase up to a temperature of 1155 °C [60]. This temperature window encapsulates the operational temperature range and is thus the only phase investigated in this work. Above 1215 °C there is a phase transformation to the cubic γ-phase before melting above ∼1500 °C.

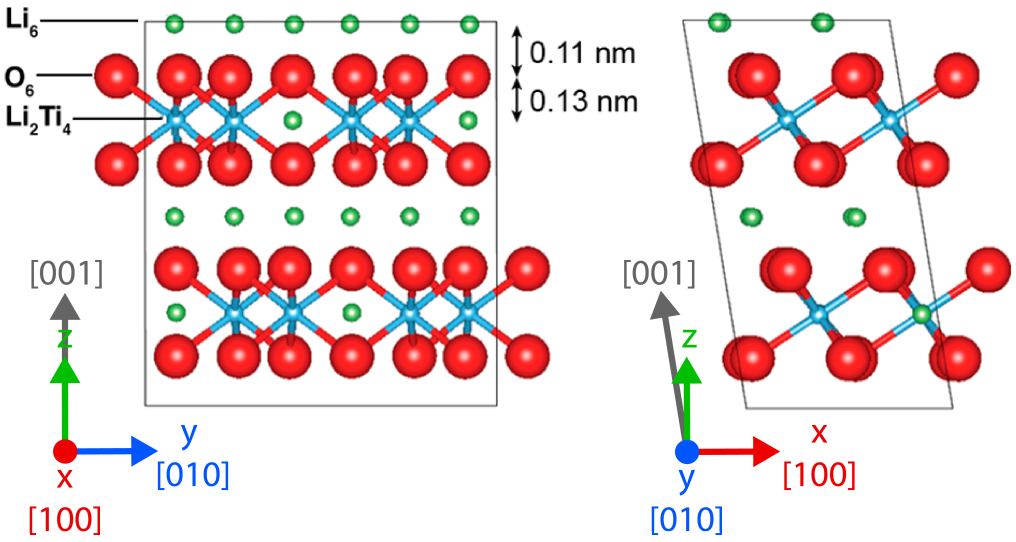

Figure 2.15: The side views of a unit cell of Li_2TiO_3, where green, blue and red spheres represent lithium, titanium, and oxygen atoms respectively. Figure adapted from [65].

The structure of β-Li_2TiO_3 was first found by Lang [64] and subsequently refined by Kataoka *et al.* [63] using single crystal X-ray data. An illustration of the unit cell is presented in Fig. 2.14. From this diagram, the complex layered crystal structure of Li_2TiO_3 is evident, as is the distinct difference in each spatial direction, x, y, and z. Highlighted in more detail in Fig. 2.15 are the three different layers in Li_2TiO_3: the lithium Li_6 layer, the oxygen O_6 layer and the mixed cation layer of Li_2Ti_4 [65]. Within this final layer, six Ti ions forming hexagons centred on Li ions form a honeycomb structure in the xy-plane, which can be stacked on top of each other in a number of different ways giving rise to different space groups (i.e. C2/m, $P3_112$, and C2/c, as seen in Fig. 2.16). Kataoka *et al.* predicted that Li_2TiO_3 can be considered as a disordered rocksalt structure with alternating Li and $LiTi_2$ (111) planes described with a glide plane and the C2/c space group seen in Fig. 2.16d. This complex structure implies that the physical properties measured in the material along each axis will be different.

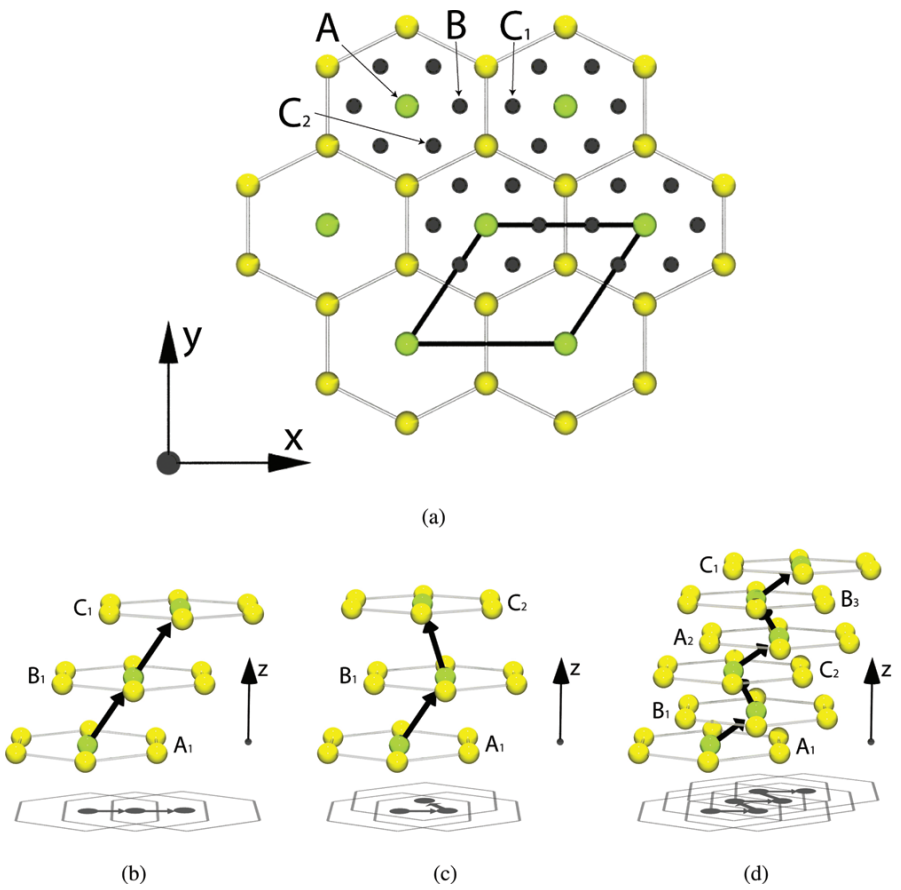

Figure 2.16: Different stacking schemes for the $LiTi_2$ planes. a) Shows the honeycomb structure in the xy-plane. Where green spheres represent lithium ions, yellow spheres represent titanium ions, and black spheres represent the possible stacking locations of the central lithium ions. The different stacking schemes in the z-direction generate the b) C2/m, c) $P3_112$, and d) C2/c space groups. Figure from [66].

2.3.2 Crystalline defects

In a wide range of scientific and engineering fields, imperfections or irregularities are referred to as defects. In the field of materials science this refers to abnormalities in the structure or composition of materials. Defects may refer to macroscopic flaws that are visible to the naked eye, such as cracks and inclusions. However, we focus on defects in the microstructure of the material and how these can affect the behaviour and properties of the material. Crystal defects, also referred to as lattice defects or crystal imperfections, are deviations or irregularities from the perfect and organised arrangement of atoms or ions within a crystalline material. Defects can be introduced during any stage of the useful life of the material, whether during initial fabrication and processing, or during use. It is important to understand the different defects that may occur and how they can affect material performance. In a simple example a crack in a material may weaken the material or lead to the failure of the structure made from the material. In addition to strength, these defects can manifest in many forms and can exert substantial influence on the material's physical, mechanical, electrical, and thermal characteristics. In order to understand the implications of crystal defects, it is necessary to categorise them into distinct groups. There are several different types of microscopic defects which can be categorised according to their dimensionality, i.e. point defects (0D), linear defects (1D), planar defects (2D), and volume defects (3D) [41].

Point defects involve irregularities in the lattice position of a single atom or ion. They include vacancies, interstitials, and substitutions (see Fig. 2.17). Vacancies are point defects that result from missing atoms in the crystal lattice. Interstitials are atoms or ions from external or internal sources that occupy positions in the crystal lattice between designated lattice sites. The additional atoms may be from the material itself or impurities from an external source. A Frenkel defect is formed when an atom leaves its lattice site and becomes an interstitial defect in a nearby

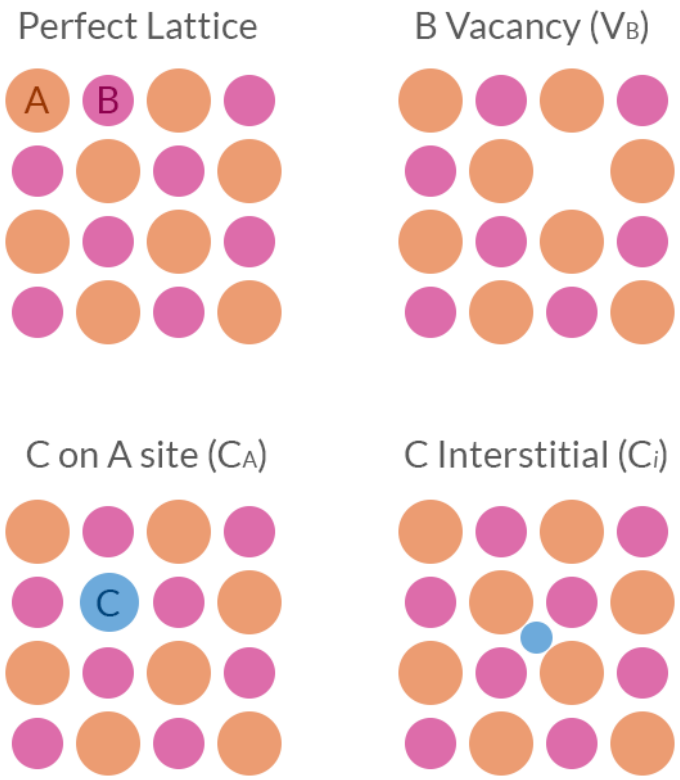

Figure 2.17: Simplified diagram illustrating various types of point defects that can occur in a crystalline material, along with the naming system used in this work to describe them.

site, leaving a vacancy defect in its original site. Stoichiometric defects maintain the ratio of atomic species of the material, whereas non-stoichiometric defects disturb the stoichiometric ratio due to the addition or removal of ions. In the case of substitutional defects, foreign atoms or ions of a different element than that contained in the pure material take the place of atoms or ions in the lattice structure. These foreign particles, called dopants, have the ability to modify the characteristics of the material, including its electrical conductivity [41].

Line defects, which are also known as dislocations, refer to the displacement or misalignment of atoms or ions along lines or planes within the crystal lattice. These dislocations can be categorised into various types, including edge dislocations. Edge dislocations manifest when an additional half-plane of atoms is inserted into the crystal structure in a specific orientation. In particular, these edge dislocations play a crucial role in the induction of plastic deformation in various materials.

Screw dislocations refer to the presence of a spiral or helical arrangement of atoms surrounding a central axis. These dislocations occur as a result of shear deformation in materials [41].

Planar defects, which are found on specific crystallographic planes or boundaries, play an important role in influencing the properties of materials. One common type of planar defect are grain boundaries, which are interfaces that separate different crystal grains within a polycrystalline material. The ideal crystal structure is described by single crystals, where the entire material is arranged in a single orientation. However, most materials have multiple crystal grains with different orientations. Smaller grain size leads to more grain boundaries, and vice versa. As well as the boundary itself, other defects such as point and line defects can gather at the grain boundaries and affect the material properties. These grain boundaries have the ability to impact various material characteristics, such as mechanical properties, electrical conductivity, and diffusion rates [41].

Volume defects refer to imperfections or irregularities found within the three-dimensional space of an object or material, which may affect its overall quality or functionality. These defects can vary in size, shape, and severity and may occur naturally or as a result of manufacturing processes. They can be classified into various categories based on their characteristics and impact on the material's properties. They encompass various types, such as inclusions or precipitates, which refer to foreign particles or regions present within a crystal. The impact of these inclusions or precipitates on material properties can either be positive or negative, depending on factors like their size and distribution. Voids or cavities refer to empty spaces found within the structure of a crystal lattice. These spaces can occur because of imperfections that may arise during the manufacturing or processing of the material, ultimately leading to a decrease in its strength [41].

Crystal defects have a significant impact on the field of materials science and engineering, as they have the ability to affect various properties of materials. Sometimes,

defects are deliberately introduced into materials in order to alter their properties for specific purposes. For instance, semiconductors can be doped with defects to enhance their performance in electronics, while dislocations can be introduced into metals to make them more malleable during manufacturing processes. It is crucial to have a thorough understanding of crystal defects and be able to control them effectively in order to customise materials according to specific performance requirements.

Increased temperature can have a profound impact on defects in a material. The manner in which defects, such as vacancies, dislocations, and interstitials, behave is directly influenced by the temperature at which they are exposed. When the temperature increases, it can result in numerous alterations to the structure and concentration of these defects [41].

When the temperature increases, the atoms gain more energy and are able to move more freely. This increased movement can result in the creation of additional vacancies as atoms temporarily abandon their assigned positions. Consequently, it is possible for the vacancy concentration to rise in response to elevated temperatures. The increased energy also allows dislocations and point vacancies to diffuse, i.e. travel, through the crystal structure. The presence of defects can also facilitate the movement of atoms and other defects through the lattice. Dislocations have the potential to serve as efficient pathways for defects to travel, causing them to relocate to dislocation centres or other sites where defects are present [41].

It is also possible that increased defect movement leads to recrystallisation and defect reduction. For instance, annealing at elevated temperatures can result in the removal of point defects, such as interstitials refilling their vacant lattice site. This has the potential to improve the mechanical and electrical properties of the material.

The annealing process typically consists of three stages. First, the material is heated to a specific point, commonly known as the annealing temperature or critical temperature. This is typically below the material's melting point and differs by material type, allowing controlled changes in the microstructure. Then, the material

is held at this temperature for a specific length of time, to guarantee that the entire material has reached thermal equilibrium and the desired alterations to the microstructure are achieved. Following the holding time, the material is gradually cooled in a carefully regulated process. The speed of cooling has significant impact on the microstructure of the final material. Slower cooling rate facilitates a more thorough recrystallisation process, aiding in the alleviation of any built-up stress within the material by the creation of fresh grains without any strain within the material. This is crucial to improving mechanical attributes such as hardness and strength.

Annealing is a critical process in the field of materials science, essential for the production of various components. This process is most commonly used with metals but is also often applied to glass and ceramics. When the material is annealed, the inherent risk of material failure resulting from cracks or deformation caused by stress is significantly minimised. Increasing the ductility is also possible, enhancing the material's ability to deform without fracturing. Consequently, this leads to improved pliability and facilitates the shaping and forming of the material. This becomes particularly significant in industrial procedures such as forging, rolling, and extrusion, where ductility plays a crucial role in achieving the desired outcomes. Annealing can also enhance the homogeneity of a material by promoting uniformity in its composition and microstructure. It can also be used to soften a material, reducing its hardness and brittleness. When the material is subjected to controlled heating and cooling cycles, the internal structure of the material is rearranged, resulting in improved malleability and flexibility. This allows for easier manipulation and shaping [41].

Sintering, by contrast, involves heating a powdered material to a temperature below its melting point, causing particles to fuse together without fully liquefying. While sintering and annealing both use controlled heating, sintering is used primarily to create dense, solid materials from powders and is distinct from annealing, which

targets defect reduction and recrystallisation.

2.3.3 Defects in Li_2TiO_3

Li_2TiO_3 contains three species of atoms, leading to three possibilities of point defects: interstitial defects (Li_i, Ti_i, and O_i), vacancies (V_{Li}, V_{Ti}, and V_O), and six arrangements of antisites (Li_O, Li_{Ti}, Ti_O, Ti_{Li}, O_{Li}, and O_{Ti}). See Fig. 2.17 for a diagram explaining this symbolism.

There have been numerous investigations into the effect of point defects on properties of Li_2TiO_3. Murphy and Hine [67] used DFT to identify the point defects responsible for the accommodation of non-stoichiometry in Li_2TiO_3. Excess Li_2O, as seen in Li-enriched materials, was found to be accommodated by Li interstitials (Li_i^{1+}) that are charge compensated by Li_{Ti}^{3-} defects or electrons. TiO_2 excess, as seen with Li burn-up, is accommodated by mutually charge-compensating V_{Li}^{1-} and Ti_{Li}^{3+} defects.

Kobayashi *et al.* [68] investigated the dependency of irradiation damage density on T release behaviour for Li_2TiO_3 using electron spin resonance and thermal desorption spectroscopy. They found that with increasing damage density in Li_2TiO_3, the apparent T diffusivity is seen to decrease. This was attributed to the creation of T trapping/detrapping sites in the form of dangling oxygen atoms (O^--centres), which hinder the movement of T. With the introduction of more damage, the number of trapping sites also increased, leading to a significant impact of the overall T release from Li_2TiO_3. The T trapping/detrapping by the dangling oxygen atoms becomes more efficient as the density of damage increases. This is due to the neighbouring irradiation damage and/or lithium burn-up producing Li vacancies which create pathways for the T to the dangling oxygen atoms. In further work by Kobayashi *et al.* [69] they found that the oxygen vacancies and the oxygen atoms with dangling bonds exhibit annihilation behaviour during the annealing process, allowing some recombination and control of the defect density, and hence increase in the T release

rate.

Vijayakumar *et al.* [70] investigated Li diffusion in Li_2TiO_3 using nuclear magnetic resonance (NMR) as well as MD simulations. Their MD calculations found that an isolated Li vacancy prefers to reside in the $LiTi_2$ layer, but in the presence of a Ti defect also in this layer, it will migrate to the Li layer sites, which may displace another $LiTi_2$ layer ion to a tetrahedral site. This site is only occupied by a Li ion when two or more Li vacancies occur in the $LiTi_2$ layer. They also found that no significant Li diffusion occurs between 300–500 K. They found that Li diffusion occurs along the c axis between the pure Li layer and the $LiTi_2$ layer, as well as in the ab plane in the pure L layer when no other vacancies are available. In non-stoichiometric Li_2TiO_3, Li vacancies are expected in both layers, thus Li diffusion should be three-dimensional.

Murphy [71] found through DFT simulations that how T is accommodated in the lattice of Li_2O enriched Li_2TiO_3 is dependant on the oxygen partial pressure. In low partial pressure conditions, the T is expected to exist as a hydride ion, occupying an oxygen vacancy that carries a double positive charge (H_O^{1+}). However, as the partial pressure of oxygen increases, the number of available oxygen lattice sites decreases, causing the T to become positively charged, forming a bond with a neighbouring oxygen ion, forming a hydroxide. Throughout the range of partial pressures, the dominant form of T-containing defect in TiO_2-rich conditions is the H_{Li}^0 defect.

These works comment on the effect of point defects of T and Li diffusion; however, the kind of defects and their relative concentrations that can be expected in damage cascades must also be understood. Suhail *et al.* [72] used MD simulations to conduct displacement cascades in β-Li_2TiO_3 using the primary knockon atom (PKA) method. They found that subcascades were more likely to form in Li_2TiO_3 at low temperatures than expected in most materials. The primary damage is composed of Li Frenkel pairs and O_{Li} and Li_O antisites. Li_i were found near O atoms and O_{Li} near Li. Defects displayed directional dependence at both low and high PKA energies, with

Li_{Ti} and Ti_{Li} showing dependence only at high PKA energies. No significant defect clustering was observed at the energies simulated. However, it should be noted that the formation of anion or cation antisites is unlikely.

2.4 Fabrication methods

2.4.1 Synthesis of powder Li_2TiO_3

There has been much discussion on the best breeder blanket concepts [4], with large attention on solid blanket designs [73]. A large portion of solid blanket designs employ pebble beds. Pebble bed concepts have the advantage of reducing cracking concerns and more easily accommodating complex reactor geometries as opposed to sintered bodies. These designs require that the powder lithium ceramic is shaped into pellets or pebbles. The overall blanket porosity is defined by the entire pebble bed, depending upon the sizes of the pebbles/how they are packed and thus is a function of the porosity of the pebbles themselves [74].

The fabrication process for ceramic breeder materials is critical to the material properties and performance. Different methods have distinct impacts on the material microstructure such as affecting the crystal morphology, stability, grain size, density, and maximum crush load, as well as the inclusion of particular impurities introduced in the process. These microstructure variations lead to changes in the macroscopic material properties which must be accurately understood to predict material behaviour in a range of conditions and thus predict its performance in an active fusion reactor [74].

The particular methods through which a material is synthesised has a strong influence on the resulting microstructure of the final product, which in this case are the ceramic pebbles for use in pebble-bed blanket designs. One influential factor on the microstructure is the sintering parameters. Sintering is the process by which the pebbles are densified using heat to minimise pores between the powder particles

through solid-state diffusion, also increasing the strength of the material. This in turn means the porosity of the pebbles is determined by the sintering parameters. By choosing specific sintering temperature and sintering time it is possible to choose the desired porosity within a ± 2% range as seen in the works referenced in this section. However, the true difficulty is a matter of reproducibility in an industrial setting and cost. With the goal in mind for these pebbles to be used in functioning fusion reactors, fabrication methods must prepare for future demand for large quantities.

The size of the resulting grains can also be manipulated by the factors in the fabrication process. Lower temperature sintering leads to larger grains. Larger grains lead to higher thermal conductivity due to the reduced phonon scattering due to fewer grain boundaries. However, for T diffusion it is advantageous to have smaller grain sizes and more grain boundaries for increased T diffusion pathways (see Fig. 2.7). To obtain smaller grains, finer particle size powder can be used.

For use in HCPB blanket designs, Li_2TiO_3 pebbles are required to be highly spherical with a diameter of ∼1 mm, and a relatively high density. Small spherical pebbles are advantageous in that they are easier to store and transport as they fill available space more efficiently and pour smoothly due to high fluidity. The TBR, pebble strength, and thermal conductivity are all improved at higher density. However, a balance is necessary to avoid losing the better T release behaviour seen at low density. This leads to the desirable density being on the order of 85% of the theoretical density (TD) of Li_2TiO_3 [75]. The TD refers to the maximum possible density of the material, without defects or pores. This is calculated as the molecular weight divided by the volume of the unit cell in the crystal lattice.

Pebble fabrication results are tied to the quality of the powder used. A highly sinterable powder with fine and even particle size is desirable for best results. High purity of powders (∼99%) are used to make pebbles. How the pebbles are formed from these powders effects the density/porosity, grain size and purity. Li_2TiO_3 powder synthesis methods include solid-state routes as well as liquid routes (wet

chemistry), such as sol-gel, hydrothermal, and solution combustion [76]. Small grains, and thus increased grain boundary interface, are preferred for improved T release rate due to T transport along grain boundaries [77].

Solid-state powder fabrication methods are conventionally used to produce T breeder pebbles at the industrial scale due to their relative simplicity and minimal waste production, resulting in lower costs. Powder Li_2TiO_3 is created by grinding together the raw materials in their solid phases and heating the mixture to high temperature until the product is formed, which can then be processed into pebbles. From the literature, the density of pebbles formed from powders produced by this method range from ∼83–98% of the TD [75, 78–82], with the additional factor of pebble fabrication methods. Powders obtained by solid-state methods tend to have particles that are very large and uneven in size due to the high calcination temperatures required to elicit the diffusion of the components. This leads to larger grains being formed during pebble fabrication which is not preferable.

One option of solid-state synthesis involving mixed two oxides [78, 83, 84] is shown in the following chemical equation:

$$Li_2CO_3 + TiO_2 \longrightarrow Li_2TiO_3 + CO_2 \tag{2.15}$$

Carbajal-Ramos *et al.* [85] milled the precursors in Eq. 2.15 under air at room temperature for increasing lengths of time (in the range of 10 min–5 h) using a planetary ball mill made of stainless steel. The milled powder was then annealed at a range of temperatures of 400 °C and 600 °C for 24 h, and 800 °C for 5 h. The produced powder was homogenous, with particle sizes of <70 nm. They compared the production method to solution combustion synthesis and found that solid-state synthesis had a higher yield of >99% vs 90%. Tripathi *et al.* [80] used the same precursors and a urea assisted solid state synthesis method to obtain fine powder at 600–700 °C in just 2 h after 1 h of milling.

Park *et al.* [79] investigate the difference in morphology of the resulting powder

fabricated from Li_2O and rutile-TiO_2 or anatase-TiO_2. The difference in TiO_2 structure in the starting materials resulted in 500 nm and 150 nm particle size powder respectively, showing anatase-TiO_2 as suitable for synthesising highly crystalline fine particles. Al impurity from the starting materials was found in the synthesized powder ∼30 ppm, considered acceptable for hands-on operation. Guo *et al.* [81] used Eq. 2.16 with deionised water as the solvent for mixing/milling. The dried mixed powder was then calcined for 4 h at 500 °C to obtain Li_2TiO_3 powder with a particle size of 19 nm, smaller than typically achieved by solid-state methods.

$$H_2TiO_3 + 2\,LiOH \cdot H_2O \longrightarrow Li_2TiO_3 + 3\,H_2O \tag{2.16}$$

Another popular method is sol-gel. A liquid suspension of solid particles, called a 'sol', is prepared by the hydrolysis of inorganic salts of metal alkoxides. It is then heated over time to concentrate it to a gel. Then the gel is strongly heated to evaporate all moisture content leaving the solid product. This procedure yields a wider range of densities for Li_2TiO_3 pebbles [86–91]. Sol-gel has further applications for the creation of the pebbles themselves and in fact a combined process to form pebbles directly from the precursor ingredients. This is discussed further on. Wu *et al.* [86] used a water-based sol-gel method, using $Ti(C_4H_9O)_4$ and $LiNO_3$, and citric acid as the chelating agent and ammonia for pH adjusting to obtain powder with particle size of 40–50 nm.

In hydrothermal synthesis, aqueous mixtures of precursors are heated in an autoclave under increased pressure. The precursors dissolve in the solution leading to supersaturation and then crystallisation. This method produces ceramics of high purity at relatively low temperature, and requires no post-production annealing, avoiding excessive grain growth Zhang *et al.* [92] prepared Li_2TiO_3 powder by adding powder anatase TiO_2 to LiOH dissolved in deionised water, stirring, and heat treatment in an autoclave to induce the hydrothermal reaction. The precipitate was separated using centrifugation and then washed and dried to obtain the powder

Li_2TiO_3 with mean particle size of 3.4 µm. They produced 1.0–1.2 mm pebbles with good sphericity from this powder using dry-rolling granulation, achieving a density of 81% TD with a grain size of 0.82 µm and crush strength of 35 N. Liu *et al.* [93] compared TiO_2 and TBT as titanium sources, producing well crystalline powder of α-Li_2TiO_3 for both, which is a metastable phase that transforms to β-Li_2TiO_3 upon sintering. They found that the TBT synthesised powder resulted in a smaller grain size of ∼20 nm compared to the TiO_2 obtained powder. Each powder was formed into pebbles by dry-rolling. The TBT pebbles reached 84% TD after sintering at 800 °C for 3 h whereas the TiO_2 pebbles required greater sintering of 850 °C to reach only 81% TD. Both pebbles showed good sphericity and small grain size of <1 µm, and good crush strength of ∼35 N.

Solution combustion involves an exothermic chemical reaction between metal nitrates and an aqueous solution of organic fuel heated at relatively low temperature. The fuel decomposes causing a thermal explosion, usually requiring no external heat to sustain combustion. The high temperature and pressure in the reaction forms the solid product. This method produces high surface area powders, which are fine and homogenous, with relative speed and ease. The particle size of the starting materials directly relates to the particle size of the solid product [85]. There is however, the possibility of leftover organic impurities from incomplete combustion, which requires increased sintering.

Carbajal-Ramos *et al.* [85] prepared a stoichiometric aqueous solution of lithium and titanium precursors of Li_2CO_3 and TiO_2, using citric acid, tartaric acid, and HNO_3 as the chelating fuel and oxidizers. The solution was mixed and heated at 70 °C, increasing the reactivity until it self ignites to produce a solid product which is then milled and heated at 550 °C for 12 h to produce the Li_2TiO_3 powder. A range of sintering temperatures were tested, finding that sintering at a low temperature of 800 °C avoided excessive grain growth, producing a grain size of 18–36 nm and >90% TD. The particle sizes produced were between 0.1–0.5 µm, and the presence

of interconnected pores is observed, beneficial for T diffusion. This method has the capability to control the microstructure of the produced powder by modifying the fuel type, fuel/oxidizer ratio and combustion mode. Zhou *et al.* [94] investigated the effect of fuel/oxidizer ratio (0.5-1.5) on the combustion mode and resulting powder microstructure. $Ti(OC_4H_9)_4$, $LiNO_3$, and HNO_3 were used as the raw materials along with citric acid, $C_6H_8O_7$, as the chelating fuel. The synthesised powder was compressed under pressure into 14×2 mm pellets so that sinterability could be tested and found that the pellets reached 90.7% TD at 800 °C (relatively low temperature) with a grain size of 800 nm. Jung *et al.* [95] prepared aqueous solutions of $LiNO_3$ with $TiO(NO_3)$ and used a mixture of urea and citric acid or glycine as the fuel. This was heated until the water evaporated and the mixture underwent spontaneous combustion, producing pure 30 nm Li_2TiO_3 powder without the need for further calcination. Sinha, Nair, and Sinha [96] used $LiNO_3$ and $TiO_2{\cdot}H_2O$ as the starting materials with glycine fuel to obtain powder with the final particle size ∼1 µm after wet-ball milling. The powder was compressed to form 10 mm pellets to test sinterability and a density of 90% TD was achieved at <1150 °C, with a grain size of 1.6–5.82 µm. Shrivastava *et al.* [97] used $TiO(NO_3)_2$ and Li_2CO_3 with citric acid fuel as the raw materials, and studied the effect of pH, citrate/metal ratio, and process temperature on the powder. They found that the powder prepared at lower pH created pebbles with a smaller grain size which is advantageous of T diffusion.

2.4.2 Pebble fabrication

There are many modes of fabrication through which to produce Li_2TiO_3 pebbles. Granulation produces a uniform densified product, improves the compression strength, reduces dust, and is a convenient medium for practical use due to the increased density from compaction and improved flow rate of spheres vs other shapes. Granules can be sieved to obtain consistent sizing which is important for breeder blankets. There are wet and dry granulation methods. Dry granulation methods include direction

compression, slugging, and roller compaction. Dry methods involves weighing, dry mixing, pebble shaping, and sintering. It is less common as it is only suitable for materials that are easily compressed without moisture/adhesive. Wet granulation is most common on the industrial scale as a wet media is used to adhere the particles together. It is suitable for materials which are not sensitive to heat or moisture. Wet methods include spray drying, and extrusion-spheronization. Wet granulation follows these steps: weighing (the active ingredients, binders, adhesives), dry mixing, milling (pestle and mortar to reduce particle size), wet massing (using moisture or adhesives), pebble shaping, drying, and sintering.

Dry methods are generally not suitable for this purpose as they result in lower density, less uniform pebbles. Wet methods allow for greater densification, which is important for T breeding, and smaller grains, which is important for T diffusion. The specific microstructure requirements of the pebbles as breeder material and plasma facing material and industrial production considerations leads to some of the most successful methods for fabricating Li_2TiO_3 pebbles being wet or hybrid methods. These include extrusion-spheronization, freeze-granulation, sol-gel, and slurry-droplet methods. These methods are able to achieve the desired morphology and microstructure with feasible production rate and yield.

Extrusion-spheronisation begins with the dry mixing of the ingredients to obtain homogenous powder dispersion. This is followed by wet massing, i.e. making a sufficiently plastic wet mass using a granulation fluid. The result must be plastic enough to form into shapes while not sticking together during spheronisation. The next step is extrusion, where the wet mass goes through an extruder to form cylinders of uniform diameter which break off into similar lengths from their own weight. Then follows the spheronisation, these cylindrical particles are rounded off into spheres by frictional forces exerted through rapid rotation in a spheroniser. The spherical pebbles are then dried to achieve the desired final moisture content, and screened by to ensure a low size distribution of pebbles before sintering. This method is

popular due to the high sphericity and uniformity of the pebbles and the smooth surface achieved (which is necessary for blanket designs that require coated pebbles). There is however, the potential to pick up metallic impurities from the extruder and spheroniser in addition to the milling of the initial powder. Li_2TiO_3 pebbles were produced using this method [78, 82, 98].

The composition of the wet mass can affect the pebble properties so the media used is a variable to determine. Mandal, Shenoi, and Ghosh [78] used an aqueous solution of poly-vinyl alcohol (PVA) and solid-state method obtained Li_2TiO_3 powder to form the wet mass for extrusion/spheronization and followed with sintering which increased the density with increased sintering time for one method with additional sample preparation steps before pebble fabrication whereas density was decreased with sintering time for the same method missing these extra preparation steps.

Mandal, Ghuge, and Jadeja [84] developed a semi-automatic system for bulk production of Li_2TiO_3 pebbles using the solid-state reaction in Eq. 2.15 for powder synthesis and extrusion-spheronisation pebble fabrication to produce pebbles of average diameter 1.15 mm, sphericity 0.95, porosity 25.08% with grain size of 1–2 µm and a crush load of 25 N. Pebbles fabricated using using an extrusion–spheronisation–sintering processes by Lulewicz and Roux [98] resulted in pebbles ranging from 0.8–1.2 mm with a density of 90% TD, and an open porosity of 5%. Yu *et al.* [99] showed that pebbles with a TD of 92.4% could be achieved through the addition of additives, such as polyvinyl alcohol, glycerol, and agar. Mandal, Shenoi, and Ghosh [78] used polyvinyl alcohol and obtained pebbles of 1.7-2 mm diameter, with a density of 85-90% TD, and 7% open porosity .

Sol-gel has further applications for the creation of the pebbles themselves by forming gel-spheres. There exists a combined process to form pebbles directly from the constituent materials, developed by Deptuła *et al.* [90] to produce pebbles 10 times smaller (<100 µm) than that achieved by extrusion-spheronisation (∼1 mm). [100]Hoshino *et al.* fabricated Li_2TiO_3 pebbles of diameter 1.18 mm with a density

of 89% TD. This method was also applied by Vittal Rao *et al.* [89] to fabricate 0.6–0.7 mm pebbles with a density of 90% TD, of which the open porosity was 3.88% .

A slurry of Li_2TiO_3 powder and water is dropped through a needle or nozzle of chosen size into liquid nitrogen, instantly freezing to produce granules of Li_2TiO_3. These are then freeze-dried by a sublimation process to produce uniform pebbles with homogenous microstructure which are then sintered [83, 101]. This method has a reduced chance of introducing impurities compared to extrusion-spheronisation due to the only risk step being the milling of the powder and not the steps in the formation of the pebbles. Due to the sublimation process, pebbles made by this method have higher (open) porosity. It is therefore necessary to further densify the pebbles by increased sintering. By using a 0.3 mm diameter needle, Lee, Park, and Yu [101] obtained a pebble diameter of 2.5–3.0 mm after freeze-drying which was then reduced to 1.2–1.5 mm after sintering. Sphericity was improved by increased solid content and the addition of glycerin in the slurry. Shrivastava *et al.* [83] obtained pebbles of 1.5–2.0 mm by using a 0.6 mm diameter nozzle which reduced to 1 mm after sintering. Both report good sphericity for the pebbles and that the needle/nozzle size used determined the droplet size and therefore the final pebble size. Guo *et al.* [81] obtained pebbles with density of 83% TD with a grain size of 420 nm and a crush strength of 45 N by sintering at a lower temperature of 800 °C, starting from powder with a particle size of 19 nm.

The vast range of microstructures produced with varying methods and parameters means that a detailed understanding of the material microstructure is difficult to deduce from the experimental literature alone. We turn to simulation to pinpoint the effect of individual microstructure changes on the macroscopic properties by simulating changing only one parameter at a time, which is not easily achieved in experiment. Microstructure changes of interest include the stoichiometry, porosity, grain size, and presence of impurities.

3

Methodology

3.1 Atomistic simulation

Atomistic simulation has become an essential component of materials science research and is likewise well utilised in a range of scientific fields, such as chemistry, physics, geology, and biophysics. Atomistic models are computational models that simulate the behaviour of molecular systems by explicitly considering one of its smallest components, i.e. each atom in a larger molecular system or crystal. In atomistic simulations, the goal is to simulate the motion of every atom over time. By creating connections to the atomic scale behaviour, analysing the combined behaviour of the atoms allows us to understand macroscopic phenomena seen in the material such as phase transitions and deformations. With the ever increasing power of modern day computers, the feasible complexity and scale of these models improves. Atomistic simulation can be grouped into two main categories; quantum mechanical simulations and classical simulations.

Quantum mechanical simulations attempt to solve the Schrödinger equation, which provides the evolution of the wave-function of an isolated system over time. These methods are often also referred to as *ab initio* methods, meaning only physical constants are input for these methods. These techniques are used to describe the elec-

tronic structure of materials. The simplest quantum mechanical atomistic simulation technique is the Hartree-Fock (HF) method. It approximates the wave-function of the system using a mean-field approximation, i.e., assuming that the interactions between electrons in a system with many electrons can be approximated by the average field. This method is often used as the foundation for more sophisticated techniques known as post-Hartree-Fock methods which apply corrections to the HF method. This includes Møller-Plesset Perturbation Theory methods which uses second-order (MP2), third-order (MP3) and higher corrections to account for electron correlation in the mean-field approximation, and the Configuration Interaction (CI) methods which expands the wave function as a linear combination of multiple electron configurations. In contrast to other quantum mechanical techniques which are wave-function methods, Density Functional Theory (DFT) describes the electronic structure of the system by using the electron density instead of estimating the wave-function. DFT uses exchange-correlation functionals and an ionic potential to define the system. DFT is more computationally efficient than the other mentioned quantum mechanical methods, making it suitable for a wider range of applications and more complex systems. This makes it a popular choice for studying the electronic structure of materials.

Molecular Dynamics (MD) has a long history, with the first simulations performed in the 1950s with early access to computers [102]. MD is one of the most widely used modelling and simulation techniques in materials science research and is simple in concept: Apply Newton's equations of motion to all the interacting particles in the system. By tracking their positions and velocities over time, we can study the time-dependent behaviour of a system and gain valuable insights into its properties and dynamics. Consequently, MD is used across most scientific disciplines. They have proven to be valuable tools for investigating a wide range of phenomena, from the behaviour of simple liquids to the folding of proteins and the dynamics of complex biomolecular systems.

Within the field of materials science, MD is routinely used to study the properties of materials and their structural changes under different conditions. Through the accurate modelling of the interactions between atoms and the forces acting on them, we are able to explore the behaviour of matter at the microscopic level. By simulating the motion of atoms and the resulting changes in the material's properties, MD simulations aid in the design and development of new materials with enhanced properties and functionalities. MD simulations offer a comprehensive and intricate analysis of a system's behaviour at the atomic level, unveiling the intricate processes and interactions between individual atoms. By simulating the dynamic nature of molecular interactions, these simulations capture the time-dependent behaviour of the simulated system. MD simulations also have the unique ability to predict properties and behaviours exhibited by the system, providing valuable insights into characteristics that are not well understood, especially by experimental means.

However, it is important to acknowledge the limitations of MD simulations. Simulating large systems or extending simulations over long time scales can be a demanding task for computers and often requires the use of high-performance computing resources due to the computational intensity involved. It is also important to note that MD simulations are primarily rooted in classical mechanics, which means that they may not fully encompass or accurately represent quantum mechanical effects that may be present in the system being studied.

The effectiveness and precision of MD simulations heavily rely on the quality and reliability of the force fields that are employed to depict the interactions between atoms. A particularly influential early MD study was done in 1964 by Rahman [103] on liquid argon. This was one of the first simulations which used a realistic continuous potential and remains a relevant example for modern MD simulations. Considerable improvements have since been made to make MD simulations more efficient, and many new methods have been developed to allow for the study of more complex systems.

The interest of this thesis lies in the evolution of thermal transport in the material. Therefore, we employ MD as it is highly suited to the study of the different dynamic effects that can contribute to the thermal conductivity. The following sections will outline the steps of MD along with the specific techniques used in this work.

3.2 Molecular dynamics

MD is a classical simulation method which treats all atoms in a supercell as point particles interacting through an interatomic potential. The aim of this method is to allow the system to adopt a range of configurations as governed by Newton's laws of motion. The interatomic potential is used to calculate the force from known mass, and from this time averages of quantities of interest can be evaluated. The dynamics are over extremely long simulations, i.e., long enough to resemble the time scales of the processes under study, and therefore resemble real averages. This concept is explained by the ergodic hypothesis.

The ergodic hypothesis is a fundamental concept in both statistical mechanics and the theory of dynamical systems. Its purpose lies in establishing a connection between the time-averaged behaviour of a system and its ensemble-averaged behaviour, particularly in systems that possess numerous degrees of freedom. An ergodic system refers to a dynamic system where the path followed by an individual particle or a collection of particles encompasses the entirety of the available phase space, thus providing a comprehensive representation of all potential states within the system. Essentially, this implies that the system effectively explores and experiences all conceivable configurations or conditions throughout its evolution. The process of calculating the time-average of a physical quantity involves taking multiple measurements of that quantity over an extended duration and subsequently finding the average of these values. This provides insight into how the system progresses and changes over a prolonged period. The ensemble average is determined by taking

the average of a particular physical quantity across a group of similar systems, each in a distinct state. This calculation provides insight into the statistical behavior of the system, reflecting the probability distribution of its various states. In an ergodic system, over a sufficiently long time, the time-average of a physical quantity (such as energy, position, or velocity) is equal to the ensemble average. Therefore, this principle is key to the effectiveness of MD.

In this work, the molecular dynamics calculations are performed using an MD code known as Large-scale Atomic/Molecular Massively Parallel Simulator (LAMMPS) [104]. The simulations are performed on a "supercell" made up of unit cells of the material of interest. Using periodic boundary conditions, the supercell approximates an infinite system; see Fig. 3.1. The configuration files describing the atom positions in the supercells of Li_2TiO_3 for use in the simulation were created using the program Atomsk [105].

3.2.1 Equations of motion

MD studies the classical motion of many-body particle systems and then extracts experimental observables from these dynamics. Since MD calculations can provide insight into the intricate motion of individual atoms in a system, the microscopic mechanisms of energy and mass transfer can be inferred [106].

Considering a N-particle system subject to only the inter-particle forces between them, the Hamiltonian is given by:

$$H(\mathbf{p},\mathbf{r}) = H\left(\mathbf{p}_1,\dots\mathbf{p}_N,\mathbf{r}_1,\dots\mathbf{r}_N\right) = \sum_{i=1}^{N}\frac{\mathbf{p}_i^2}{2m_i} + U\left(\mathbf{r}_1,\dots\mathbf{r}_N\right), \tag{3.1}$$

where, the spatial positions of the particles as a function of time are denoted by $\mathbf{r}_1,\dots\mathbf{r}_N$, their velocities by $\mathbf{v}_1,\dots\mathbf{v}_N$, and their momenta by $\mathbf{p}_1,\dots\mathbf{p}_N$, defined by $\mathbf{p}_i = m_i\mathbf{v}_i$, and $U\left(\mathbf{r}_1,\dots\mathbf{r}_N\right)$ is the potential energy due to the interactions between particles. The forces on the ith atom is then given by:

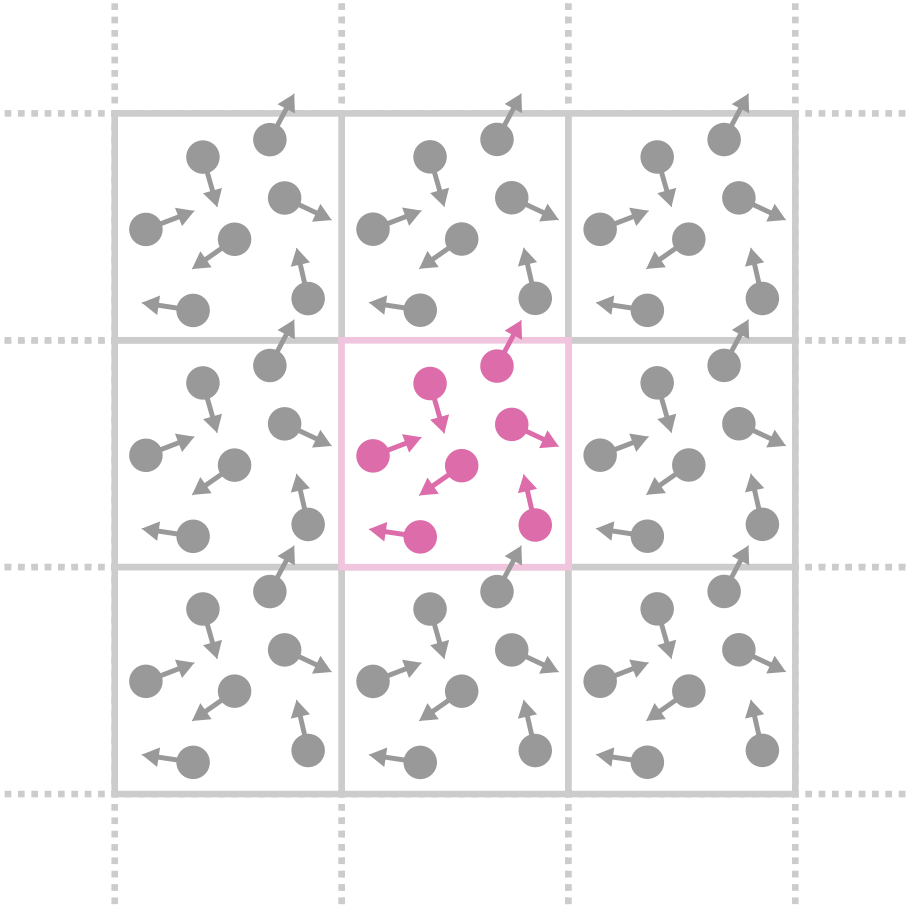

Figure 3.1: Diagram illustrating the concept of periodic boundary conditions in two dimensions, where the pink central cell represents the simulation supercell and the grey cells represent the periodic images. As a particle leaves the simulation supercell, it reenters the supercell from its image.

$$\mathbf{F}_i = -\frac{\partial U}{\partial \mathbf{r}_i}. \tag{3.2}$$

We can then derive the equations of motion (3.5) from the Hamiltonian (3.1) using Hamilton's equations:

$$\dot{\mathbf{r}}_i = -\frac{\partial H}{\partial \mathbf{p}_i}, \tag{3.3}$$

and

$$\dot{\mathbf{p}}_i = -\frac{\partial H}{\partial \mathbf{r}_i} = -\frac{\partial U}{\partial \mathbf{r}_i} = \mathbf{F}_i\left(\mathbf{r}_1, \ldots \mathbf{r}_N\right). \tag{3.4}$$

By substituting the time derivative of Eq. 3.3 into Eq. 3.4, we arrive at Newton's second law, Eq. (3.5):

$$m_i \ddot{\mathbf{r}}_i = \mathbf{F}_i \tag{3.5}$$

where, $m_1, \ldots m_N$ are the masses of the N particles. This tells us that only a complete set of particle positions and momenta is required to determine the entire classical state of the system [107].

The force on each particle is a function of all the position variables, $\mathbf{F}_i = \mathbf{F}_i(\mathbf{r}_i, \ldots \mathbf{r}_N)$, therefore Eq. 3.5 composes a set of $3N$ coupled second-order differential equations for three dimensions, d. By selecting a set of initial conditions at $t = 0$, a unique solution to Eq. 3.5 is obtained, which describes the complete set of positions and velocities of the system at time t. Barring specific special cases, an analytical solution of Eq. 3.5 is not possible. Instead, MD calculations involve an iterative numerical procedure called a numerical integrator to arrive at an approximate solution, whose precision is determined by the chosen time step δt. The numerical solution is statistically equivalent to the true solution for any extracted average physical observables [106].

3.2.2 Integration algorithms

With the assumption that the classical trajectories are continuous, the positions of the particles at a given time, $t + \delta t$, can be determined by a Taylor expansion of $\mathbf{r}_i(t + \delta t)$ about $\mathbf{r}_i(t)$:

$$\mathbf{r}_i(t + \delta t) = \mathbf{r}_i(t) + \dot{\mathbf{r}}_2(t)\delta t + \frac{1}{2}\ddot{\mathbf{r}}_2(t)\delta t^2 + \frac{1}{6}\dddot{\mathbf{r}}_l(t)\delta t^3 + O(\delta t^4). \tag{3.6}$$

Using the knowledge that the equations of motion should be time reversible, we can also write:

$$\mathbf{r}_i(t - \delta t) = \mathbf{r}_i(t) - \dot{\mathbf{r}}_2(t)\delta t + \frac{1}{2}\ddot{\mathbf{r}}_2(t)\delta t^2 - \frac{1}{6}\dddot{\mathbf{r}}_l(t)\delta t^3 + O(\delta t^4). \tag{3.7}$$

This allows the cancelling of the first and third order terms by adding Eq. 3.6 and Eq. 3.7, hence obtaining:

$$\mathbf{r}_i(t + \delta t) = 2\mathbf{r}_i(t) - \mathbf{r}_i(t - \delta t) + \ddot{\mathbf{r}}_i(t)\delta t^2, \tag{3.8}$$

where, the $O(\delta t^4)$ terms have been discarded. We can then rewrite the derivatives in Eq. 3.8 using the convention $\mathbf{a}_i(t) = \ddot{\mathbf{r}}_i(t)$ to obtain:

$$\mathbf{r}_i(t + \delta t) = 2\mathbf{r}_i(t) - \mathbf{r}_i(t - \delta t) + \mathbf{a}_i(t)\delta t^2. \tag{3.9}$$

This gives the positions of atoms accurate to the order of δt^4. This is known as the Verlet algorithm [108]. Though the velocity is not calculated in Eq. 3.8, it can be calculated by using a central finite difference estimate:

$$\mathbf{v}_i(t) = \frac{\mathbf{r}_i(t + \delta t) - \mathbf{r}_i(t - \delta t)}{2\delta t}, \tag{3.10}$$

where, $\mathbf{v}_i(t) = \dot{\mathbf{r}}_i(t)$. Calculating the velocity is required for calculating the kinetic energy. It should be noted that the errors in the velocity are larger than in the

positions, being in the order of δt^2. This algorithm, though effective for evolving the trajectories, is not ideal because two adjacent timesteps are always required for calculations, which means that when starting up the calculation, as well as defining the starting conditions of $\mathbf{r}(0)$ and $\mathbf{v}(0)$, the previous timestep's position $\mathbf{r}(0-\delta t)$ must also be defined.

An adjustment of the Verlet algorithm, which stores the full set of current values ($\mathbf{r}_i$, $\mathbf{v}_i$, and $\mathbf{a}_i$), and is hence 'self-starting' from the initial conditions of $\mathbf{r}(0)$ and $\mathbf{v}(0)$, is the Velocity Verlet algorithm of Swope *et al.* [109]. For the derivation, we reduce the second order differential equation (3.5) to two first order differential equations:

$$\dot{\mathbf{r}}_i(t) = \mathbf{v}_i(t), \tag{3.11}$$

and

$$\dot{\mathbf{v}}_i(t) = \mathbf{a}_i(t) = \frac{\mathbf{F}_i(\mathbf{r}_i(t))}{m_i}. \tag{3.12}$$

Using the Taylor expansion again we obtain an expressions for $\mathbf{r}_i(t+\delta t)$ and $\mathbf{v}_i(t+\delta t)$:

$$\mathbf{r}_i(t+\delta t) = \mathbf{r}_i(t) + \dot{\mathbf{r}}_i(t)\delta t + \frac{1}{2}\ddot{\mathbf{r}}_i(t)\delta t^2 + O(\delta t^3), \tag{3.13}$$

and

$$\mathbf{v}_i(t+\delta t) = \mathbf{v}_i(t) + \dot{\mathbf{v}}_i(t)\delta t + \frac{1}{2}\ddot{\mathbf{v}}_i(t)\delta t^2 + O(\delta t^3). \tag{3.14}$$

To obtain an expression for $\ddot{\mathbf{v}}$ we write the Taylor expansion of $\dot{\mathbf{v}}_i(t+\delta t)$:

$$\dot{\mathbf{v}}_i(t+\delta t) = \dot{\mathbf{v}}_i(t) + \ddot{\mathbf{v}}_i(t)\delta t + O(\delta t^2), \tag{3.15}$$

and

$$\ddot{\mathbf{v}}_i(t)\delta t = [\dot{\mathbf{v}}_i(t+\delta t) - \dot{\mathbf{v}}_i(t)] + O(\delta t^2). \tag{3.16}$$

We now substitute (3.11) and (3.12) into (3.13), and (3.16) into (3.14), and discard the higher order terms to obtain the final two equations for implementing the *Velocity Verlet* algorithm:

$$\mathbf{r}_i(t+\delta t) = \mathbf{r}_i(t) + \mathbf{v}_i(t)\delta t + \frac{1}{2}\mathbf{a}_i(t)\delta t^2, \tag{3.17}$$

$$\mathbf{v}_i(t+\delta t) = \mathbf{v}_i(t) + \frac{1}{2}\left[\mathbf{a}_i(t) + \mathbf{a}_i(t+\delta t)\right]\delta t. \tag{3.18}$$

The Velocity Verlet algorithm involves three steps. The first step requires the calculation of the velocities at the half time step:

$$\mathbf{v}_i\left(t + \frac{1}{2}\delta t\right) = \mathbf{v}_i(t) + \frac{1}{2}\mathbf{a}_i(t)\delta t. \tag{3.19}$$

The second step calculates the updated positions as given by Eq. 3.17. Then, the force is evaluated from the interatomic potential at the updated positions, to calculate the acceleration at $(t+\delta t)$. Finally, in the third step, the velocity at the full time step is calculated using:

$$\mathbf{v}_i(t+\delta t) = \mathbf{v}_i\left(t + \frac{1}{2}\delta t\right) + \frac{1}{2}\mathbf{a}_i\left(t + \frac{1}{2}\delta t\right)\delta t. \tag{3.20}$$

Now, both the positions and velocities at the current time are readily available. The Velocity Verlet algorithm is the most widely used integrator in MD simulations [107]. This is also the integration algorithm employed in this work.

As can be seen from the forms of integration algorithms, the choice of time step is a crucial component to MD simulations. The smaller the time step, the greater the computing power required for a given simulation length. However, too large of a time step will lead to errors in the trajectory and possibly 'explosions' where two

atoms get too close together and are strongly repelled apart [110]. Therefore, the ideal time step would be as large as possible while still avoiding these errors. This can vary between simulations but is typically $\sim 1\,\text{fs}$ (10^{-15} s).

3.2.3 Ensembles

The term statistical ensemble or ensemble is used describe the rules under which the system under study operates. This concept was introduced by Gibbs in 1902 [111] to connect atomic-scale properties such as the atom trajectories with macroscopic properties such as pressure and temperature. An ensemble is the collection of all possible configurations and momenta (microstates) defined by the same macroscopic parameters that are in statistical equilibrium. The most simple ensemble is the microcanonical ensemble which represents an isolated system where the number of atoms, N, the volume, V, and the energy, E, are all constant. This is also commonly known as the constant volume and energy (NVE) ensemble. It is important to note that it is the total energy (3.21) that remains constant; the kinetic and potential energies, K and U, of the system will still fluctuate:

$$E = K + U. \tag{3.21}$$

For simulations it is often desirable to be able to keep a constant temperature to enable a comparison to experimental results. This is not possible in the NVE ensemble where the kinetic energy of the system fluctuates:

$$k_B T(t) = \frac{1}{N} \sum_i m v_i^2, \tag{3.22}$$

where, k_B is the Boltzmann constant. This introduces the canonical (constant volume and temperature (NVT)) ensemble which has fixed number of atoms, N, volume, V, and temperature T. In this ensemble the temperature is controlled by exchanging energy with a thermostat. In addition to this there is the isothermal-isobaric (constant

pressure and temperature (NPT)) ensemble where pressure, P, is fixed instead of volume. This NPT ensemble often most closely resembles experimental conditions. There are numerous methods for implementing thermostats and barostats. In this work we employ the method, originally prepared Nosé [112] and further developed by Hoover [113]. This is an extended system method where fictitious degree of freedoms are introduced to represent the environment or external system alongside the real system. Here s is included to represent the heat bath. The potential energy of s is given by:

$$U(s) = (3N + 1)k_B T \ln s, \tag{3.23}$$

where, $(3N + 1)$ is the number of degrees of freedom and N is the number of particles. The kinetic energy is given by:

$$K(s) = \frac{Q(\mathrm{d}s/\mathrm{d}t)^2}{2}, \tag{3.24}$$

where, Q repesents a ficticious mass for the motion of s. With the assumption that the external system is microcanonical, the real system remains in a canonical state. The strength of the coupling between the real system and the heat bath is determined by Q.

3.3 Force fields

So far we have described calculating the positions and momenta of the atoms in the system assuming the forces are known. These known forces are described by the gradient of an interatomic potential, which describes the energy landscape of the material. This is also known as a force field. This is an empirical approach that approximates the bonding between atoms to allow the modelling of larger systems than possible with quantum mechanical methods. In this work, and in

many MD simulations, we employ a pair potential. A pair potential depends only on the interatomic separation between two ions i and j (r_{ij}). It does not include many-body interactions which involve increasingly complicated additions [114]. The interactions between atoms can be grouped into two areas: long-range interactions, and short-range interactions.

3.3.1 Long-range interactions

In order to form a solid or liquid material, an attractive force must be present between the atoms. This electrostatic interaction is given by Coulomb's law:

$$E_{\text{Coul}} = \frac{q_i q_j}{4\pi\epsilon_0 r_{ij}}, \tag{3.25}$$

where, ϵ_0 is the permittivity of free space, q_i and q_j are the charges on ions i and j. We can see that the Coulombic potential has a long range as it is a function of $\frac{1}{r_{ij}}$.

Modelling long-range interactions pose a problem in that they extend beyond the boundaries of the supercell into the periodic images, see Fig. 3.1. The Coulomb sum does not converge, leading to approximations becoming necessary. To circumvent the computing cost of achieving this by summing over many images of the supercell, we use a technique, originally designed by Ewald [115] in pre-computer times, that divides the significant part of the potential into short- and long-range contributions. Since this idea, there exists many developments on this concept which include the particle mesh ewald (PME) [116], the particle-particle particle-mesh (PPPM) [117], and the Wolf summation [118]. The last of these listed is the technique employed in this work. The Wolf summation builds on the Ewald summation with the use of error function switching, allowing smooth transitions between the short and long-range forces, ensuring the potential approaches zero beyond the cutoff distance, avoiding abrupt changes. The Wolf summation is designed with computational efficiency in mind, making it a popular choice for many MD simulations.

3.3.2 Short-range interactions

Equally, a short-range repulsion must be represented to prevent the atoms in our model from collapsing into each other. Considering that atoms are composed of a positively charged nucleus and negatively charged electron distribution, there is no net electrostatic interaction at a distance. However, if two atoms become close enough that their charge distributions overlap, there is an electrostatic repulsion between them. We must also consider the quantum mechanical effect of the Pauli exclusion principle, which states that two electrons cannot simultaneously occupy the same quantum state. To model this repulsive interaction the Born-Mayer potential [119] was developed:

$$E^{\text{B-M}}{}_{ij}(r) = A_{ij} \exp\left(-\frac{r_{ij}}{\rho_{ij}}\right), \tag{3.26}$$

where A_{ij}, and ρ_{ij} are potential parameters that define the characteristics of the interaction.

We must also consider London dispersion forces, commonly known as van der Waals forces, which act at the intermediate scale. These are forces which arise from the fleeting fluctuations in electron distribution, which create temporary dipoles that in turn induce other dipoles, resulting in a net attraction between particles. This interaction is described by the London dispersion equation:

$$E^{\text{London}}{}_{ij}(r) = \frac{c_{ij}}{{r_{ij}}^6} \tag{3.27}$$

where, c_{ij} is a variable potential parameter dependent on the crystal being modelled.

3.3.3 Interatomic potential for Li_2TiO_3

The Buckingham potential [120] was adapted from the popular Lennard-Jones potential [121–123] and describes the Pauli repulsion and the weak van der Waals

Table 3.1: Buckingham parameters of the potential used in this work [70].

Ion pair (ij)	A_{ij} (eV)	ρ_{ij} (Å)	c_{ij} (eV Å^6)
Li-Li	38533.955	0.100	0.00
Ti-Li	33089.570	0.127	0.00
Ti-Ti	31120.528	0.154	5.25
Ti-O	16957.710	0.194	12.59
Li-O	15465.549	0.167	0.00
O-O	11782.884	0.234	30.22

attraction. It replaces the repulsive term in Lennard-Jones with a Born-Mayer interaction to give:

$$E_{\text{Buck}} = A_{ij} \exp\left(\frac{r_{ij}}{\rho_{ij}}\right) - \frac{c_{ij}}{{r_{ij}}^6}. \tag{3.28}$$

When combined with the Coulomb interaction, the Buckingham potential describes ionic systems well and is in frequent use in MD simulations.

The empirical model employed in this work was developed by Vijayakumar *et al.* [70] using previous work by Matsui and Akaogi [124] for TiO_2 polymorphs. The long-range interactions are described by a Coulombic force, and the short-range interactions are described using the Buckingham potential (see Fig. 3.2). The form of this potential can be seen in Eq. 3.29:

$$U_{ij} = \frac{1}{4\pi\epsilon_0}\frac{q_i q_j}{r_{ij}} + A_{ij}\exp(-\frac{r_{ij}}{\rho_{ij}}) - \frac{c_{ij}}{{r_{ij}}^6}, \tag{3.29}$$

where, the values for the potential parameters previously defined can be seen in table 3.1.

As originally constructed this potential used the shell model of Dick and Overhauser [125] to describe the polarisability of the oxygen ion. However, the use of shells

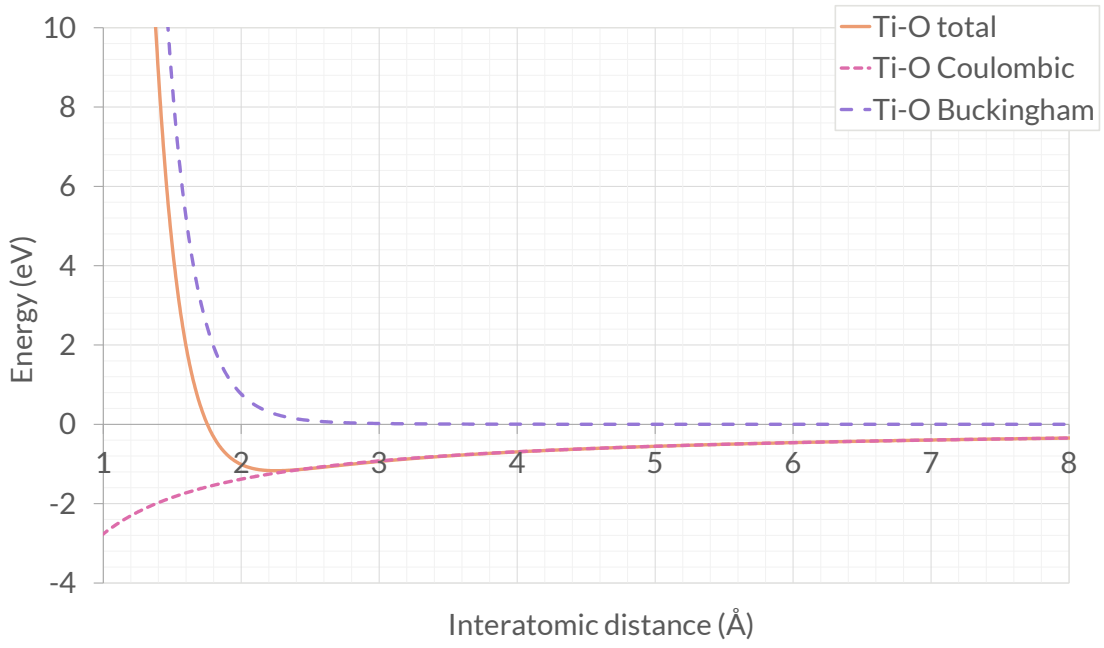

Figure 3.2: The interatomic potential used in this work, as developed by Vijayakumar *et al.* [70] for the Ti-O interactions.

in MD simulations requires either the arbitrary assignment of shell masses or energy minimisation of core-shell separations at each time step, which is computationally intensive. In the work in this thesis we assign partial charges to the Li, Ti, and O ions such that $q_{\mathrm{Li}} = 0.549e$, $q_{\mathrm{Ti}} = 2.196e$ and $q_{\mathrm{O}} = \text{-}1.098e$, where e is elementary charge. In table 3.2, the values of the lattice parameters and elastic constants as produced by the empirical model employed in this work (without shells) are shown, compared to valued obtained by the same empirical model when shells are included, an alternative empirical model, density functional theory, and experiment. A good agreement can be seen between both empirical models with the shells on or off, and between the empirical models, DFT, and experiment, demonstrating the efficacy of the model used. An alternative empirical model [126] is also shown in this table. This model displays fair agreement with the DFT and experimental results, though with greater deviation than the model employed in this work.

Table 3.2: Table of lattice parameters and elastic constants as obtained from the empirical model employed in this work with shells off, the same empirical model with shells on [66], another empirical model [126], density functional theory [66] and experiment [63].

Property	Emp (shells off)	Emp [66] (shells on)	Other Emp [126]	DFT [66]	Exp [63]
a /Å	5.10	5.07	5.12242	5.09	5.06
b /Å	8.85	8.80	8.88292	8.83	8.79
c /Å	9.48	9.51	10.00538	9.51	9.75
α /°	90.00	90.00	90.00	90.00	90.00
β /°	100.32	100.24	99.9866	100.25	100.21
γ /°	90.00	90.00	90.00	90.00	90.00
c_{11} /GPa	226.17	228.3	-	275.9	-
c_{12} /GPa	85.67	83.9	-	74.2	-
c_{13} /GPa	39.87	41.2	-	23.9	-
c_{15} /GPa	-5.96	8.9	-	22.4	-
c_{22} /GPa	219.93	223.8	-	269.3	-
c_{23} /GPa	40.09	40.9	-	24.2	-
c_{25} /GPa	15.56	11.8	-	25.0	-
c_{33} /GPa	116.28	123.3	-	209.2	-
c_{35} /GPa	2.34	2.2	-	2.4	-
c_{44} /GPa	34.41	37.4	-	57.5	-
c_{46} /GPa	14.70	11.0	-	23.2	-
c_{55} /GPa	33.83	37.0	-	56.8	-
c_{66} /GPa	68.69	71.8	-	103.9	-

3.4 Non-equilibrium molecular dynamics

An adaption to MD is Non-Equilibrium Molecular Dynamics (NEMD) where perturbed, non-equilibrium systems can be studied by artificially imposing gradients in order to study transport properties [102]. Thermal conductivity can be calculated using the Müller-Plathe method [127] in a NEMD simulation. The method calls for the division of the supercell into "chunks" along the direction of calculation (x, y, or z). Kinetic energy swaps are then performed between the hottest atom in the "cold chunk" and the coldest atom in the "hot chunk" (see Fig. 3.3). This is done by the literal swap of the velocity values of the atoms. The energy cost of performing each swap is logged as the process continues, repeating until a steady state temperature gradient is formed. The thermal conductivity can then be calculated using Fourier's law, as described in Eq. 2.11 [38].

The thermal conductivity of a material is made up of both phonon and electron contributions [128]. NEMD is most useful for materials such as ceramics, which are dominated by phonon conductivity, which is captured by MD. However, for materials such as metals, while the smaller phononic contribution to the thermal conductivity can be calculated, the large electronic conductivity component would be missed using solely MD.

Initially simulation supercells were equilibrated under NPT conditions for 50 000 timesteps of 2 fs. Simulations employed the Nosé-Hoover thermostat and barostat with relaxation times of 0.05 ps and 1.0 ps respectively. These values were chosen by first running a 5×5×5 supercell of Li_2TiO_3 in a NVT regime with a range of thermostat relaxation times for 10 000 timesteps, and observing the change in temperature with respect to time to ensure that the behaviour was not sinusoidal; which would have indicated that the thermostat is too strong. This arrived at a thermostat relaxation time of 0.05 ps. Then, with this chosen thermostat value, this was repeated in an NPT regime for 10 000 timesteps with various barostat relaxation

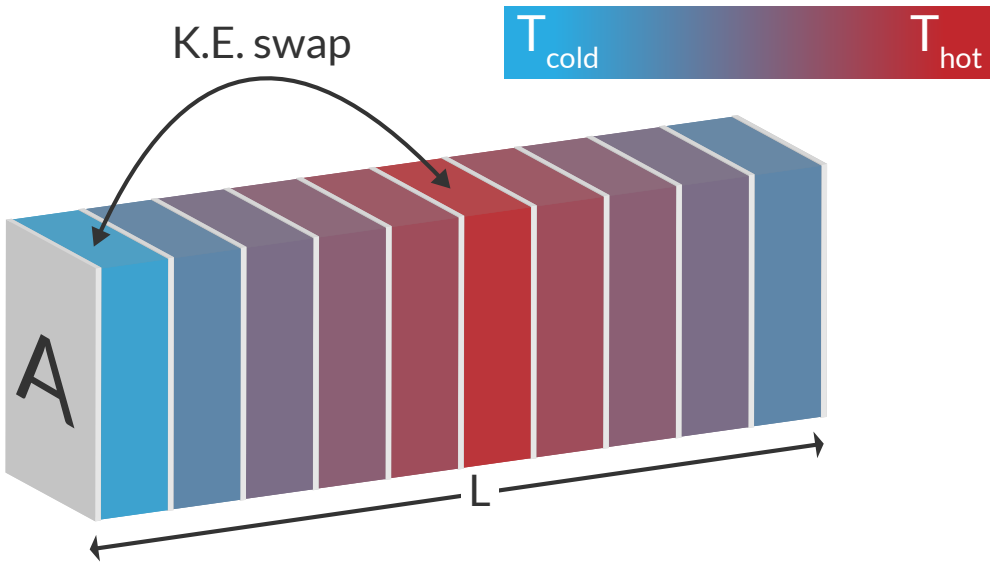

Figure 3.3: A supercell of length L and cross-sectional area A, in the Müller-Plathe method, where kinetic energy swaps are performed between the first chunk and centre chunk of the supercell, inducing a heat flux from the hot chunk (at temperature T_{hot}) to the cold chunk (at temperature T_{cold}).

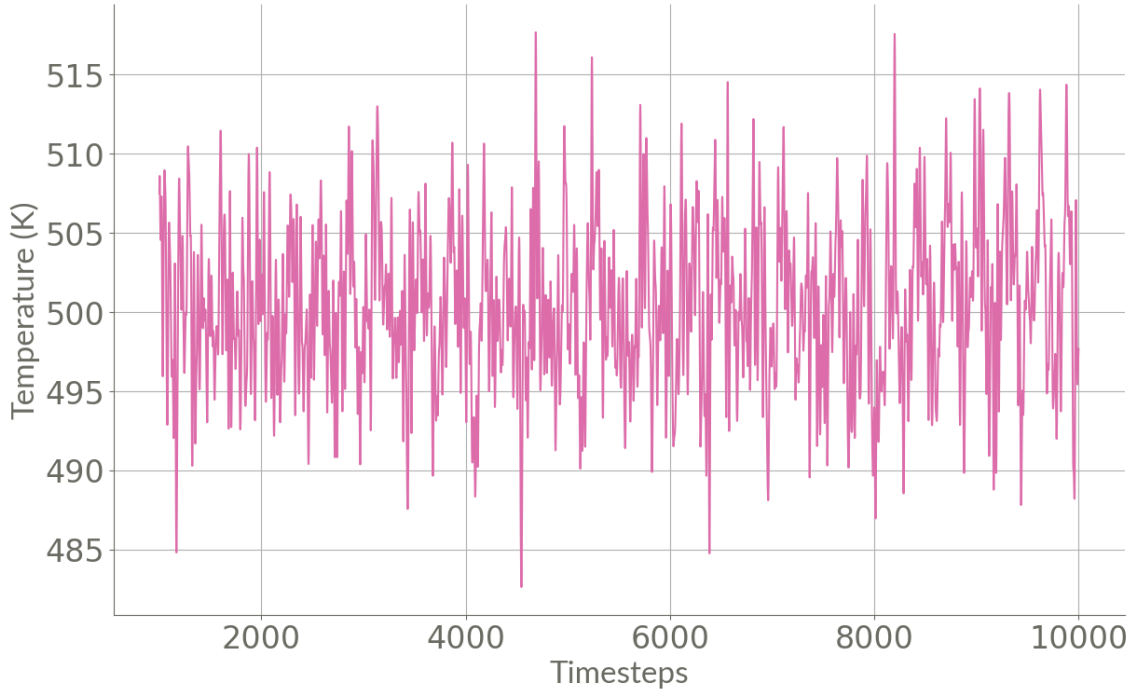

Figure 3.4: Temperature as a function of timestep for set temperature $T = 500$ K, in an NPT regime with thermostat and barostat relaxation times of 0.05 ps and 1.0 ps respectively. The first 1000 steps have been omitted to allow time for the system to reach equilibrium.

times, again checking the evolution of the temperature with time, to arrive at 1.0 ps. The temperature with respect to time for the final chosen NPT regime at $T = 500$ K is seen in Fig 3.4. For the second part of the simulation, kinetic energy swaps were performed every 10 timesteps under NVE conditions in the spatial direction of choice, with 20 "chunks" over which the gradient is formed. After at least 100 000 timesteps, to allow the system to form its gradient, the temperature of each chunk is recorded every 1000 time steps, from which the thermal conductivity calculation can be made using Fourier's Law (see Eq. 2.11).

Fig. 3.5 shows real temperature gradients induced in six simulations from 300–1100 K. From this it can be seen that well defined temperature profiles can be achieved with this method when suitably equilibrated.

As well as the Müller-Plathe method, there are several other MD techniques for

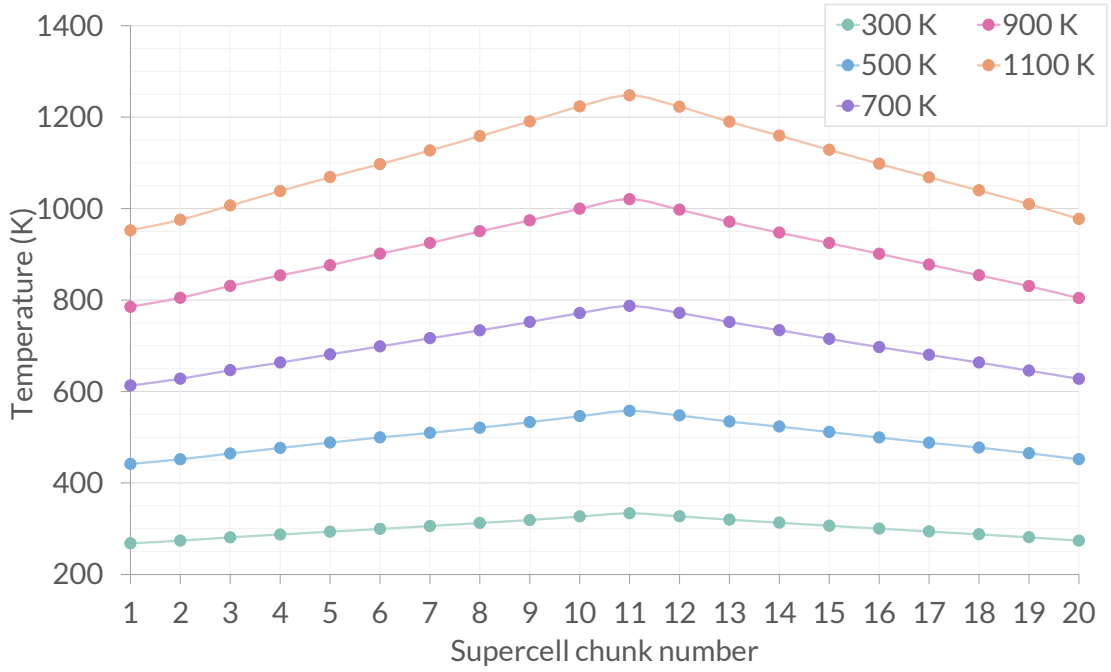

Figure 3.5: Temperature profiles of Li_2TiO_3, calculated for supercells of length, $L = 30$ unit cells, in the y-direction, for temperatures 300–1100 K. Where, chunk 1 is the cold chunk and chunk 11 is the hot chunk.

calculating the thermal conductivity. The most popular alternative is the Green-Kubo method. This method relates the auto-correlation function of the heat flux to the thermal conductivity. Green-Kubo typically requires longer to reach convergence which can make it more computationally expensive and sensitive to system size. For the purpose of this work, large simulation supercells are used to represent different defect types, leading to the Müller-Plathe method to be more suitable.

3.5 Extrapolation for the infinite cell

In crystalline structures, the calculated thermal conductivity is size dependent on the supercell. This regime is known as the Casimir limit [129], and is the result of phonon scattering at the interfaces of the hot and cold chunks due to the simulation supercell length L restricting the mean free path of the phonons [130], and thus limiting the thermal conductivity. In an ideal case, simulations would all be run with

large enough supercells to avoid this scattering effect. However, computational costs increase exponentially with increased cell size (i.e. the total number of atoms in the simulations). It is therefore not computationally feasible and another solution has been proposed and tested [130, 131] to successfully produce results in good agreement with experiment, using the relationship,

$$\frac{1}{k} \propto \frac{1}{L} \tag{3.30}$$

where, L is the length of the supercell in the direction of calculation (i.e L_x, L_y, and L_z), typically shown in this thesis in units of unit cells.

By calculating the thermal conductivity for each temperature of interest in a range of increasing supercell lengths, a "true" value for the thermal conductivity can be obtained by extrapolating the calculated thermal conductivity to $L \to \infty$, i.e. $\frac{1}{L} \to 0$. This would be the simple intercept of a graph showing inverse thermal conductivity, $\frac{1}{k}$ against inverse supercell length, $\frac{1}{L}$. This final calculated value would be comparable to experimental single crystal results.

3.6 Defect calculations

Once the lattice has settled into a state of equilibrium, we can examine how the introduction of defects affects the local environment. Ultimately, it is the behaviour of these defects that significantly impacts a material's performance. Defect energy can be defined as the energy difference between the perfect lattice and the lattice containing the defect. Early defect calculations, focusing on the introduction of charged defects, emphasised the necessity of computing the lattice's polarisation response to the presence of defects [132]. This idea was expanded by Mott and Littleton [133] who proposed dividing the lattice into two regions.

The Mott-Littleton method is a systematic approach to understanding the effects of defects in crystalline lattices. When a defect is introduced into an otherwise

perfect lattice, it disrupts the arrangement of surrounding ions, necessitating a relaxation process to achieve a new energy minimised configuration. Despite the potential field of the defect diminishing with distance as $\frac{1}{r}$, owing to its charge, the relaxation of nearby ions effectively shields the outer ions through polarisation. As the distance from the defect increases, the amount of relaxation diminishes rapidly. This characteristic allows for the lattice's description using the multi-region technique devised by Mott and Littleton.

In this method, the lattice is divided into concentric spherical regions (region I and region II), with the defect positioned at the centre. The region I encompasses the defect and is surrounded by ions initially arranged according to perfect lattice geometry. These ions are treated explicitly, i.e., their positions are shifted as determined by the interatomic potential. This explicit treatment is crucial due to the strong forces exerted by the defect on nearby atoms.

Beyond region I lies region II, where lattice relaxation is less pronounced. Here, a more approximate method can be employed. This region is further divided into region IIa and IIb (see Fig. 3.6). In region IIa, ions are displaced according to forces approximated by Mott-Littleton. However, the positions of ions within region IIb, extending infinitely, remain unaltered in response to the defect. The energy of the interaction with the defect in this region is determined directly from the Mott-Littleton approximation.

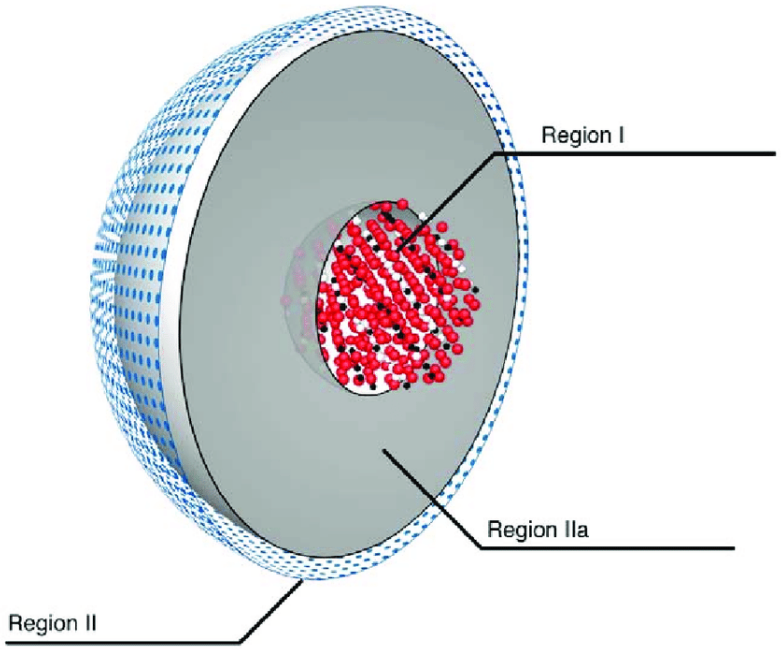

Figure 3.6: Representation of the Mott-Littleton regions [134].

4

Perfect Li_2TiO_3

This work has previously been published in Fusion Engineering and Design [135].

4.1 Introduction

To begin work on calculating the effect of defects on heat transfer in Li_2TiO_3, we characterise the perfect crystal to set a baseline for direct comparison to later chapters and to complement the available literature. In earlier chapters the anisotropy of the crystal structure of Li_2TiO_3 and the likelihood of measuring different values along different axes was discussed. In this chapter we measure the thermal conductivity along the three spatial directions and investigate the differences based on the differing crystal structures along these axes.

The perfect crystal is defined as the Li_2TiO_3 unit cell, and can be seen to be comparable to single crystal experiments. The absence of defects allows for a deeper understanding of the intrinsic properties of materials.

4.2 Methodology

4.2.1 Molecular dynamics parameters

For MD simulations it is essential to choose an appropriate timestep. The timestep must be at least one order of magnitude smaller than the fastest timescale in the system. This is because too large of a timestep can cause the simulation to become unstable as the positions of two atoms can become close to overlapping. Common timesteps for MD are in the order of 1 fs. After comparing results from 1 fs and 2 fs and finding no issues with the simulation, for this work we use a timestep of 2 fs to better utilise limited computational resources.

The perfect crystal thermal conductivity simulations were run as follows. The simulations were equilibrated under NPT conditions for 50 000 timesteps of 2 fs. This figure was chosen after studying plots of the temperature with respect to time during equilibration and becoming certain equilibration had been achieved in this time. Simulations employed the Nose-Hoover thermostat and barostat with relaxation times of 0.05 ps and 1.0 ps respectively. Then, for the second part of the simulation, kinetic energy swaps were performed every 10 timesteps under NVE conditions in the spatial direction of choice, with 20 "chunks" over which the gradient is formed for 50 000 timesteps. In the third stage, the temperature of each chunk is recorded every 1000 time steps for the rest of the simulation time in the same conditions, to allow the system to form its temperature gradient. Initial simulations suggested that the previous 50 000 timesteps would be sufficient to stabilise the temperature gradient, and an average of the gradient over the next 100 000 timesteps was used. However, depending on the size of the simulation supercell, the temperature gradient takes longer to stabilise. The temperature gradient with respect to time was studied to ensure it had converged by at least the final 100 000 timesteps, leading to increased number of timesteps for larger simulations. The average of the final 100 000 timesteps

is then taken as the average temperature gradient for the simulation, and from this the thermal conductivity calculation can be determined using Fourier's Law (see Eq. 2.11). Due to the small statistical variation, averaging over fewer than 100 000 timesteps would also produce an acceptable result. The figure of 100 000 timesteps best utilised available computational resources at the time and mitigated the risk of needing to repeat simulations where the gradient did not converge within the given time.

The temperature profile was checked for each simulation to ensure the temperature gradient has converged, i.e. that the difference between the hot and cold chunks had stabilised. This led to differing total simulation time for different supercells in an effort to maximise efficient use of computational resources while still obtaining high quality results.

4.2.2 Minimum cell-size and convergence time-scales

To gain reliable results from simulations, a number of parameters that must be considered, including the cross-sectional area of the supercell and the number of time steps used to establish a convergent temperature gradient. Running simulations with larger supercells (more atoms) or longer simulation run times can become very computationally expensive, requiring minimisation of cost while ensuring the accuracy of the data. Here illustrated is the testing used to determine the appropriate simulation supercell cross-section size and simulation run time.

The dependence on cross-sectional area was examined first. This was done by calculating the thermal conductivity for supercell cross-sections of 5×5, 10×10, and 20×20 unit cells. From Fig. 4.1, the effect of increased cross-section of the simulation supercells on the temperature gradient can be seen. With a larger cross-sectional area, a gentler temperature gradient is induced (see Fig. 4.1). This reduces potential adverse effects such as the hot chunk passing the melting point of the material, which would create an unphysical scenario for the model. By studying these effects, and the

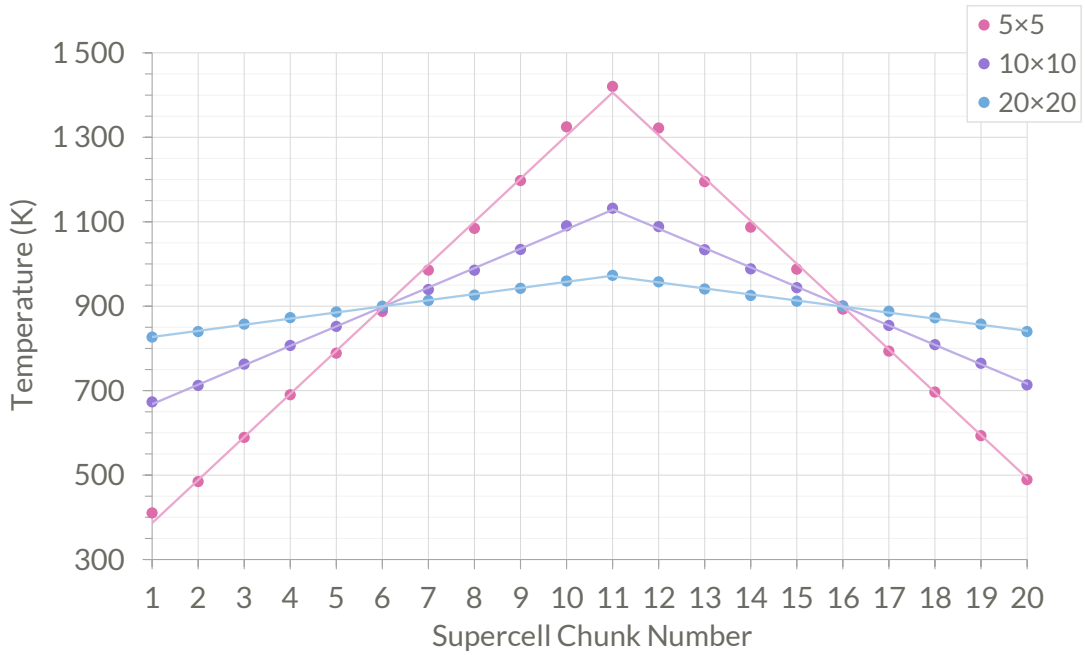

Figure 4.1: The temperature profiles induced using NEMD with increasing cross-section sizes of 5×5, 10×10 and 20×20 unit cells of supercell length $L = 40$ unit cells and simulation run time of 100 ps, for the $T = 900$ K data set calculations along the y-direction.

resulting thermal conductivity values calculated, a cross-sectional area of 10×10 unit cells was found to be sufficient for this work as it provided a similar value for the thermal conductivity as the larger and more expensive 20×20 supercell. Due to the anisotropic crystal structure the actual cross-sectional area differs depending on the direction along which the supercell is elongated for thermal conductivity calculation while keeping the same number of atoms. The difference between the areas can be seen in Fig. 4.2.

The simulation length over which the kinetic energy swaps take place directly relates to the quality of the temperature profile induced, until such a point that a steady state temperature gradient is formed. To ensure this work contains converged values for the thermal conductivity, simulations were run for a range of increasing simulation lengths, until convergence was ensured in each of the three spatial directions. When the the temperature gradient begins to be induced, the temperature profile

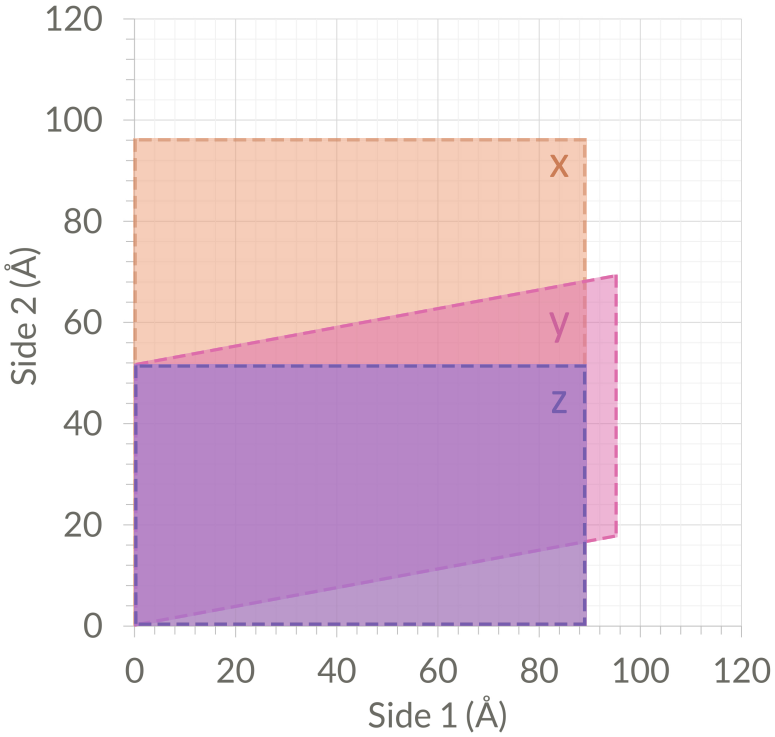

Figure 4.2: Comparison of cross-sectional area along each studied axis.

displayed a curved trend rather than the desired straight line profile. Eventually with enough time a steady state straight-line temperature gradient is formed as seen in Fig. 4.4.

The difference in crystal structure of Li_2TiO_3 affected how quickly a steady state temperature gradient was induced in each direction. Most notably the z direction requires significantly more time on average ($\sim$500 ps) than x or y ($\sim$200 ps) to achieve convergence, see Fig. 4.5. There is notably also a positive correlation between the length, L, of the supercell and the time required for convergence. Fig. 4.4 shows the convergence of the temperature profiles of simulations of supercell length $L = 100$ unit cells in the z-direction. To maximise the use of computational resources this was accounted for to ensure all data produced in this work is well converged by giving all the largest $L = 100$ unit cells simulations twice as long to run (i.e. simulations along x and y were run for 500 ps and along z for 1200 ps). Final simulation run times for thermal conductivity calculations along all axes can be found in table 4.1.

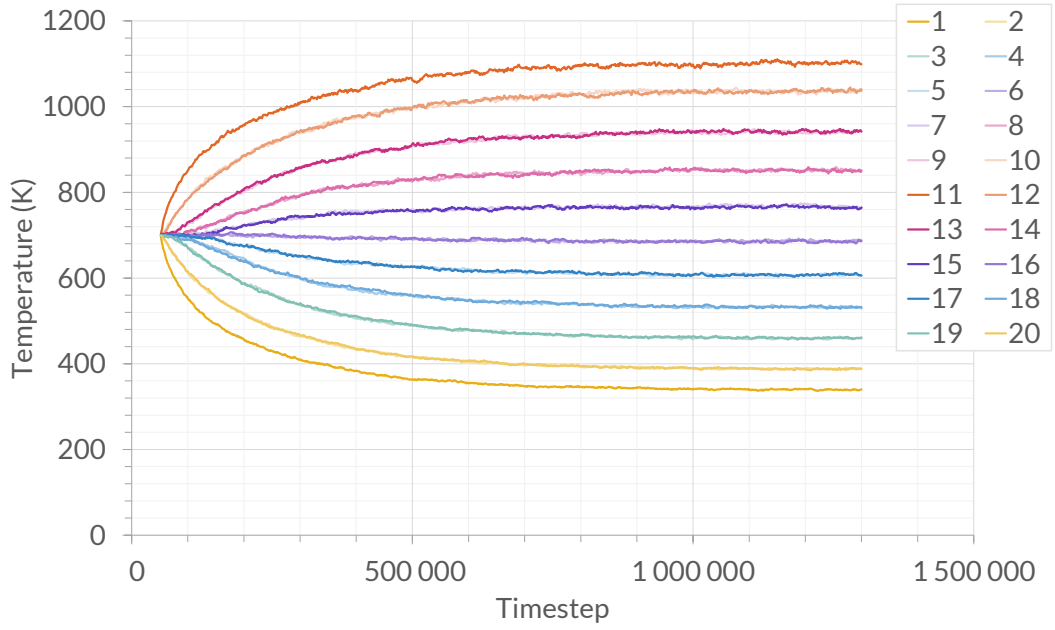

Figure 4.3: The temperature of each Müller-Plathe chunk with respect to time in the simulation for a simulation with a supercell of length $L = 100$ unit cells along the z-direction at 700 K.

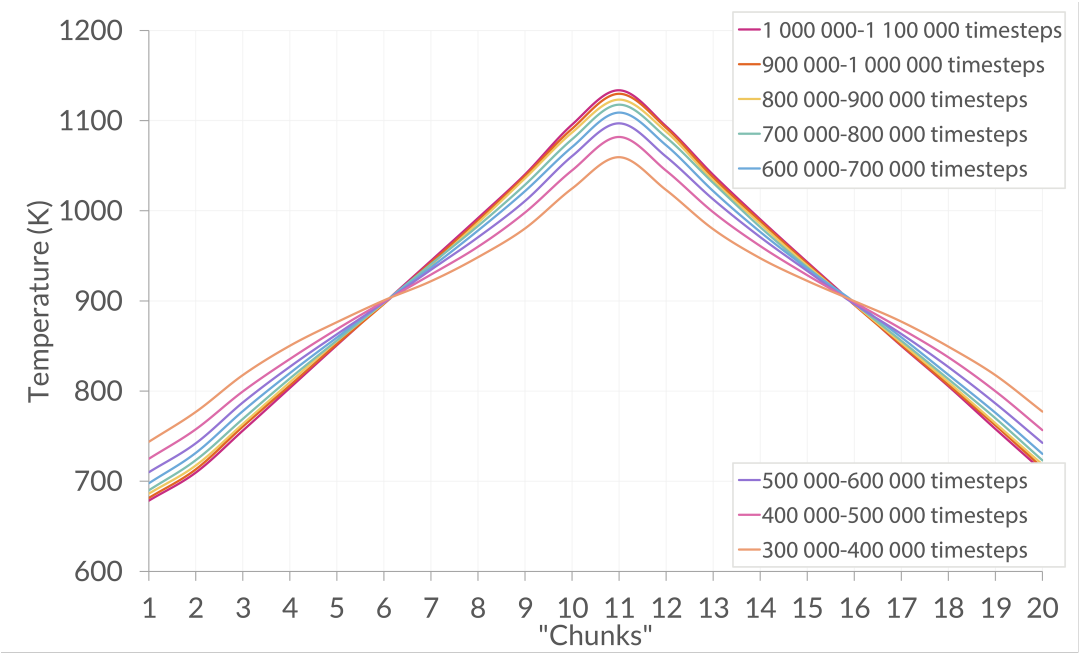

Figure 4.4: The calculated average temperature profile over 100 000 timesteps, every 100 000 timesteps for a simulation with a supercell of length $L = 100$ unit cells along the z-direction at 700 K.

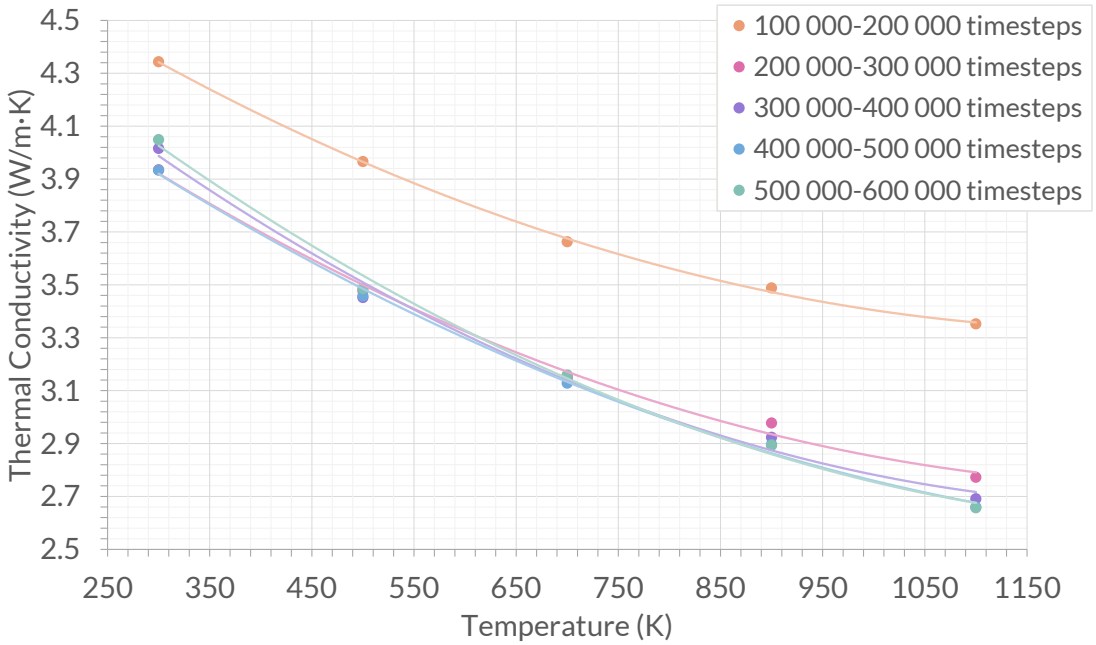
100 000-200 000 timesteps
200 000-300 000 timesteps
300 000-400 000 timesteps
400 000-500 000 timesteps
500 000-600 000 timesteps
Thermal Conductivity (W/m·K)
4.5
4.3
4.1
3.9
3.7
3.5
3.3
3.1
2.9
2.7
2.5
250
350
450
550
650
750
850
950
1050
1150
Temperature (K)

(4.5a) x

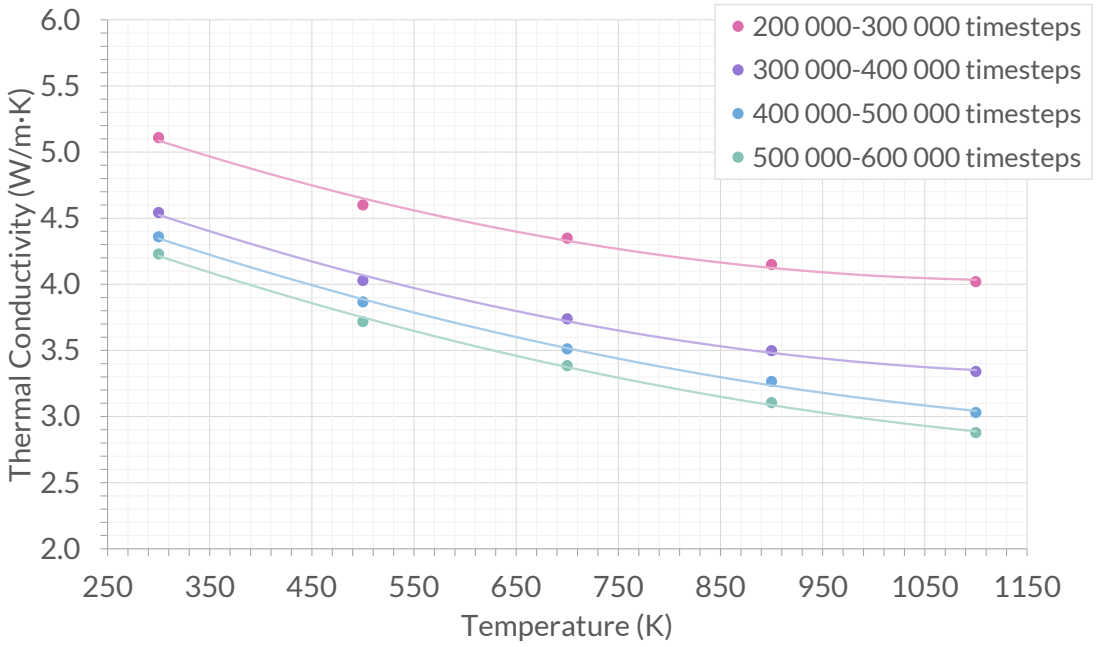
200 000-300 000 timesteps
300 000-400 000 timesteps
400 000-500 000 timesteps
500 000-600 000 timesteps
Thermal Conductivity (W/m·K)
6.0
5.5
5.0
4.5
4.0
3.5
3.0
2.5
2.0
250
350
450
550
650
750
850
950
1050
1150
Temperature (K)

(4.5b) y

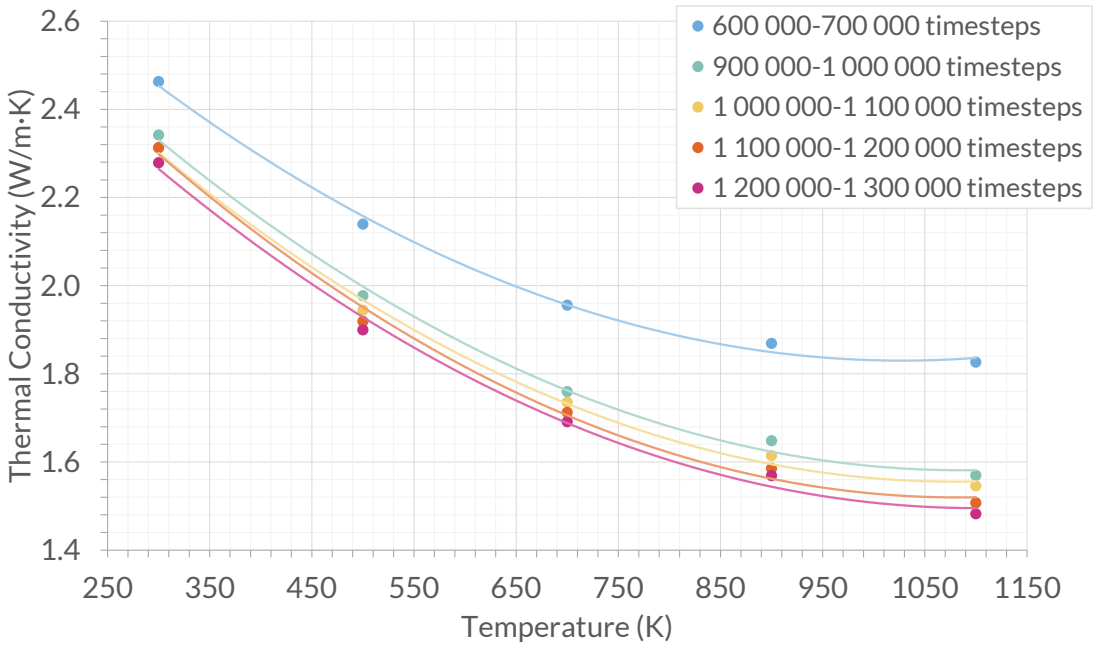

(4.5c) z

Figure 4.5: Plot of the calculated thermal conductivity along each axis, (a) x, (b) y, and (c) z, as a function of temperature over a range of simulation time lengths until convergence, for $L = 100$ unit cells supercell lengths. The legend shows the simulation timestep range used for the temperature gradient calculation.

Table 4.1: Overview of the simulation parameters for different axes, supercell lengths in units of unit cells, and temperatures (300–1100 K) for calculating the extrapolated thermal conductivity of the perfect crystal of Li_2TiO_3, for a total of 60 simulations.

Axis	L (unit cells)	No. of atoms	No. of temperatures	Equil. time (timesteps)	NEMD time (timesteps)	Total time (timesteps)
x	30	144 000	5	100 000	200 000	300 000
	40	192 000	5	100 000	200 000	300 000
	50	240 000	5	100 000	200 000	300 000
	100	480 000	5	100 000	500 000	600 000
y	30	144 000	5	100 000	200 000	300 000
	40	192 000	5	100 000	200 000	300 000
	50	240 000	5	100 000	500 000	600 000
	100	480 000	5	100 000	500 000	600 000
z	30	144 000	5	100 000	500 000	600 000
	40	192 000	5	100 000	600 000	700 000
	50	240 000	5	100 000	1 000 000	1 100 000
	100	480 000	5	100 000	1 200 000	1 300 000

4.3 Results and discussion

4.3.1 Thermal Conductivity

In Fig. 4.6 the calculated thermal conductivity at each supercell length with respect to temperature is shown compared to the extrapolated value. We can see the importance of the extrapolation procedure by how much the thermal conductivity increases compared to even the largest simulation supercells.

Shown in Fig. 4.7 is the inverse of the thermal conductivity as a function of the inverse of the supercell length in the direction of interest, at a series of temperatures. The straight line trends obtained enable the extrapolation of the thermal conductivity in each direction, to represent the infinite cell.

The extrapolation was performed for all three spatial directions, allowing for calculation of the thermal conductivity in x, y, and z to be displayed in Fig. 4.8. From this the anisotropy of the thermal conductivity of Li_2TiO_3 can be clearly observed. The x, and y thermal conductivities remain similar to each other, while the z-direction thermal conductivity is markedly lower than both. The origin of this anisotropy is due to the crystal structure of the host material. The crystal structure of Li_2TiO_3 along z differs greatly from the more similar structures of x and y. There is very clear bonding in the xy-plane but not between the layers along z (the lithium L_6 layer, the oxygen O_6 layer and the mixed cation layer of Li_2Ti_4, see. Fig. 2.14). The difference in bonding along z appears to inhibit thermal transport and thus lower the thermal conductivity. This may be due to increased phonon scattering along the path of the bonding in z (see Eq. 2.13 for the relationship between thermal conductivity and the elastic tensor). Kataoka *et al.* measured the thermal conductivity of a single crystal, finding the thermal conductivity in z as being $0.93\,\mathrm{W/(m \cdot K)}$ at $294\,\mathrm{K}$, that is, much lower than the reported value for Li_2TiO_3, implying strong anisotropy [63]. This observed lower thermal conductivity may also account for why simulations along

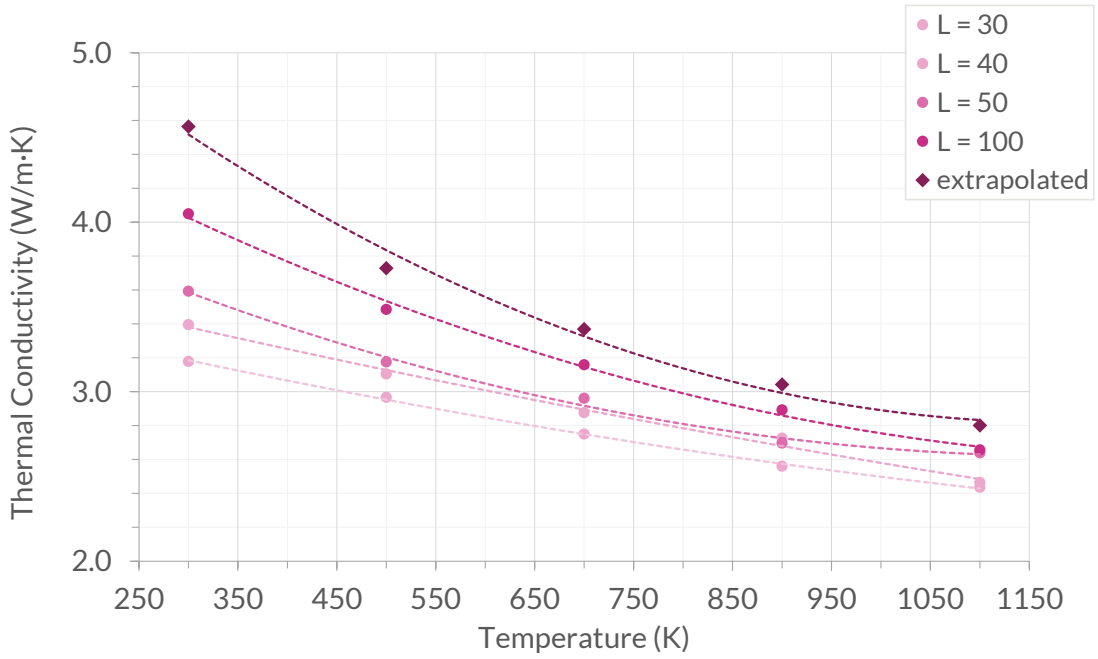
L = 30
L = 40
L = 50
L = 100
extrapolated
Thermal Conductivity (W/m·K)
5.0
4.0
3.0
2.0
250
350
450
550
650
750
850
950
1050
1150
Temperature (K)

(4.6a) x

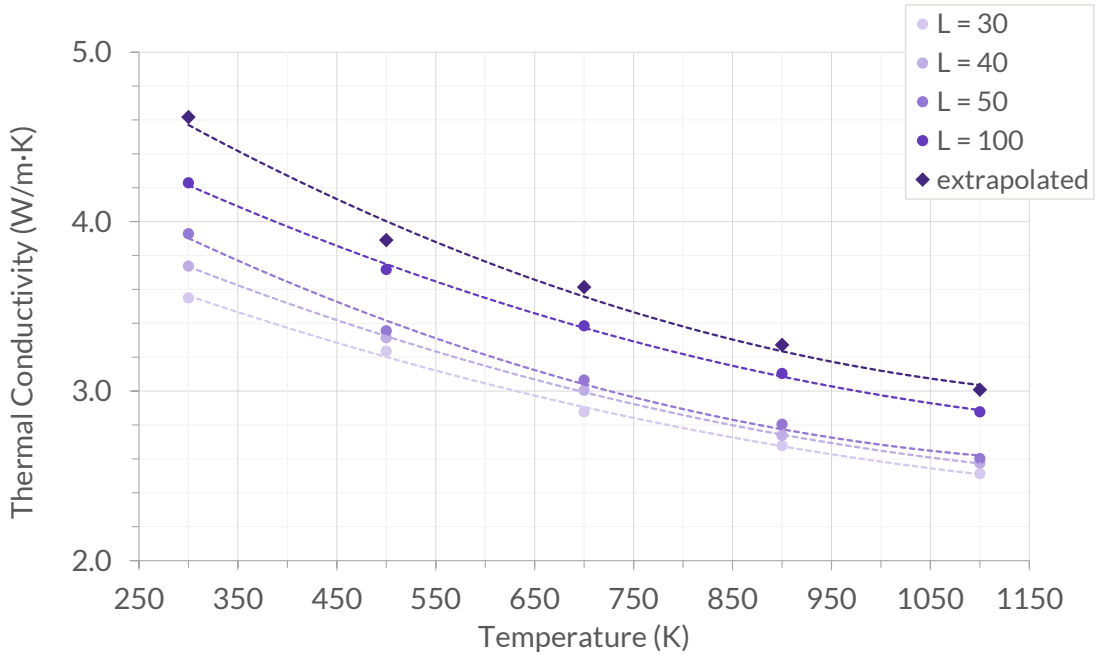
L = 30
L = 40
L = 50
L = 100
extrapolated
Thermal Conductivity (W/m·K)
5.0
4.0
3.0
2.0
250
350
450
550
650
750
850
950
1050
1150
Temperature (K)

(4.6b) y

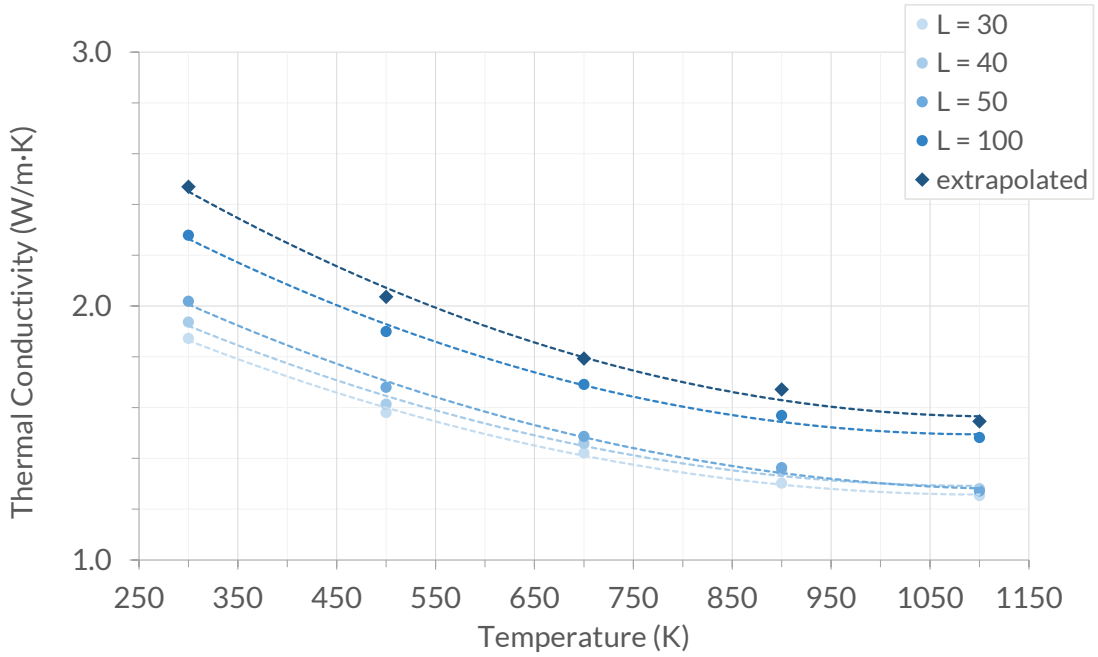

(4.6c) z

Figure 4.6: Figures showing the calculated thermal conductivity at each supercell length in each spatial direction (a) x, (b) y, and (c) z.

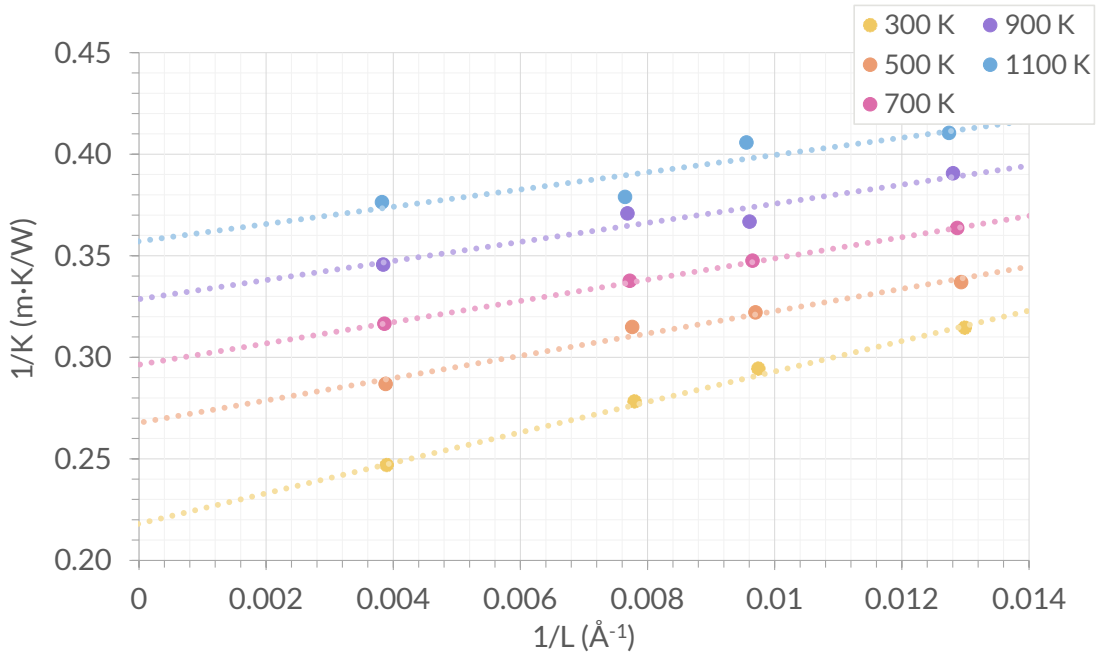

(4.7a) x

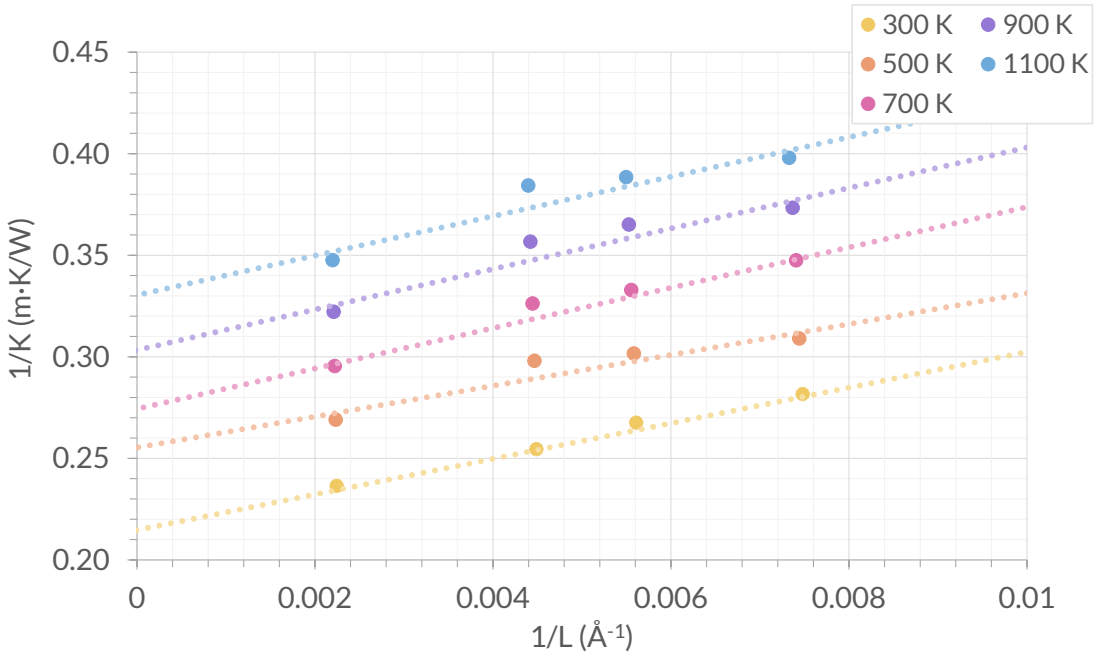

(4.7b) y

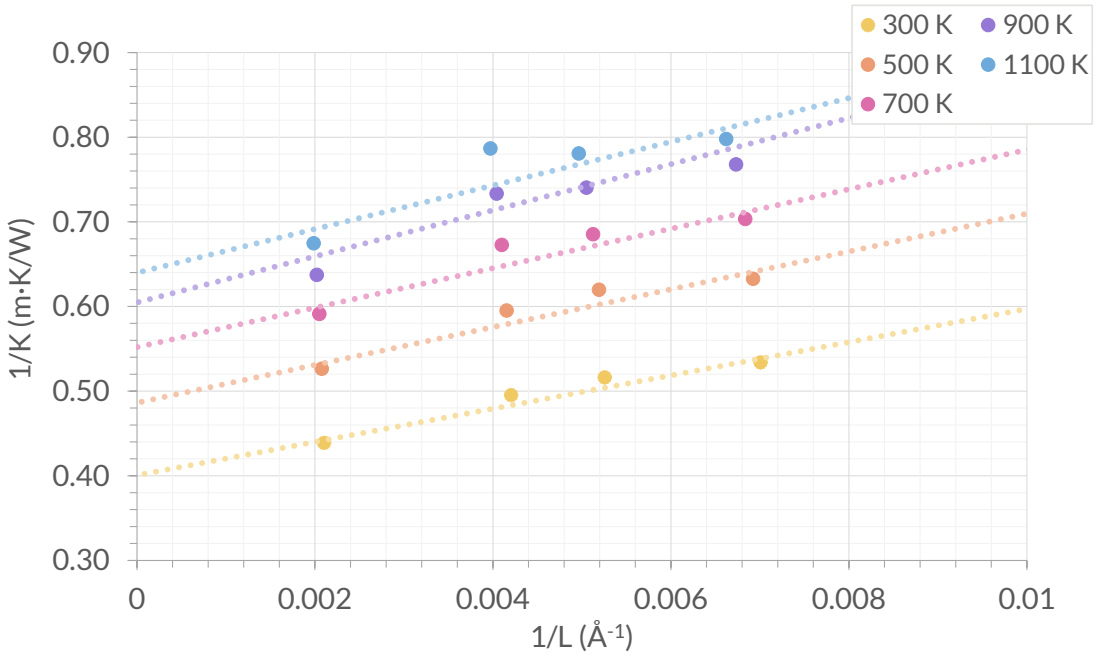

(4.7c) z

Figure 4.7: The inverse thermal conductivity in, (a) x, (b) y, and (c) z, as a function of inverse supercell-length L in Å, the intercept of which is the inverse of the thermal conductivity of the infinite cell.

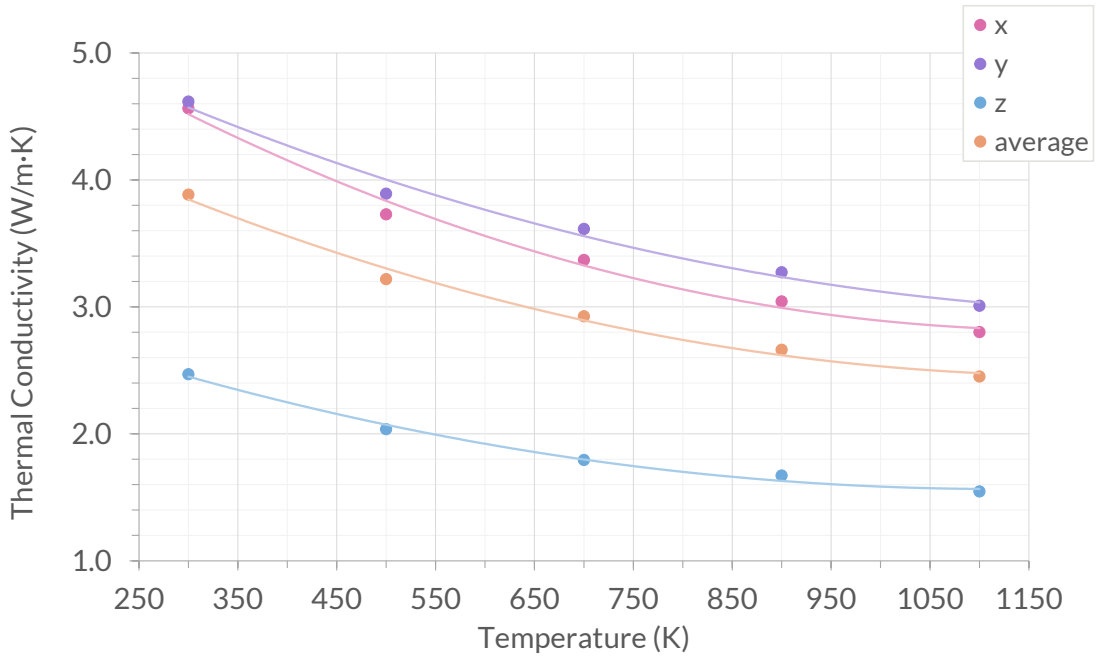

Figure 4.8: The extrapolated thermal conductivity in x, y, and z, along with the average thermal conductivity.

z required longer to achieve a steady state temperature gradient, as was found when checking the convergence of simulations (section 4.2.2).

Alongside these data, the average (arithmetic mean) of the extrapolated thermal conductivity of Li_2TiO_3 is shown. These are the values most comparable to those from the experiment, where the grains of Li_2TiO_3 are randomly orientated. The general trend in thermal conductivity is that it decreases with increasing temperature, as is the case for most materials [128]. It can also be seen from Fig. 4.8 how much the lower thermal conductivity along z lowers the average thermal conductivity, illustrating the magnitude of its influence.

There have been a number of studies of the thermal conductivity of Li_2TiO_3. The data show considerable variation depending on the size of the pebbles, grain size, density of the material, and the particular chemical composition chosen for study. A summary of the existing data for the thermal conductivity of Li_2TiO_3 has been reproduced in Fig. 4.9. It is hard to draw many conclusions based on the

data presented in Fig. 4.9. Davis and Haasz [136], and Saito *et al.* [137] investigate the thermal conductivity of pebbles of Li_2TiO_3, similar to those that will be used in a breeder blanket design. Saito *et al.* used 8 mm diameter by 2 mm thickness pellets of three densities, here plotted for comparison is 83% TD. Hoshino *et al.* [138] investigates non-stoichiometric compositions of Li_2TiO_3. In Fig. 4.9 it is the thermal conductivity of $95Li_2TiO_3$, i.e. where the molecular ratio of Li_2O over TiO_2 is 0.95 (lithium deficient), that is plotted. One might anticipate that the non-stoichiometric material would have a lower thermal conductivity, due to the introduction of point defects which act as phonon scattering centres. However, Hoshino *et al.* found the thermal conductivity to be higher than for the stoichiometric Li_2TiO_3 found by Saito *et al.* This highlights one example of the complex nature of Li_2TiO_3, and the clear need for further study. Another feature seen in the experimental data from Saito *et al.* and Davis and Haasz is a small increase in the thermal conductivity at high temperature. Though the phonon thermal conductivity (as calculated in this work) is anticipated to drop with temperature, the photon conductivity is shown to slightly increase [139]. This change can be significant however it depends on the particular composition of the sample. It may be that the samples used in Saito *et al.* and Davis and Haasz are seeing an upturn in the photon conductivity at high temperature. As well as these experimental results, the thermal conductivity of Li_2TiO_3 was calculated by DFT, along with a non-analytical term correction, in Samolyuk and Edmondson [140]. This thermal conductivity is significantly lower at higher temperatures than those observed in experiment, and does not observe the increase in thermal conductivity at high temperature seen in some experimental results.

The average thermal conductivity calculated in this chapter can now be compared with the experimental results, as seen in Fig. 4.9. The values for thermal conductivity found in this chapter are consistently higher than those shown in the experiment. This is to be expected, as the simulations of this work do not include any of the defects

found in real Li_2TiO_3, such as grain boundaries, where phonon scattering lowers the thermal conductivity. Overall, the trend of the thermal conductivity follows the experimental data, with the exception of experiments in which the thermal conductivity was found to decrease initially and then rise again with increased temperature, which could originate from impurities in the crystal structure not captured in the present simulations. This could suggest that this distinct behaviour is not inherent to the pure crystal structure, which would be expected to be observed in this chapter.

4.4 Summary

In this chapter the thermal conductivity of stoichiometric, single crystal Li_2TiO_3 has been examined, highlighting how the complex underlying crystal structure results in highly anisotropic heat transfer in the material. The overall thermal conductivity of the material is predicted to be slightly higher than experimental observations, but this is expected as the current model neglects the impact of defects (including grain boundaries) and impurities. The results suggest that thermal conductivity in the z direction (the direction in which the crystal structure alternates between Li, O and $LiTi_2$ (111) planes) is roughly half that predicted in the x and y directions where planes are homogeneous. This interesting characteristic could potentially be exploited using methods of creating breeder blankets where the crystal structure of all grains of Li_2TiO_3 are favourably aligned to give the blanket a higher thermal conductivity than the average for the material. Current solid breeder blanket designs utilising pebbles do not make use of selectively orienting crystal structure. With the foundation of the calculated thermal conductivities of the perfect crystal, further work will proceed with the effect of defects on the thermal conductivity of Li_2TiO_3. Beginning with the investigation of point defects as found in non-stoichiometric Li_2TiO_3 and how they affect the thermal conductivity in the next chapter.

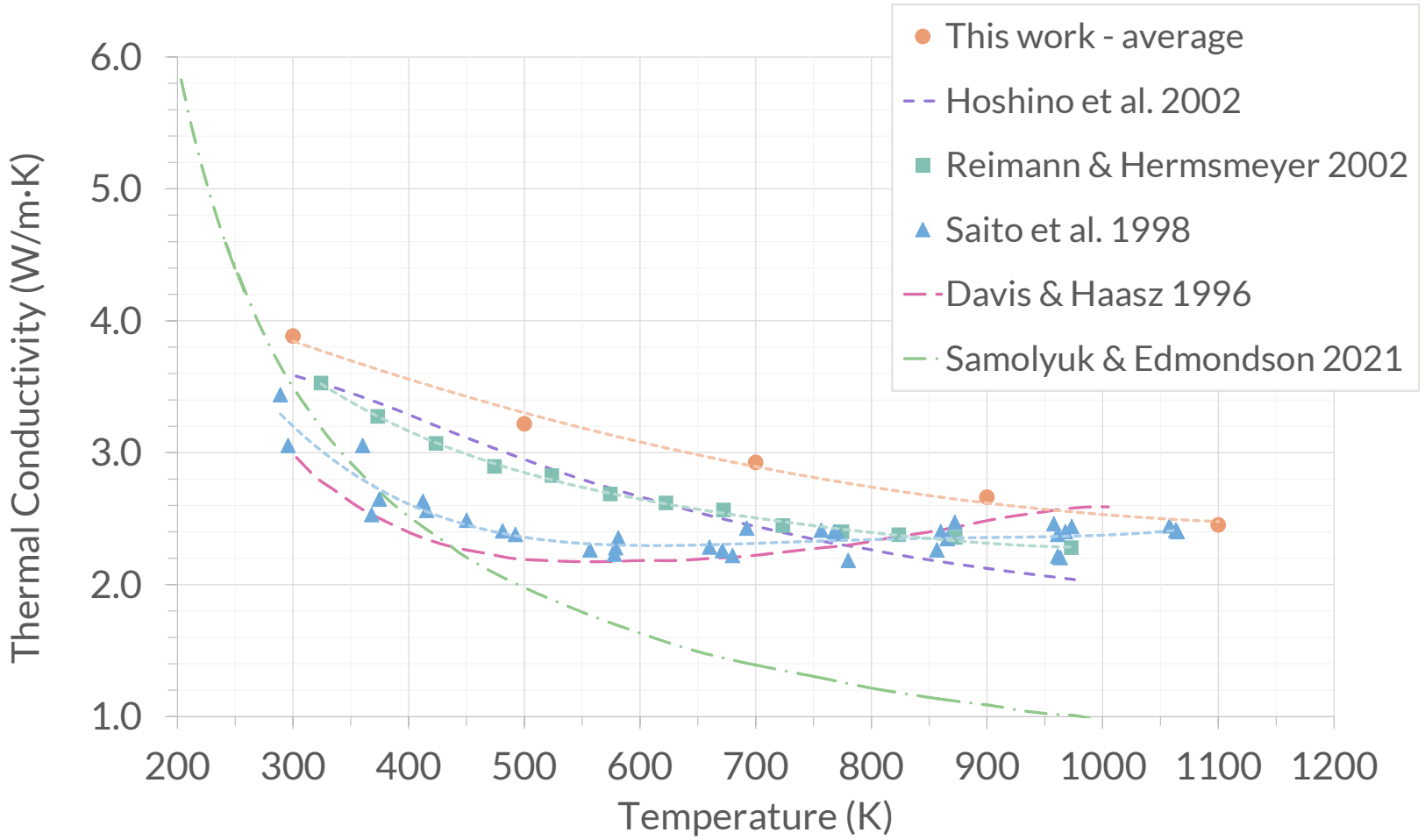

Figure 4.9: The extrapolated thermal conductivity compared with current experimental data [136–138, 140, 141].

5

Non-stoichiometric Li_2TiO_3

This work has previously been published in Journal of Nuclear Materials [142]

5.1 Introduction

The transfer of heat through the breeder region of a future fusion reactor is a key component of its thermal efficiency. Development of advanced ceramic breeder materials based on Li_2TiO_3 seek to exploit its ability to accommodate significant non-stochiometry, however, it is not clear how deviations from the 50:50 mix of Li_2O and TiO_2 will affect key properties of the material, including the thermal conductivity. Therefore, in this chapter MD simulations are employed to examine how the thermal conductivity of Li_2TiO_3 changes with stoichiometry.

To ensure the whole fusion process is sustainable it is essential to be able to recover at least one tritium from the blanket for each fusion reaction occurring in the plasma (in practice, it will be necessary for the tritium breeding ratio (TBR) to be somewhat above one to allow for engineering losses in the fuel cycle). The design of the blanket and the selection of materials from which it is to be constructed is therefore a critically important part of a future fusion power station. There have

been a number of different concepts developed for the breeder blanket which has been discussed in Chapter 2.

According to the phase diagram of the Li_2O/TiO_2 system [58, 60] (see Fig. 2.13), we see that β-Li_2TiO_3 has a compositional homogeneity range of 47 to 51.5 mol% TiO_2. This compositional flexibility has been exploited in the development of advanced ceramic breeder materials such as $Li_{2+x}TiO_{3+y}$ [100, 138, 143, 144], where the increase in lithium density results in improved tritium breeding performance. During operation, lithium will undergo transmutation to generate tritium for the plasma and so the material will be increasingly Li deficient as it ages; Li burn-up may reach several % during a typical blanket lifetime [145]. Therefore, it is important to be able predict the thermal conductivity of the titanate across a wide stoichiometric range.

The exact mechanisms by which any non-stoichiometry will be accommodated has been examined widely in the literature. A number of different mechanisms have been proposed for accommodation of a lithium excess. Hao *et al.* [146] and Bian and Dong [147] propose that a lithium excess is accommodated by titanium vacancy V_{Ti}^{4-} defects charge compensated by oxygen vacancies. These defects can be represented using Kroger-Vink notation as V_{Ti}^{4-} and V_{O}^{2+}, where the V indicates a vacancy defect on a site indicated by the subscript. The defect's relative charge is indicated in the superscript [148]. At smaller deviations from stoichiometry Hao *et al.* propose that the Li_i^{1+} defect is the dominant defect for incorporating the lithium excess. This suggestion is supported by the diffraction data of Mukai *et al.* who also suggest the presence of the $\mathrm{Li}_{\mathrm{Ti}}^{3-}$ antisite defect (i.e. where Li sits in a Ti site), which is charge compensated for by reduction of Ti [149]. The presence of lithium substitution onto titanium sites is also supported by the DFT simulations of Murphy and Hine [67]. There is less disagreement regarding the identification of the dominant defects on the lithium deficient side of the phase diagram, with Yu *et al.* [150] and Murphy and Hine [67] proposing the $\mathrm{Ti}_{\mathrm{Li}}^{3+}$ defect charge compensated for by V_{Li}^{1-} defects.

Vitins *et al.* also suggest that the some of the lithium sites become substituted by titanium [151].

Previous studies of the thermal conductivity of Li_2TiO_3 have shown significant variation arising due to different pebble sizes, densities and compositions [136, 137, 141]. Interestingly, the thermal conductivities determined by Hoshino [138] and Roux [152] for lithium deficient Li_2TiO_3 are greater than values previously determined for the stochiometric material. Similarly, Mukai *et al.* observe an increased thermal diffusivity for lithium rich samples [149]. As stated above, the introduction of an increased concentration of point defects to accommodate this non-stoichiometry would be expected to reduce the thermal conductivity and diffusivity. Mukai *et al.* argue that the origin of the increase is due to the microstructure, as the Li-rich samples are much closer to the theoretical density, and not the thermal conductivity through the grains themselves [149]. Therefore, this still leaves the question of how significant the change in the thermal conductivity in the fuel grains themselves is.

As discussed above the previous experiments attribute the increase in the thermal conductivity/diffusivity to changes in the microstructure that arises for the different stoichiometries. This makes it difficult to determine how the thermal conductivity will change in a pebble that starts with the microstructure corresponding to an Li-rich or stoichiometric composition and then moves to become lithium deficient. This type of information can be determined with an atomic resolution using atomistic simulation techniques, like MD. Classical MD has already been employed to demonstrate the highly anisotropic thermal conductivity in the previous chapter. Therefore the aim of this work is to use MD to understand how the introduction of non-stoichiometry changes the thermal conductivity of bulk Li_2TiO_3.

5.2 Methodology

Determination of how changes in stoichiometry will affect the thermal conductivity of Li_2TiO_3 will be achieved in two steps. In the first step we will use lattice statics techniques to understand how the changes in stoichiometry are incorporated in the lattice. For the calculation of the impact of this non-stoichiometry on the thermal conductivity we will perform MD simulations using supercells seeded with the defects predicted from step 1.

5.2.1 Lattice statics simulations

Calculation of the defect energies were performed using the Mott-Littleton approach [133] and the GULP simulation package [153]. In the Mott-Littleton method the lattice is partitioned into three concentric regions (1, 2a and 2b) centred on the defect of interest. Within the central region, with a radius of 10 Å, ions are treated using the potential and are relaxed to achieve a force balance. The ions of region 2a are relaxed in one step using the Mott-Littleton approximation with the interactions between the regions treated explicitly. This region extended for 20 Å beyond region 1. The remainder of the crystal (region 2b) is simply represented as an array of point charges and is used to generate the Madelung field of the crystal.

5.2.2 Thermal conductivity simulations

MD simulations were performed using the LAMMPS simulation package [104]. Simulation supercells were constructed by taking L repetitions of the Li_2TiO_3 supercell along the direction of interest, and 10×10 unitcell cross-sections. These simulation supercells are initially energy minimised under constant pressure and subsequently equilibrated for 50 000 timesteps of 2 fs each, under NPT conditions using a Nosé-Hoover style thermostat and barostat with relaxation times of 0.05 ps and 1.0 ps, respectively.

Table 5.1: Table of simulation parameters for various axes, supercell lengths in units of unit cells, temperatures, repetitions, stoichiometries, simulation time, for a total of 360 simulations.

Axis	L	No. of Atoms	No. of Temperatures	No. of Repetitions	No. of Stoichiometries	Equil. time (timesteps)	NEMD time (timesteps)	Total time (timesteps)
x	30	144 360	5	3	2	100 000	200 000	300 000
	40	192 480	5	3	2	100 000	200 000	300 000
	50	240 600	5	3	2	100 000	200 000	300 000
	100	481 200	5	3	2	100 000	200 000	300 000
y	30	144 360	5	3	2	100 000	200 000	300 000
	40	192 480	5	3	2	100 000	500 000	600 000
	50	240 600	5	3	2	100 000	500 000	600 000
	100	481 200	5	3	2	100 000	500 000	600 000
z	30	144 360	5	3	2	100 000	500 000	600 000
	40	192 480	5	3	2	100 000	600 000	700 000
	50	240 600	5	3	2	100 000	1 000 000	1 100 000
	100	481 200	5	3	2	100 000	1 200 000	1 300 000

Once equilibrated, the thermal conductivity was determined using the Müller-Plathe method [127] as discussed in Chapter 3, with the same simulation parameters as described in Chapter 4. For details on all the simulations used in this chapter see table 5.1.

5.3 Results and discussion

To determine the exact mechanisms responsible for accommodating non-stoichiometry it is essential to know the energies for all of the intrinsic defect species. For Li_2TiO_3 these are presented in table 5.2. Defect energies calculated using the Mott-Littleton approach represent the energy to add or remove atoms and any accompanying charge from the system and placing them at an infinite separation, where they no longer interact with the system or each other. Consequently, they are not directly comparable with formation energies calculated using DFT where a reference state for both the atoms and electrons is typically defined. However, it is possible to draw comparisons between defects of the same type. For example, table 5.2 shows that the lithium site in the mixed cation layer (V_{Li3}^{1-}) exhibits the lowest defect energy of the lithium vacancy defects in excellent agreement with previous DFT simulations. However, there are some small discrepancies with the DFT. The defect energies presented in table 5.2 predict that the $\mathrm{V}_{\mathrm{Li2}}^{1+}$ defect is lower in energy than the $\mathrm{V}_{\mathrm{Li1}}^{1+}$ defect, however, as shown by Murphy and Hine [67], DFT predicts the opposite ordering. It is noted here that the difference in energy for these two vacancy defects presented here is 0.03 eV and for the DFT it is 0.04 eV, which is within the expected error of both techniques implying that the energy for the two defects are essentially the same.

Substitution of a titanium ion onto the lithium site in the mixed cation layer has a slightly larger defect energy than for substitution into the pure Li layer. This is likely due to the greater repulsion from the Ti^{4+} ions in the mixed cation layer and

Defect	Defect energy /eV	Defect	Defect energy /eV
V_{Li1}^{1-}	3.21	$\mathrm{Li}_{\mathrm{Ti1}}^{3-}$	27.59
V_{Li2}^{1-}	3.18	$\mathrm{Li}_{\mathrm{Ti2}}^{3-}$	27.59
V_{Li3}^{1-}	3.01	Li_{i1}^{1+}	-2.02
V_{Ti1}^{4-}	32.13	Li_{i2}^{1+}	-2.00
V_{Ti2}^{4-}	32.13	Ti_{i1}^{4+}	-22.23
V_{O1}^{2+}	9.22	Ti_{i2}^{4+}	-24.14
V_{O2}^{2+}	9.16	O_{i1}^{2-}	-0.99
V_{O3}^{2+}	9.43	O_{i2}^{2-}	-0.99
$\mathrm{Ti}_{\mathrm{Li1}}^{3+}$	-23.00		
$\mathrm{Ti}_{\mathrm{Li2}}^{3+}$	-22.90		
$\mathrm{Ti}_{\mathrm{Li3}}^{3+}$	-22.42		

Table 5.2: Table showing the defect energies for the intrinsic defects in Li_2TiO_3– as calculated using molecular simulations with the empirical potentials described in the text.

again concurs with existing DFT data [66]. For the oxygen vacancy defects, previous DFT simulations have shown that the removal of the oxygen from the O3 site is less energetically favourable than removal from either the O1 or O2 sites. Table 5.2 shows that the defect energy for the V_{O3}^{2+} defect is 9.43 eV which is higher than the values of 9.22 eV and 9.16 eV predicted for the V_{O1}^{2+} and V_{O2}^{2+} defect respectively, therefore it agrees with DFT. The empirical potential also predicts that there is very little distinction between the titanium sites, as the defect energies for the vacancy and antisite defects are the same on both available sites.

The crystal structure of Li_2TiO_3 means that the interstitial defects display complex geometries. For lithium the lowest energy interstitial defect has a split structure similar to those predicted in other materials [154]. Fig. 5.1 shows the lowest energy Li interstitial defect aligned along the z-direction centred on the Li3 site in

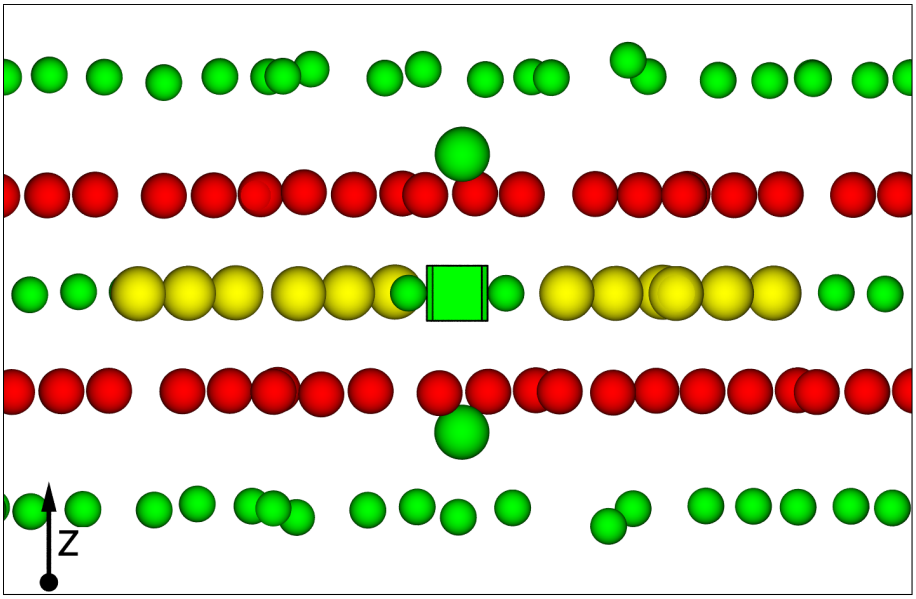

Figure 5.1: Graphical representation of the lowest energy Li_i^{1+} defect. Green, yellow and red spheres represent the lithium, titanium and oxygen ions respectively. The lithium interstitial displaces another lithium ion from the Li3 lattice site to create a Li^{1+}:V_{Li}^{1-}:Li^{1+} defect cluster aligned along the [001] direction, where the lithium vacancy is represented by the green cube, and the larger green spheres represent the Li interstitials.

the mixed cation layer. This interstitial configuration is only 0.02 eV lower than the simple isolated interstitial. A number of other split interstitial configurations were observed, aligned along different crystallographic directions, however, only the two lowest energies are reported in table 5.2 for conciseness. The titanium interstitial is predicted to be metastable and will displace a lithium ion resulting in the formation of a titanium antisite and lithium interstitial, i.e.:

$$Ti_i^{4+} + Li_{Li}^{\times} \rightarrow Ti_{Li}^{3+} + Li_i^{1+}. \tag{5.1}$$

The energy for this reaction is predicted to be -2.16 eV.

With the defect formation energies presented in table 5.2 it is possible to calculate the reaction energies for the intrinsic defect processes. The per defect reaction

Table 5.3: Table showing the reaction energies of rate intrinsic defect processes in Li_2TiO_3 normalised per defect (i.e. reaction energy/number of defects).

Process	Reaction energy (eV)
Li Frenkel	0.49
O Frenkel	4.03
Ti Frenkel	4.62
Antisite	2.29
Schottky	10.93

energies for the intrinsic defect processes are presented in table 5.3. The results show that the lithium Frenkel process is the lowest energy process and the antisite process is the next lowest energy process (see section 2.3.1 for descriptions of defect types). Therefore, the defect chemistry would be expected to be dominated by lithium interstitials/vacancies and antisite defects as predicted by DFT [67].

There are a range of different processes responsible for the accommodation of excess Li_2O and TiO_2 in Li_2TiO_3. In the majority of cases there is the defect that actually accommodates the excess cation and then other defects that compensate for the charge imbalance that arises, for example excess lithium might be accommodated via the Li_{Ti}^{3-} defect with charge compensation provided by the V_O^{2+} defect. Therefore, by considering all accommodating defects compensated for by all possible oppositely charged defects (while still ensuring the overall reaction changes the stoichiometry) it is possible to write a series of reactions that can accommodate non-stoichiometry in Li_2TiO_3. The list of processes considered in this chapter and the energy per formula unit incorporated into Li_2TiO_3 are presented in table 5.4. Note that in all cases the lowest energy for each defect has been used in the calculation of the reaction energies.

Table 5.4: Reaction energies for the incorporation of non-stoichiometry into Li_2TiO_3.

Excess	Number	Reaction	Reaction energy per Li_2O/TiO_2 (eV)
Li_2O	1	$Li_2O_{(s)} \rightarrow 2Li_i^{1+} + O_i^{2-}$	5.13
	2	$3Li_2O_{(s)} + Ti_{Ti}^0 \rightarrow 4Li_i^{1+} + V_{Ti}^{4-} + Li_2TiO_{3(s)}$	1.55
	3	$3Li_2O_{(s)} + Ti_{Ti}^0 \rightarrow 3Li_i^{1+} + Li_{Ti}^{3-} + Li_2TiO_{3(s)}$	0.72
	4	$3Li_2O_{(s)} + 2Ti_{Ti}^0 + 3O_O^0 \rightarrow 2Li_{Ti}^{3-} + 3V_O^{2+} + 2Li_2TiO_{3(s)}$	4.42
	5	$3Li_2O_{(s)} + 4Ti_{Ti}^0 \rightarrow 4Li_{Ti}^{3-} + 3Ti_i^{4+} + Li_2TiO_{3(s)}$	8.87
	6	$Li_2O_{(s)} + Ti_{Ti}^0 + 2O_O^0 \rightarrow V_{Ti}^{4-} + V_O^{2+} + Li_2TiO_{3(s)}$	10.63
TiO_2	7	$TiO_{2(s)} \rightarrow Ti_i^{4+} + 2O_i^{2-}$	16.14
	8	$3TiO_{2(s)} + 4Li_{Li}^0 \rightarrow Ti_i^{4+} + 4V_{Li}^{1-} + 2Li_2TiO_{3(s)}$	3.45
	9	$3TiO_{2(s)} + 2Li_{Li}^0 \rightarrow 2Ti_{Li}^{3+} + 3O_i^{2-} + Li_2TiO_{3(s)}$	6.63
	10	$3TiO_{2(s)} + 4Li_{Li}^0 \rightarrow Ti_{Li}^{3+} + 3V_{Li}^{1-} + 2Li_2TiO_{3(s)}$	1.67
	11	$TiO_{2(s)} + 2Li_{Li}^0 + O_O^0 \rightarrow 2V_{Li}^{1-} + V_O^{2+} + Li_2TiO_{3(s)}$	4.76

The results presented in table 5.4 show that the most thermodynamically favourable process for introducing excess Li_2O into Li_2TiO_3 is via a combination of the Li_i^{1+} and Li_{Ti}^{3+} defects. This prediction is in excellent agreement with previous DFT studies that predict that excess Li_2O incorporation by the same defects at intermediate oxygen partial pressures [67]. On the other side of the Li_2O-TiO_2 phase diagram the lowest energy process for incorporation of excess TiO_2 is via reaction 10 in the table. In reaction 10 excess TiO_2 is accommodated by the mutually charge compensating V_{Li}^{1-} and Ti_{Li}^{3+} defects, in agreement with previous studies [67, 150]. Overall, table 5.4 shows that the energy required to incorporate one formula unit of Li_2O is nearly 0.8 eV lower than for the incorporation of a TiO_2 unit. This observation matches the phase diagram presented in Fig. 2.13 by Kleykamp [60], which shows that Li_2TiO_3 can accommodate a greater degree of excess Li_2O than TiO_2. Overall the potential appears to very accurately reproduce the defect chemistry of Li_2TiO_3 from both experiment and DFT.

5.3.1 Thermal conductivity of non-stoichiometric Li_2TiO_3

Using the predictions above we can create simulation supercells for MD that contain representative degrees of non-stoichiometry. To explore both sides of the stoichiometry regime we look at 1% Li excess (Li-rich) and 1% Li loss (Li-poor) and use reaction numbers 3 and 10, respectively (see table 5.4).

For the Li-rich case, 0.5% of Ti sites were randomly selected and substituted with Li. Then, three times as many Li interstitials were added to make up to 1% Li excess while ensuring charge neutrality. For the Li-poor case, 0.25% of Li sites were randomly selected and substituted with Ti. Then, three times as many Li vacancies were created to balance the charge and make up to 1% Li loss. The defects were randomly introduced into the simulation supercells using Atomsk [105]. As the non-stoichiometry is accommodated by charged defects it is likely that these defects will form clusters, particularly, at low temperatures. An investigation of the role of

clustering of these defects and the impact on the predicted thermal conductivity is reserved for future work.

In Fig. 5.2 the extrapolated calculated thermal conductivity for both the Li-rich and Li-poor cases are shown. We see the same anisotropy in the thermal conductivity in the three spatial directions, as seen in Chapter 4. The thermal conductivity along z is notably lower than that in x and y.

Murphy *et al.* examined the elastic properties of Li_2TiO_3 and showed that the Young's modulus in z (205.7 GPa) is significantly reduced relative to x (238.2 GPa) and y (230.7 GPa) [66]. It should be noted that the orientation of the crystal in this previous work is not the same as used here and so comparisons of the thermal conductivities and stiffness's in x and y are not possible. The reduced stiffness predicted in the z direction will lead to lower phonon velocities reducing the thermal conductivity in this direction (see Eq. 2.13). This has the effect of reducing the average thermal conductivity (plotted as a dotted line) downwards.

Fig. 5.3 shows the average thermal conductivities of the Li-rich and Li-poor cases are compared to the perfect crystal seen in Chapter 4. From this figure we see that the introduction of defects reduces the thermal conductivity at low temperatures (< 500 K), although this reduction is modest. This is perhaps unsurprising as the antisite defects are not anticipated to have a significant impact on the thermal conductivity [35]. As the temperature increases the thermal conductivity for both non-stoichiometric samples becomes the same as that predicted for the stoichiometric material. Comparing both sides of the stoichiometry, the Li-rich side appears to have a slightly larger effect on the thermal conductivity ($\sim 9\%$ vs $\sim 7\%$ less than the perfect crystal) at 300 K.

In Fig. 5.5, the calculated thermal conductivities of Li-rich, Li-poor and the perfect crystal are displayed for individual x, y, and z-directions. Here we can see how the introduction of defects affected the thermal conductivity in each direction, which is particularly relevant for Li_2TiO_3 due to the high degree of anisotropy

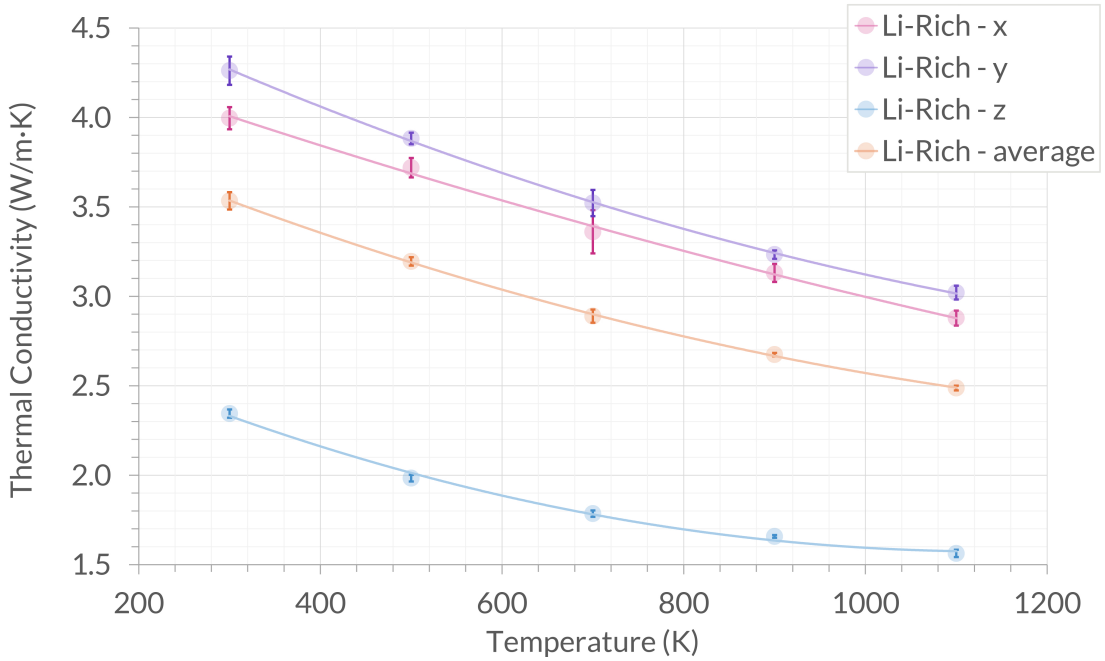

(5.2a) Li-rich

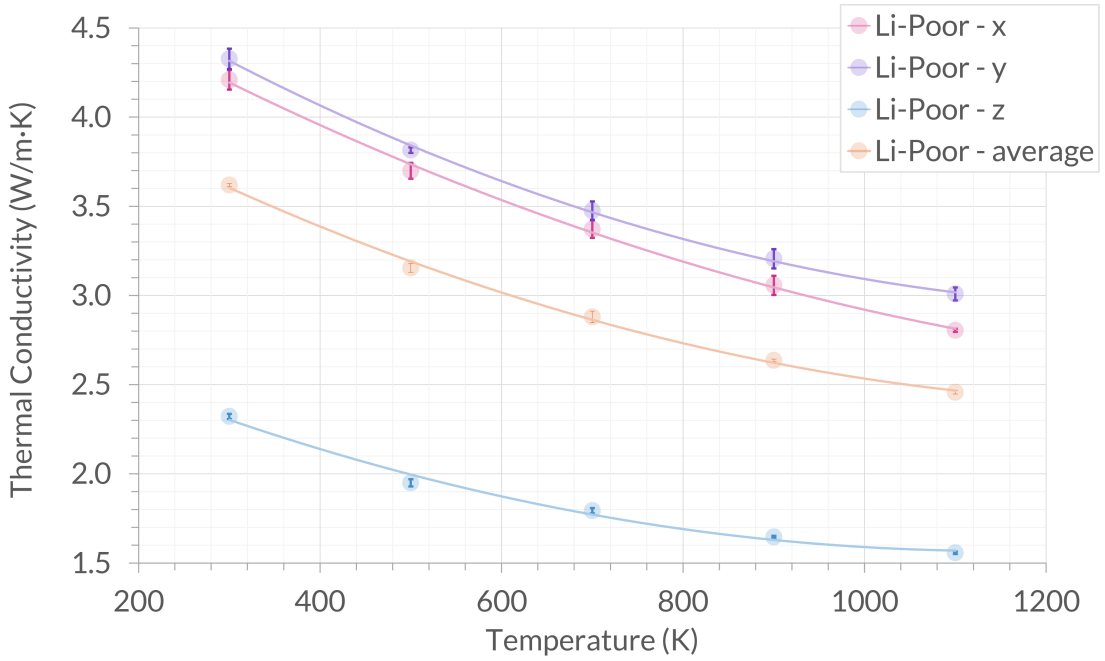

(5.2b) Li-poor

Figure 5.2: Calculated thermal conductivity of Li-rich and Li-poor as a function of temperature, in each of the spatial directions, and as an average over all directions. Where the Li-rich case has 1% more lithium and the Li-poor case has 1% less lithium than perfect Li_2TiO_3. Error bars show the standard deviation of three sets of randomly selected point defect locations.

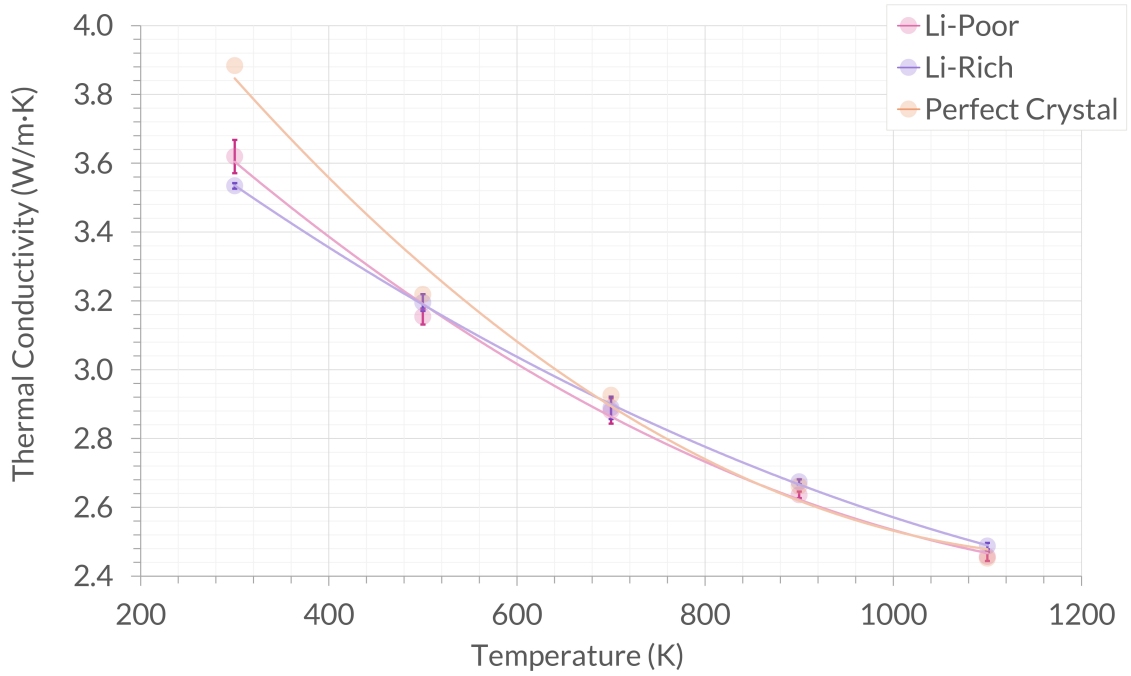

Figure 5.3: The average calculated thermal conductivity of Li-rich, Li-poor, and perfect Li_2TiO_3 as a function of temperature. Error bars show the standard deviation of three sets of randomly selected point defect locations.

predicted previously.

Some experimental data concerning non-stoichiometric Li_2TiO_3 is available in the literature. Roux [152] and Hoshino *et al.* [138] measured thermal properties of $0.95Li_2TiO_3$ (where the molecular ratio of Li_2O over TiO_2 is 0.95, i.e. lithium deficient). This is seen compared to this work in Fig. 5.4. We see the same trend in the data of decreasing thermal conductivity with increasing temperature. This experimental data is not directly comparable to this work due to the presence of many other defects not included in our simulations. Both Roux and Hoshino *et al.* made the interesting observation of finding the thermal conductivity of lithium deficient Li_2TiO_3 to be higher than the stoichiometric thermal conductivity. As discussed in the introduction the origin of this may be increased grain sizes observed in the non-stoichiometric material, resulting in reduced phonon scattering at grain boundaries [149].

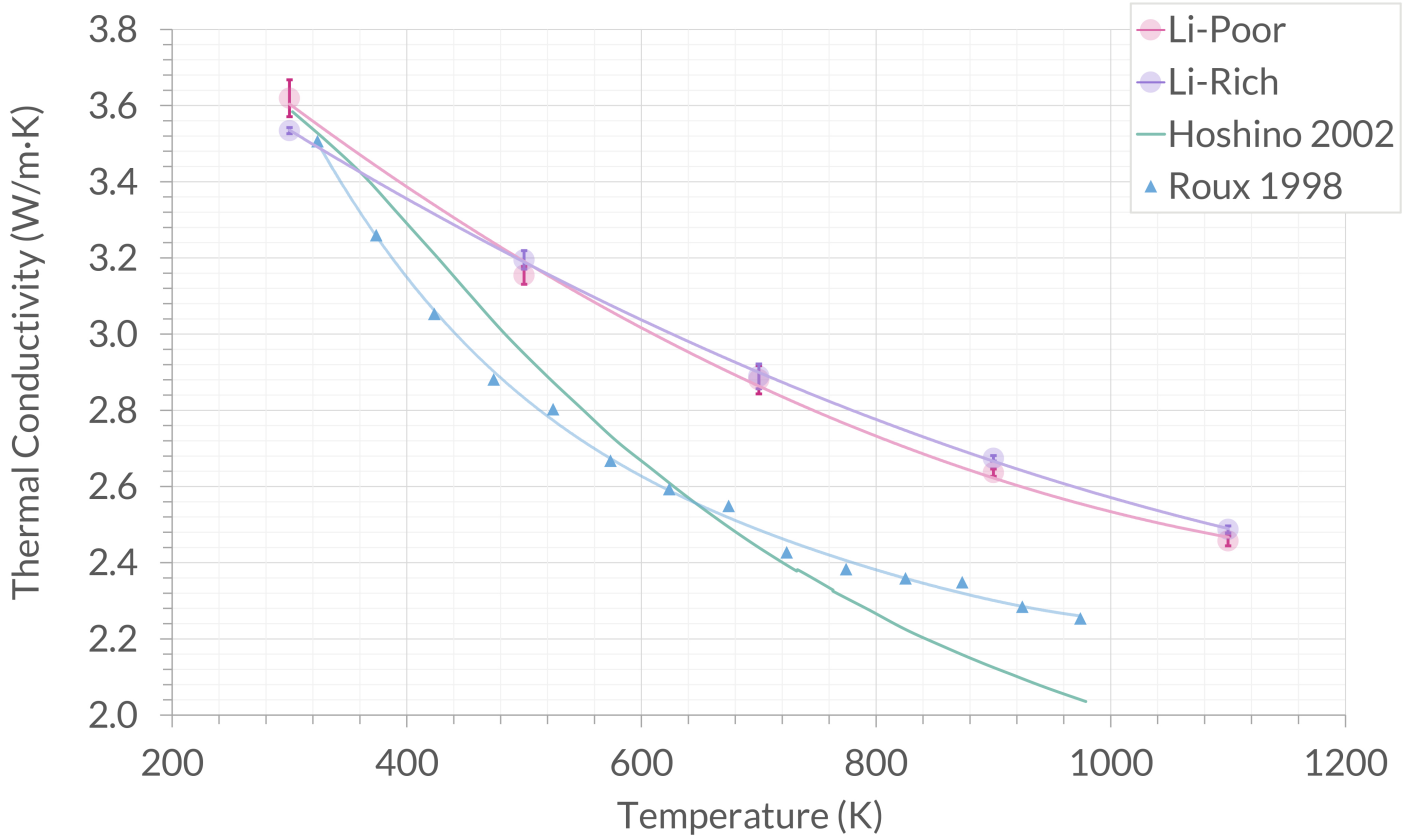

Figure 5.4: The average calculated thermal conductivity of Li-rich and Li-poor, plotted alongside experimental results from the literature [138, 152]. Error bars show the standard deviation of three sets of randomly selected point defect locations.

Fig. 5.5 shows that the reduction in thermal conductivity observed at low temperatures is predominantly in the x and y-directions irrespective of whether the sample is Li-rich or Li-poor. By contrast the thermal conductivity in the z-direction shows very little difference between the three cases.

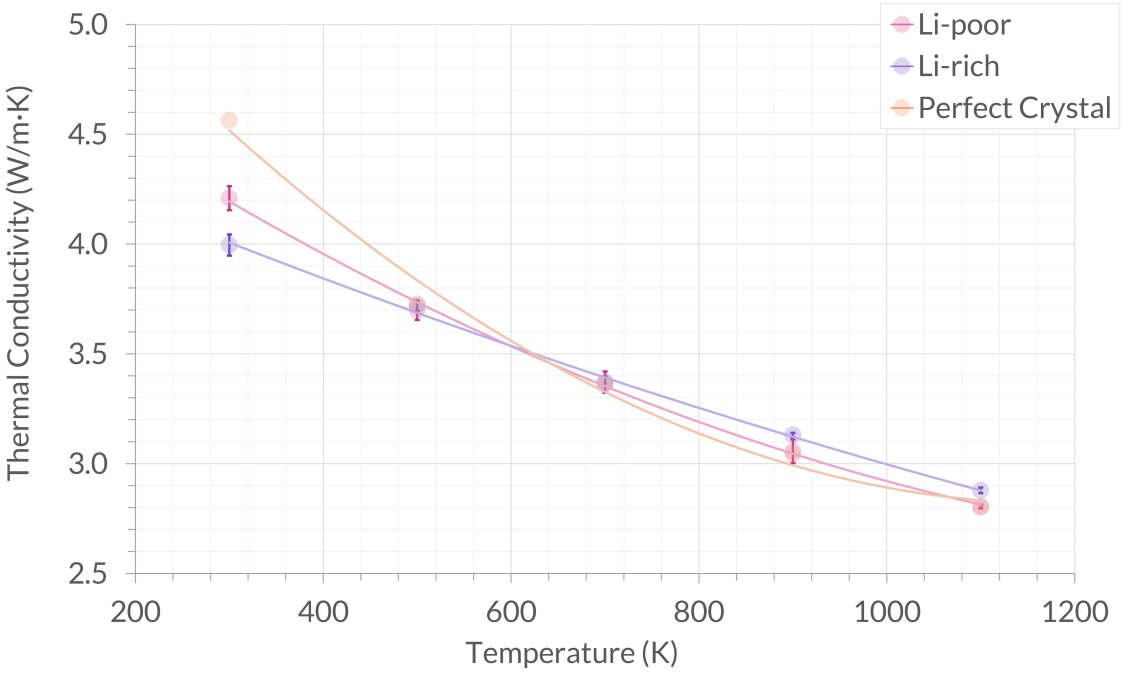

(5.5a) x

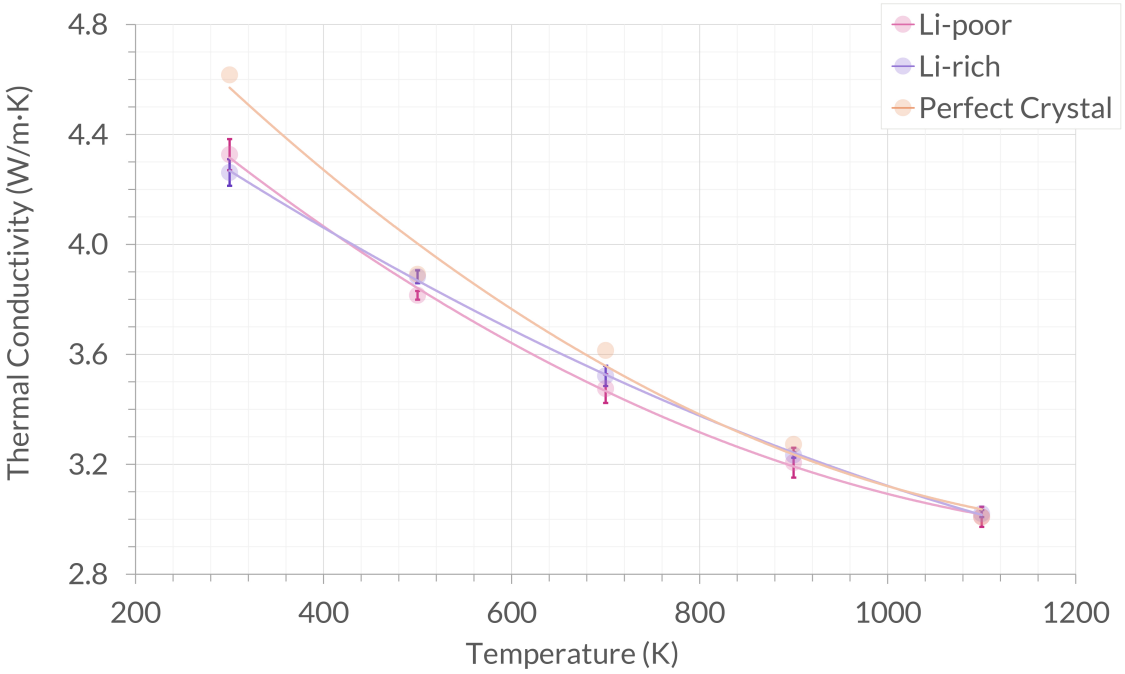

(5.5b) y

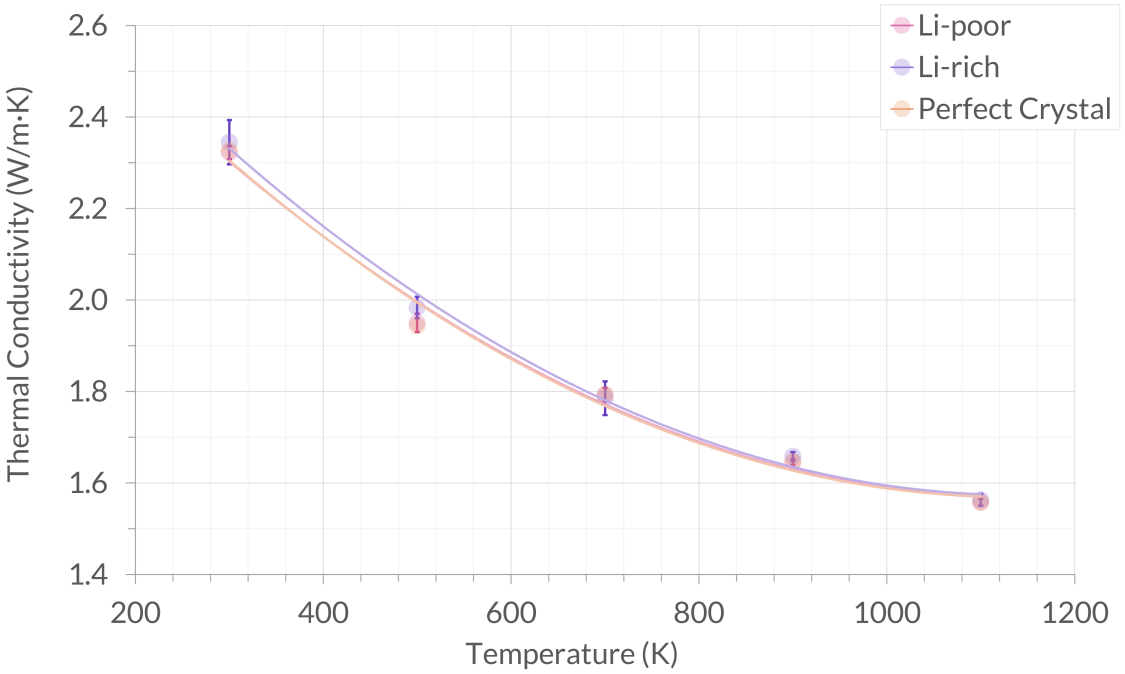

(5.5c) z

Figure 5.5: Calculated thermal conductivity of Li-rich, Li-poor, and perfect Li_2TiO_3 as a function of temperature, in each of the spatial directions x, y, and z. Error bars show the standard deviation of three sets of randomly selected point defect locations.

5.4 Summary

From defect energies calculated using the Mott-Littleton approach the reaction energies for different mechanisms for incorporation of non-stoichiometry have been determined. The results predict that in the Li_2O-rich regime accommodation is via the mutually charge compensating Li_i^{1+} and Li_{Ti}^{3-} defects, while in the TiO_2 rich regime accommodation is via the V_{Li}^{1-} defect with charge compensation provided by the Ti_{Li}^{3+} defect. The energy for incorporation of a formula unit of Li_2O was found to be significantly lower than for TiO_2, in agreement with the phase diagram that shows considerably more non-stoichiometry on the Li_2O-rich side.

Starting from lowest energy configurations, non-stoichiometry was accommodated in NEMD simulations to calculate the thermal conductivity. It was found that the thermal conductivity decreases on both sides of the stoichiometry (1% Li excess and 1% Li loss) at temperatures $< 500\,\mathrm{K}$. However, at higher temperatures changes in the stoichiometry of the crystal have a negligible impact on the thermal conductivity. The Li-rich case appears to have a slightly greater effect than the Li-poor case. The previously seen anisotropy of the thermal conductivity of Li_2TiO_3 is seen again, with the non-stoichiometry making no impact on the thermal conductivity in the z-direction, and only affecting the thermal conductivity in x and y. Overall, the results show that the thermal conductivity drops with the introduction of defects accommodating non-stoichiometry for both sides of the stoichiometry.

Given that the breeder blanket region of a future fusion reactor will be operating at higher temperatures, the results presented here suggest that there will be little or no impact from Li burn-up on the thermal conductivity of the breeder material and consequently, no impact on thermal efficiency of the reactor. Further, the changes in stoichiometry were accommodated through the introduction of large numbers of point defects, similar to those introduced by neutron irradiation. As a consequence we speculate that the these defects are also unlikely to significantly impact the

thermal conductivity. However, neutron irradiation can also create much larger defects such as dislocation loops and voids; the impact that those might have on thermal conductivity is assessed in the coming chapters.

6

Introduction of voids

6.1 Introduction

We then examined defects of a larger scale known as voids. Voids are regions within a substance that lack any particles, essentially being empty space. They can occur as a result of the material's fabrication process, whether as intended features or unintended defects. For instance, voids can often be found in powders and sintered materials due to the nature of these fabrication methods. In addition to this, cracks that form in a material over time due to stress or other factors can introduce voids into a material even after its fabrication.

It is essential to clarify the distinction between voids and pores to define what is meant by porosity. While both refer to empty spaces, voids are simply unoccupied regions within a material. A void can act as a pore if it is accessible to a particular substance from outside it, allowing the substance to enter, exit, or permeate the void. Porosity is defined as the volume fraction of these accessible spaces (pores) within the material. However, porosity is only meaningful in relation to a specific substance. For example, a material could be porous to tritium, allowing tritium to diffuse through a network of connected pores, but be non-porous to oxygen, if the oxygen cannot penetrate or escape these spaces.

Pores can vary in size, ranging from microscopic to macroscopic dimensions. Pores can be categorised by their size using the IUPAC definitions into the following: micropores (<2 nm), mesopores (2–50 nm), and macropores (>50 nm) [155]. Small molecules such as tritium can permeate through micropores, while larger molecules might only be able to pass through mesopores or macropores. However, size alone is not always the determining factor; the crystal structure, pore connectivity, and surface interactions also play crucial roles. Furthermore, a material with interconnected pores may allow diffusion of molecules through the structure, while isolated pores might trap molecules, preventing them from escaping.

In specific situations, an increased level of porosity may be advantageous, particularly when aiming to create lightweight materials. However, it is important to note that a higher porosity can also compromise a material's strength and diminish its structural integrity. The introduction of porosity into the breeder material is expected to enhance tritium release, however, this will have implications on other aspects of the breeder's physical properties. Therefore, it is important to understand the effect of voids on heat transfer through the material.

6.2 Methodology

6.2.1 Thermal Conductivity

We begin our investigation of voids and porosity by examining the impact of the introduction of a single void into a simulation supercell. This is done by creating a perfect supercell of cross-section 10×10 and half the desired final length, i.e. $L = 30$ unit cells. A void of radius r was then introduced at the centre of the simulation supercell by removing the atoms within a given radius of this point. A select few neighbouring atoms are also removed to balance the charge of the void so that the supercell remains charge-neutral. This is important for isolating the effect of the presence of voids from the effect of net charge. This supercell is then doubled along

the direction of calculation to a final length of $L = 60$ unit cells, meaning that the final simulation supercell contains two identical voids (see Fig. 6.1). This also easily maintains the requirements for periodic boundary conditions in the simulation supercell.

This void arrangement is important for the application of the Müller-Plathe method, where the hottest chunk of the supercell is at the centre. Placing a single void in the centre of the supercell would not well represent a temperature gradient across a void, and instead places the majority of the void in the hot centre of the supercell. This large discrepancy in the number of particles in the centre chunk would also lead to the material being more easily melted in these simulation parameters, which is not the aim of this study.

Supercells were created containing voids of radius 10, 15, and 20 Å, making supercells with $p = 0.36\%$, 1.21%, and 2.83%, where, p refers to the percentage of atoms removed from the perfect supercell.

By using an atomistic visualisation tool, the Open Visualization Tool (OVITO), we estimate the porosity of the supercell with respect to tritium. OVITO calculates the porosity by generating a surface mesh that outlines the voids within a material. It identifies which particles are in close proximity and creates geometric elements connecting them to form a mesh. This side of these elements depends on the probe sphere radius. For this, we use 2.5 Å, to approximate the accessible space for molecules like tritium (the kinetic diameter of a tritium molecule is 2.89 Å [156]). The probe sphere checks whether a region is accessible by testing whether it fits within the gaps between particles. The accessible surface area is then used to estimate the volume fraction of voids, from which porosity is calculated. Due to the small size of tritium molecules, we found that we can approximate the porosity of the supercell to be equal to the percentage of atoms removed in the spherical void.

It should be noted that in previous work 20 chunks were used to implement the Müller-Plathe method. However, this was quickly found to be insufficient for

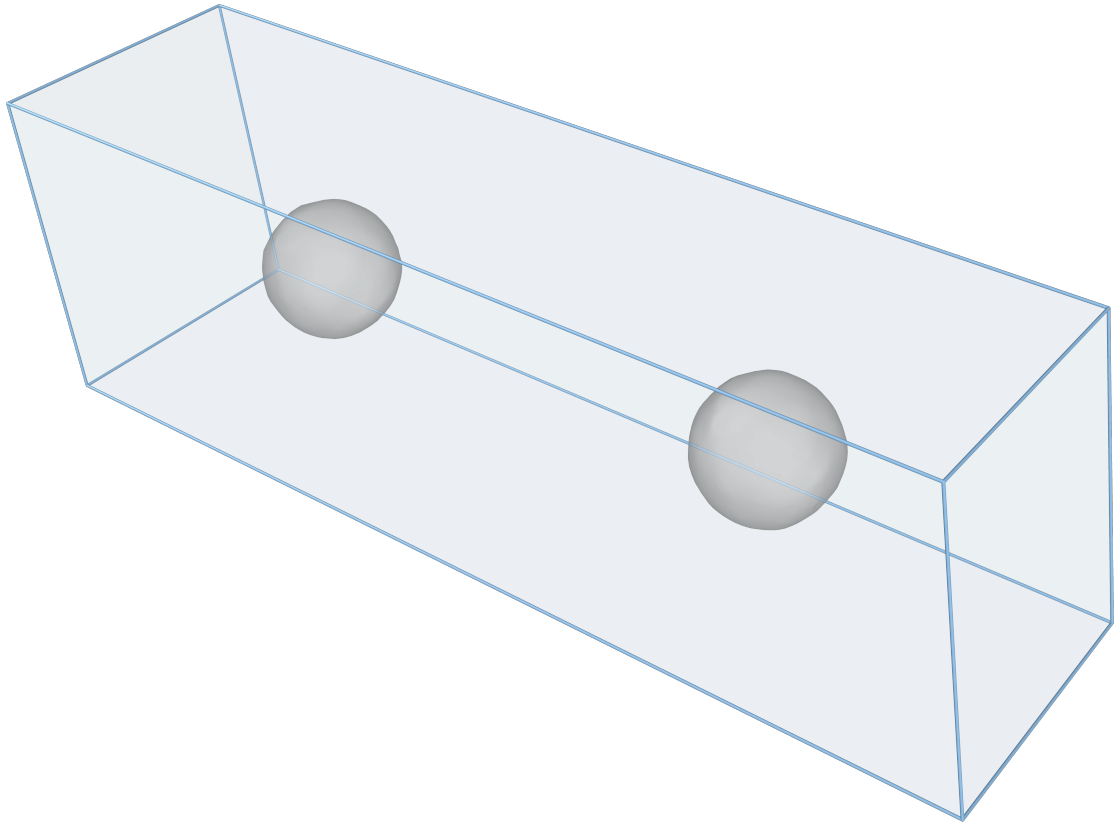

Figure 6.1: 60×10×10 unit cells supercell containing single voids in each half of radius $r = 20$ Å, visualised in OVITO.

the study of single voids. This is due to the large discrepancy in the number of particles in the chunks containing the void and those without. In the worst case, the smallest voids were entirely captured inside a single chunk. This prevents a steady state temperature gradient from developing, hence resulting in a poorly defined temperature gradients across the void. Instead, we used 80 chunks to well sample the crystal region that includes the void (see Fig. 6.2) while still ensuring that each chunk contains sufficient particles. To represent the porosity of the entire supercell, we take the average temperature gradient across each half of the supercell. The value obtained for each half was then averaged again to obtain the final value used for all calculations in this chapter.

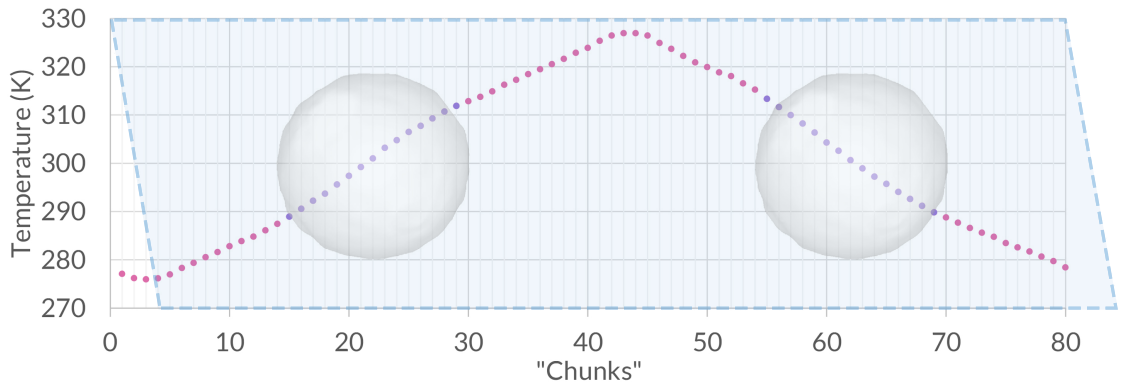

Figure 6.2: Example figure showing the average induced temperature profile in the simulation supercell (60×10×10 unit cells) for thermal conductivity calculations along x at temperature $T = 300$ K, containing single voids in each half of radius $r = 30$ Å. The data points from the bulk crystal are shown in pink, and the data points in the sections including the single voids are shown in purple.

By examining the induced temperature profile across the supercell in Fig. 6.3, we can identify two distinct temperature gradients: that of the bulk crystal and that of the section containing the void. We can see that the gradient is steeper when across the section including the void, which would correspond to a reduction in the thermal conductivity. To represent the density of the whole supercell, we take the average temperature gradient across the entire half of the supercell.

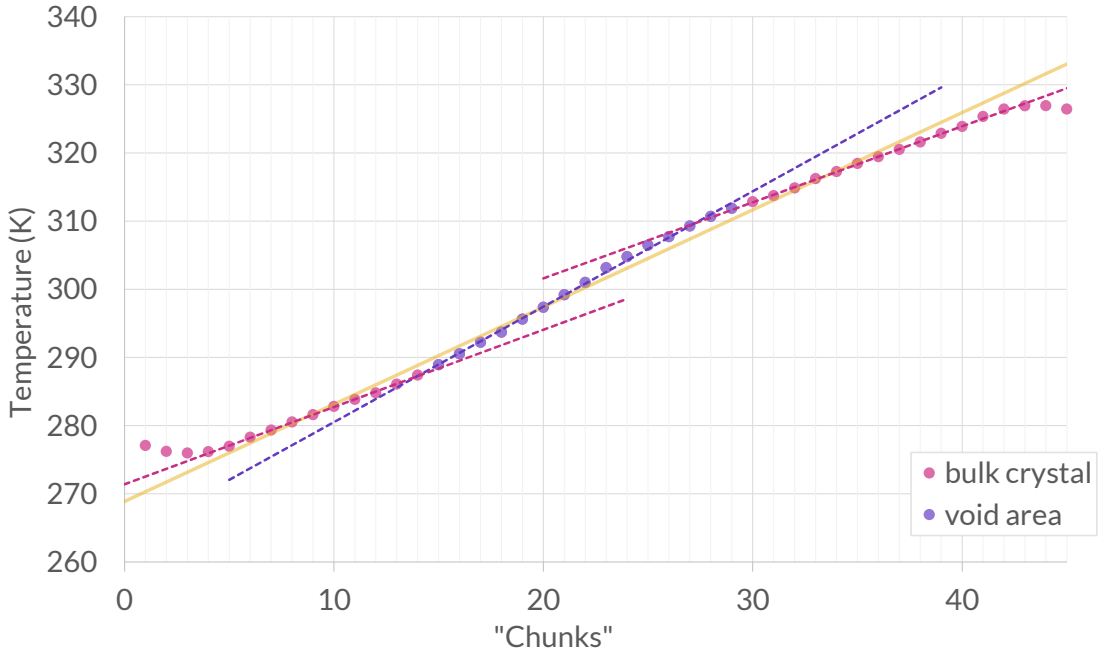

Figure 6.3: Figure showing the average temperature gradient (yellow), taken across the entire half supercell as compared to the temperature gradient in the bulk crystal (pink) and across the void section (purple). The same is seen on the right-hand side of the profile. Compare with Fig. 6.2.

The Müller-Plathe method of thermal conductivity calculation is applied with the equilibration steps as seen in previous chapters. It was confirmed that steady state temperature gradients had been reached by the end of the allowed equilibration time and results are taken over an average of the simulation steps after equilibration. The results shown are from the final set of simulations listed in table 6.1.

Axis	L	Void Radius (Å)	No. of Atoms	No. of Temperatures	Equil. time (timesteps)	NEMD time (timesteps)	Total time (timesteps)
x	60	0	288 000	5	100 000	500 000	600 000
		10	287 040	5	100 000	500 000	600 000
		15	284 742	5	100 000	500 000	600 000
		20	280 296	5	100 000	500 000	600 000
y	60	0	288 000	5	100 000	500 000	600 000
		10	287 040	5	100 000	500 000	600 000
		15	284 742	5	100 000	500 000	600 000
		20	280 296	5	100 000	500 000	600 000
z	60	0	288 000	5	100 000	1 000 000	1 100 000
		10	287 040	5	100 000	1 000 000	1 100 000
		15	284 742	5	100 000	1 000 000	1 100 000
		20	280 296	5	100 000	1 000 000	1 100 000

Table 6.1: List of simulation parameters for various axes, supercell lengths in units of unit cells, void radii, temperatures, simulation time, used for studying the effect of single voids on the thermal conductivity in Li_2TiO_3, for a total of 60 simulations.

6.3 Results and discussion

6.3.1 Thermal conductivity

Fig. 6.4 shows the calculated thermal conductivity in the three spatial directions as a function of temperature for a series of void radii. For all directions we see a decrease in the calculated thermal conductivity with increasing temperature which is as expected with the introduction of voids. For all directions and temperatures, we also observe a reduction in the thermal conductivity with increasing void size.

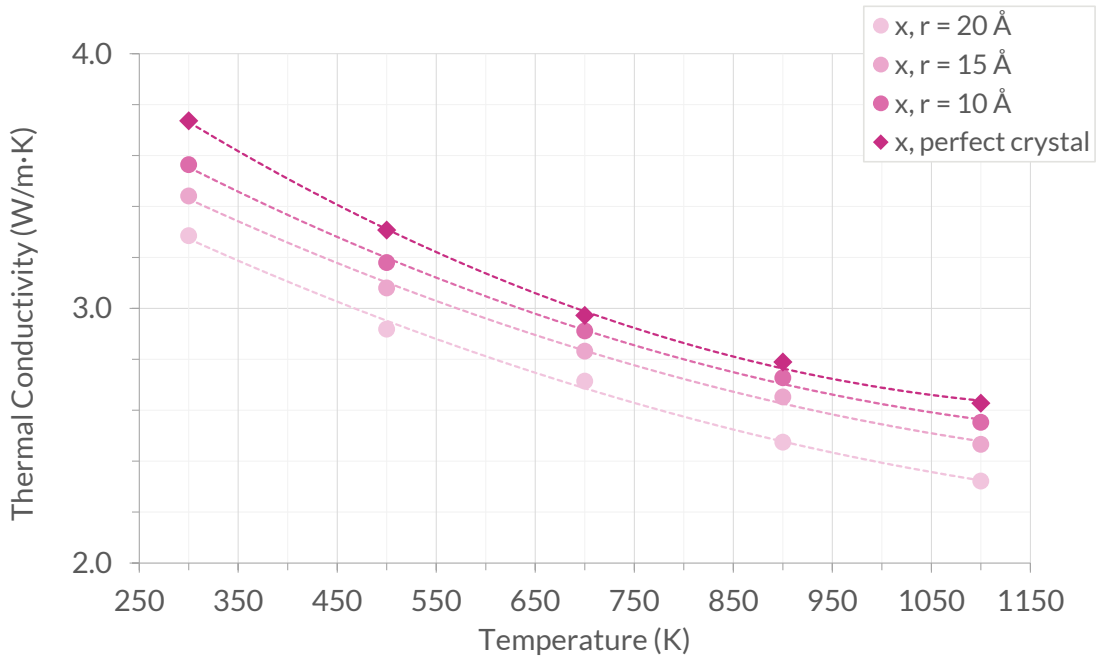

(6.4a) x

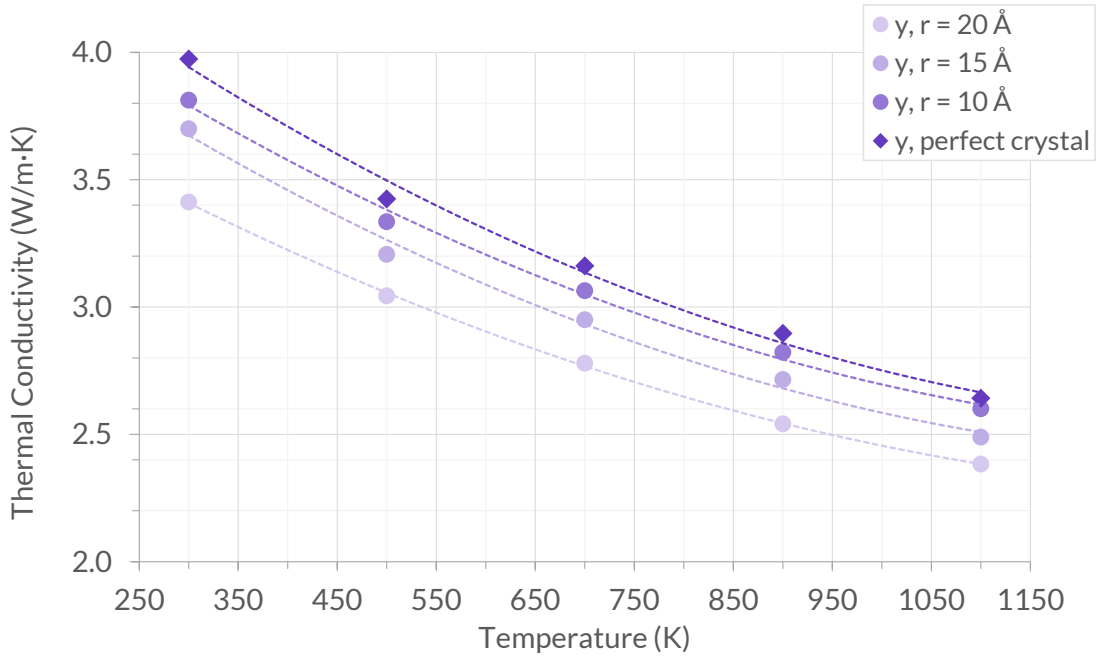

(6.4b) y

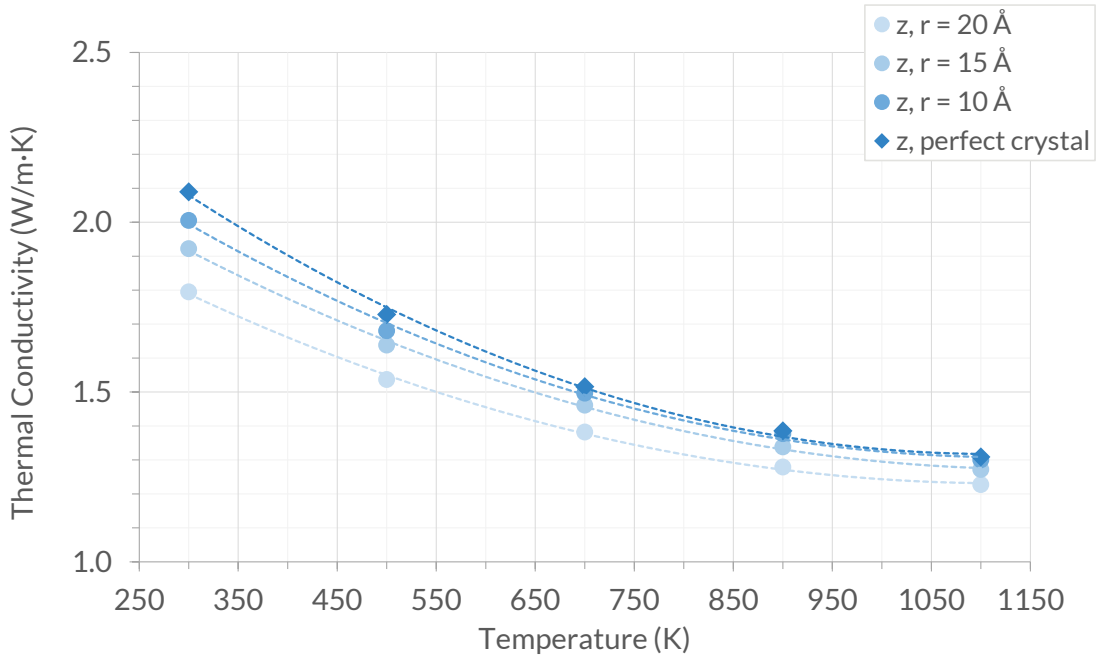

(6.4c) z

Figure 6.4: Calculated thermal conductivity for single voids of radius r = 10 Å, 15 Å, and 20 Å, in each of the spatial directions x, y, and z.

In the y and z cases we observe a greater reduction in the thermal conductivity at lower temperatures (300–500 K) than seen at higher temperatures. In the x-direction this trend is not observed and the reduction in thermal conductivity is relatively constant with increasing temperature. A possible explanation for this is when examining the thermal conductivity along x, the perpendicular cross-section is made from 10x10 images of the supercell in y and z, resulting in the largest cross-sectional area ($\sim$ 70% larger), such that the void cross-section is proportionally lower in the x-direction than in other directions (Fig. 4.2). When temperature is increased there is also some increase in the cross-sectional area (and volume) of the supercell. This increase with temperature is proportionally less along x than y or z due to its already larger cross-section. In Chapter 4, the effect of supercell cross-section was tested and a 10×10 unit-cells cross-section was determined to be suitable for our purposes. Since periodic boundary condition are maintained, this effect can be attributed to the difference in crystal structure along the different directions.

The average thermal conductivity for isolated voids is presented in Fig. 6.5 where it is compared to the experimental data of Shrivastava *et al.* [157] and Saito *et al.* [137]. Note that the average is simply the trace of the matrix for the thermal conductivity. In all cases there is a slightly greater decrease in the thermal conductivity at lower temperatures than at the higher temperatures, as we could have seen from the individual conductivities in y and z. These average thermal conductivities can be directly compared to experimental data where samples can be expected to have randomly orientated grains.

For the $r = 10$ Å void we see a decrease in the calculated thermal conductivity of $\sim$3% to $\sim$1% as temperature increases. For the $r = 15$ Å case this decrease goes from $\sim$6% to $\sim$4%, and for the $r = 20$ Å case, $\sim$11% to $\sim$8%.

As shown in Fig. 6.5 the lowest porosity sample of 4%, seen in the literature, is significantly higher than the highest porosity achievable with a single void in the supercell size of this work (2.83%). This is due to the void size being limited

by the supercell size. Larger supercells greatly increase the computational cost of the simulation. Previous experimental investigations observed that the thermal conductivity is reduced at all temperatures for increased porosity, as seen in this work. In the data presented from Shrivastava *et al.* we see an increase in the thermal conductivity after the initial decrease at lower temperature. This trend is not observed in this work, but has also been observed in studies of Li_2TiO_3 pebbles by Davis and Haasz [136] and Saito *et al.* [137].

We previously postulated that the small increase in thermal conductivity at high temperature seen in these works was due to an increase in the photon contribution of the thermal conductivity, which would not be captured by MD. However, seeing a much larger increase in the thermal conductivity at high temperature in Shrivastava *et al.* [157] suggests that the increase may be due to sintering of the crystal at higher temperatures, reducing the actual porosity of the samples from their initial porosity. The reported porosity of the samples is only provided before the experiments and is not re-examined at the end. This phenomenon would not be seen in this work on these timescales.

In Fig. 6.6 we see the average calculated thermal conductivity as a function of porosity. We can clearly see that for all temperatures thermal conductivity decreases with increasing porosity. This is as expected with the inclusion of voids as the heat has no media for conduction through the voids thus inhibiting heat transfer.

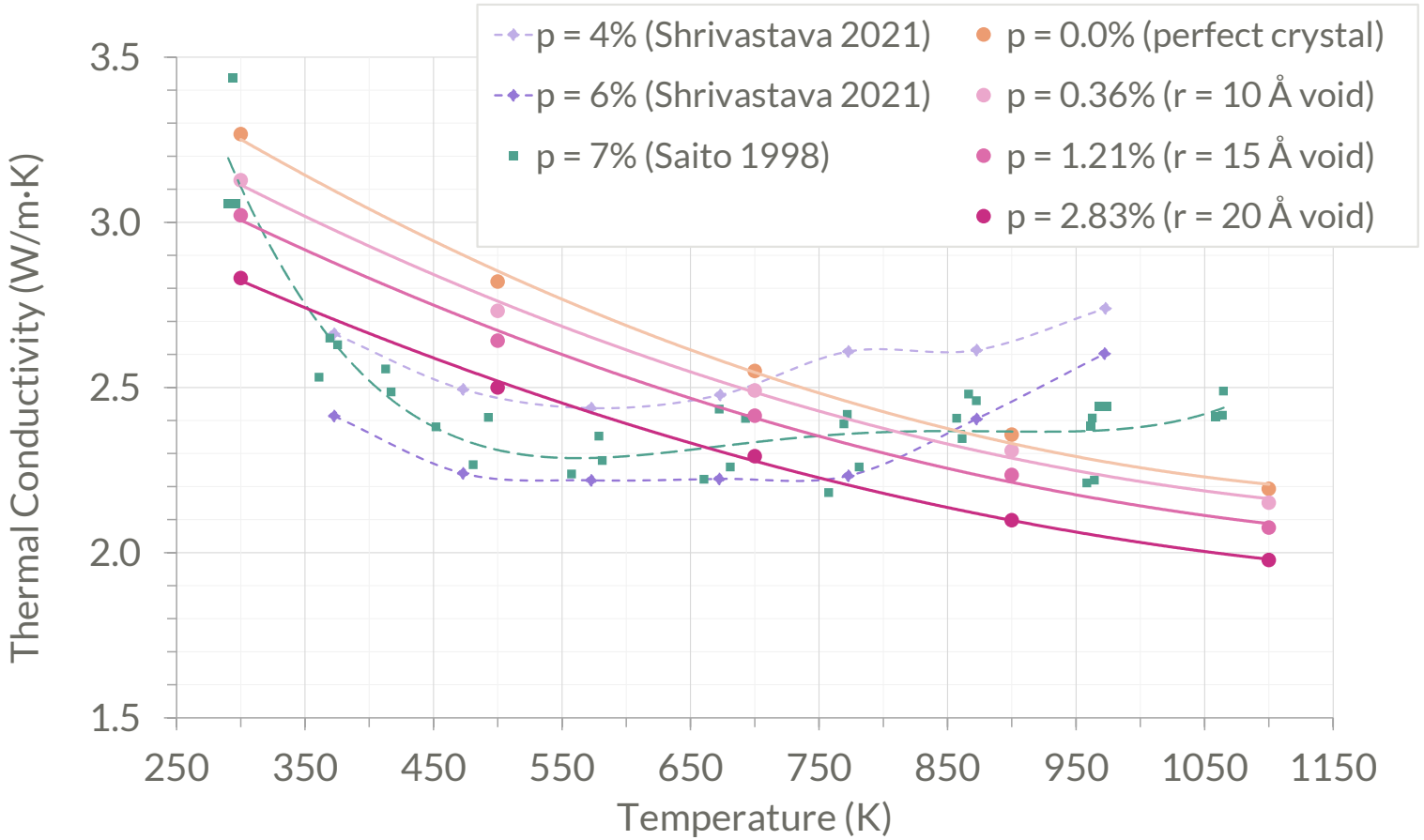

Figure 6.5: Calculated thermal conductivity of increased single void size and perfect Li_2TiO_3 as a function of temperature. For simulation cells sizes of 10×10 cross-section and $L = 60$ unit cells in direction of calculation. Compared with experimental data from Shrivastava *et al.* [157] and Saito *et al.* [137]

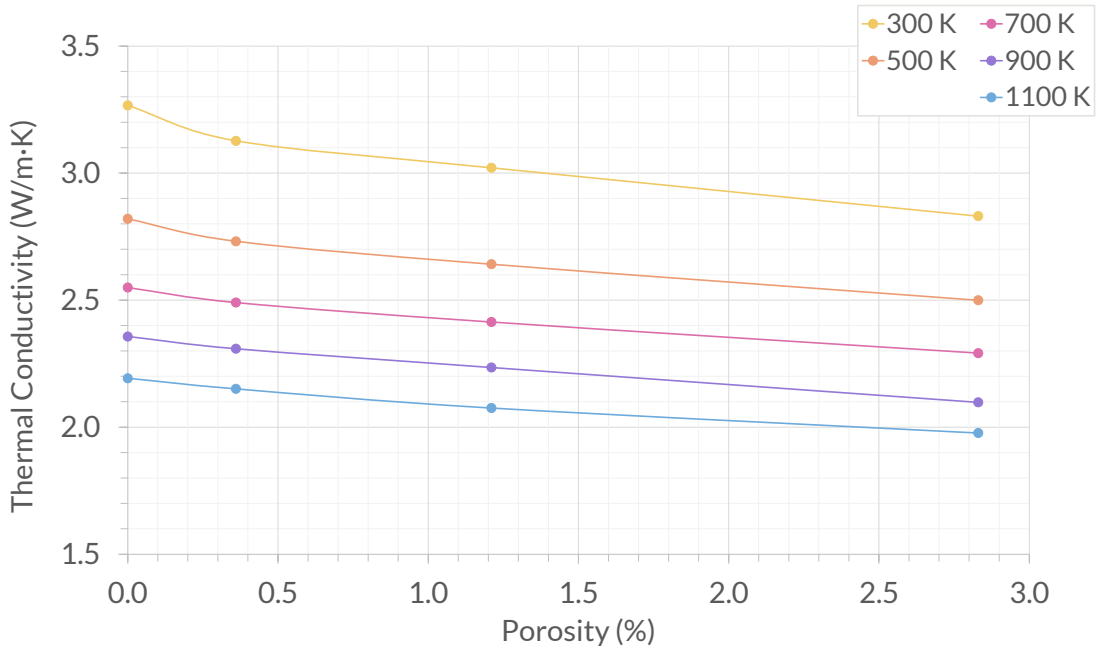

Figure 6.6: The average calculated thermal conductivity with respect to porosity for each studied temperature for supercells containing single voids.

6.4 Summary

The effect of single voids on the thermal conductivity and crystal structure of Li_2TiO_3 was investigated to find that increased void size reduces the thermal conductivity at all temperatures and in all directions. We do not observe the trend of increased thermal conductivity at high temperature after an initial decline seen in the literature. We offer the explanation that the samples in the literature may have experienced sintering, reducing their actual porosity with increased temperature. This effect would not be seen in the simulations of this work with such short timescales.

To study higher porosities as seen in experiment it is essential to simulate many smaller voids in the supercell, which follows in the next chapter.

7

Effect of porosity

This work has previously been published in Fusion Engineering and Design [158].

7.1 Introduction

Building on the work of single void effects, we can now study the effect of porosity on heat transfer in Li_2TiO_3. Relatively high levels of porosity (circa 10%) are attractive to enable the release of tritium from ceramic breeder materials, however, it may also have a detrimental impact on the thermal and mechanical properties of the material. The porosity of the breeder material is dependent on the process and conditions used in the fabrication of the pebbles. The fabrication process can be divided into two main steps; Li_2TiO_3 powder synthesis, and subsequent pebble fabrication from this powder using granulation techniques. More detail on Li_2TiO_3 fabrication processes are found in Chapter 2.

The thermal conductivity of Li_2TiO_3 has been widely studied previously. There is significant variation in not just the value of the thermal conductivity but the trend as a function of temperature. Hoshino *et al.* [138] and Reimann and Hermsmeyer [141] predicted that the thermal conductivity of stoichiomteric Li_2TiO_3 decreases as a function of temperature. However, works by Saito *et al.* [137] and Davis and

Haasz [136] suggest that, while there is an initial decrease in the thermal conductivity, it starts to increase again from around 600 K. The significant scatter in this data is due to the range of different densities and grain sizes in the different samples. In Chapter 5, MD simulations suggest that deviations in stoichiometry have a small impact on thermal conductivity at 300 K and a negligible effect at operational temperatures (typically 900-1050 K [57]), however, experimental studies suggest that non-stoichiometric samples exhibit higher thermal conductivities [152]. Mukai *et al.* [149] argue that this is due to a larger grain size present for the non-stoichiometric samples. Saito *et al.* [137] and Shrivastava *et al.* [157] have investigated the impact of porosity on the thermal conductivity of Li_2TiO_3.

In both studies it is shown that the thermal conductivity of the samples is decreased by the introduction of increased porosity. Interestingly, both groups observe an increase in the thermal conductivity with temperature in their samples [137, 157]. So marked is this increase that Shrivastava *et al.* [157] find the thermal conductivity for Li_2TiO_3 with a porosity of 4% is greater at 1000 K than 300 K. Typically, it would be anticipated that the thermal conductivity of a ceramic will decrease with temperature due to increased vibrations and increased levels of phonon scattering. Therefore, the observed increase may be due to changes in the material's microstructure, possibly sintering. It is noted that the porosity of the materials is not measured both before and after experiments examining the thermal diffusivity, therefore, any changes in porosity during heating may have been missed.

As discussed above, some initial porosity is expected to be present in Li_2TiO_3 pebbles to aid tritium release. This is likely to change during the lifetime of the blanket as more defects are introduced due to the irradiation and lithium burn-up.

7.2 Methodology

7.2.1 Introducing porosity

To simulate realistic porosities, we create simulation supercells that include many randomly distributed spherical voids of a range of sizes, built up to a given porosity. This was done by randomly selecting the position for a void, as well as randomly selecting its radius from a given range (chosen to be r = 5–10 Å). The atoms that fell within this given radius are then removed, and then a select few more atoms near the surface of this sphere are also removed as needed to maintain the charge balance. This process is repeated until the necessary proportion of atoms are removed. Due to the iterative process, voids are allowed to overlap without causing any miscounting in the number of atoms. An example supercell containing many voids can be seen in Fig. 7.1. The porosities were chosen to mirror results from Shrivastava *et al.* [157], choosing to simulate the lowest porosities of p = 4.0%, 6.0%, and 11.0%.

7.2.2 Thermal diffusivity and specific heat capacity

Using the calculated values for the thermal conductivity we are also able to deduce the thermal diffusivity, which defines the rate of heat transfer through the material. We can then determine the thermal diffusivity from the following relation seen in Eq. 2.7. The inclusion of density in the definition of α excludes the porosity as a variable, making it more easily comparable to other results, especially experimentally obtained values from the literature.

The specific heat capacity of Li_2TiO_3 at constant pressure was calculated using MD simulations of a 10×10×10 supercell consisting of 48,000 atoms (in a perfect crystal configuration). The supercell was energy-minimised and then equilibrated in NPT conditions for 600,000 timesteps of 2 fs for temperatures, T = 200-1200 K in increments of 50 K (see table 7.1 for details on all the simulations used in this

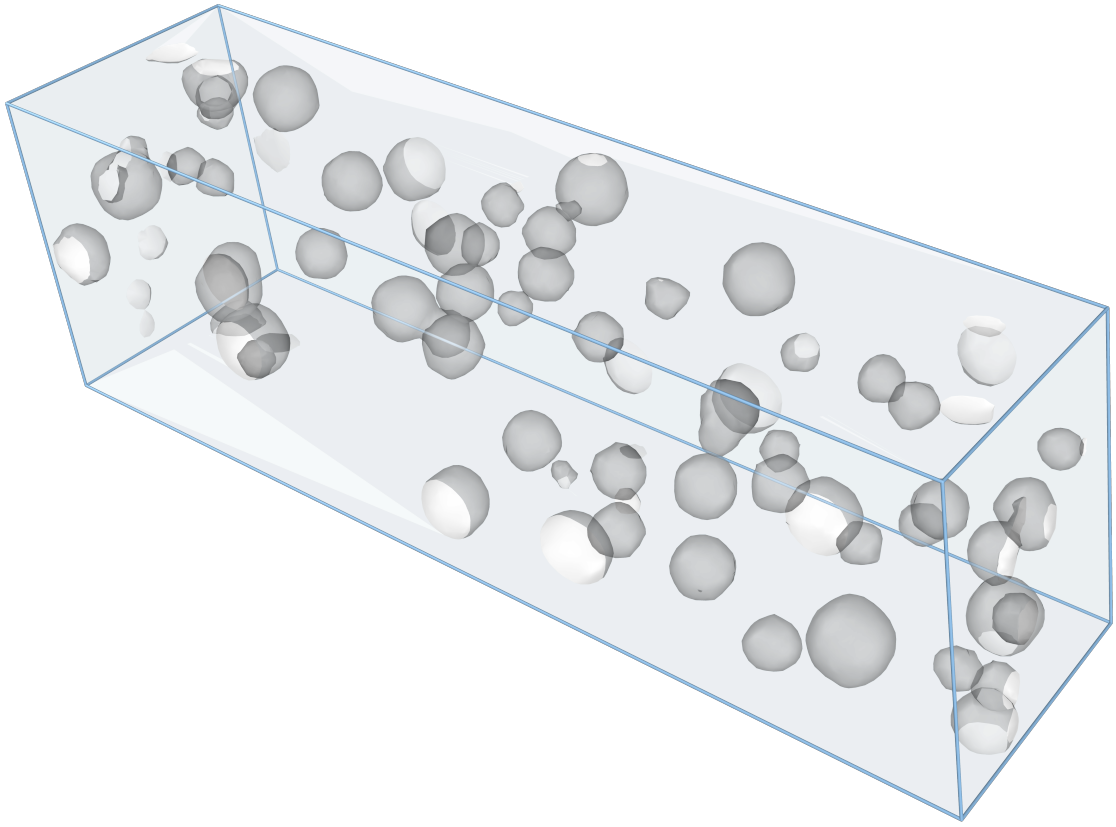

Figure 7.1: 60×10×10 supercell containing many voids up to a porosity of $p = 4.00\%$, of radii $r = 5$–$10\,\text{Å}$, visualised in OVITO.

chapter). These simulations employed the Nosé-Hoover thermostat and barostat with relaxation times of 0.1 ps and 0.5 ps respectively. The enthalpy and density were then calculated by averaging over the values obtained every 100 timesteps from the last 20,000 timesteps after ensuring that the enthalpy value had converged by this time (the standard deviation of the average enthalpy at each temperature was $\sim$0.01%). Then, by calculating the gradient of the enthalpy increment with increasing temperature at every 50 K (by fitting to points $\pm$100 K), we find the isobaric heat capacity C_p from the following equation:

$$C_p = \frac{1}{m}\left(\frac{\partial H}{\partial T}\right)_p, \tag{7.1}$$

where, m is the mass and H is the enthalpy of the system.

We use the values for the thermal conductivity and specific heat capacity, as calculated using the methods above, to calculate the thermal diffusivity.

Axis	L	No. of Porosities	No. of Atoms	No. of Temperatures	Equilibration time (timesteps)	NEMD time (timesteps)	Total time (timesteps)
x	40	3	∼180 000	5	100 000	500 000	600 000
	60	3	∼270 000	5	100 000	500 000	600 000
	100	3	∼450 000	5	100 000	500 000	600 000
y	40	3	∼180 000	5	100 000	500 000	600 000
	60	3	∼270 000	5	100 000	500 000	600 000
	100	3	∼450 000	5	100 000	500 000	600 000
z	40	3	∼180 000	5	100 000	1 000 000	1 100 000
	60	3	∼270 000	5	100 000	1 000 000	1 100 000
	100	3	∼450 000	5	100 000	1 000 000	1 100 000

Table 7.1: Table of simulation parameters for various axes, supercell lengths in units of unit cells, number of porosities, number of atoms, number of temperatures, and simulation time, for a total of 135 simulations.

7.3 Results and discussion

7.3.1 Porosity

To examine any changes in the porosity during our simulations, the equilibrated supercell density was calculated by taking the supercell density after equilibration at each temperature and simulated porosity and then dividing by the density of the perfect supercell at the same temperature to find the fraction of the theoretical density. A plot showing how the porosities are affected by temperature are presented in Fig. 7.2. The legend refers to the simulated porosity of the initial configuration, which was defined by the percentage of atoms removed from the perfect crystal configuration to introduce the voids. We observe a small reduction in porosity with increasing temperature, due to the thermal expansion of the equilibrated supercell and that the case of a porosity of 11% shows the greatest reduction in porosity of $\sim$1%.

The difference in the calculated porosity by LAMMPS and OVITO is shown in Fig. 7.3. The LAMMPS porosity is calculated from the density of the system. The OVITO porosity is calculated using a surface mesh. This is done by identifying which particles can be considered part of the same region in terms of their proximity. Then geometric elements are created connecting these particles. The size of these elements depends on the chosen level of refinement. This forms the basis of the surface mesh. A probe sphere radius of 2.5 Å was chosen, based on the minimum pair separation distance of Li_2TiO_3.

At the lower porosities of 4% and 6%, the LAMMPS porosity is slightly lower than the one calculated by OVITO. However, at the higher 11% there is an interesting comparison. The porosities are calculated to be the same until $\sim$700 K, where the OVITO porosity becomes much lower with temperature. This implies that at high porosity, the atoms arrange themselves to fill in the void space more than seen at

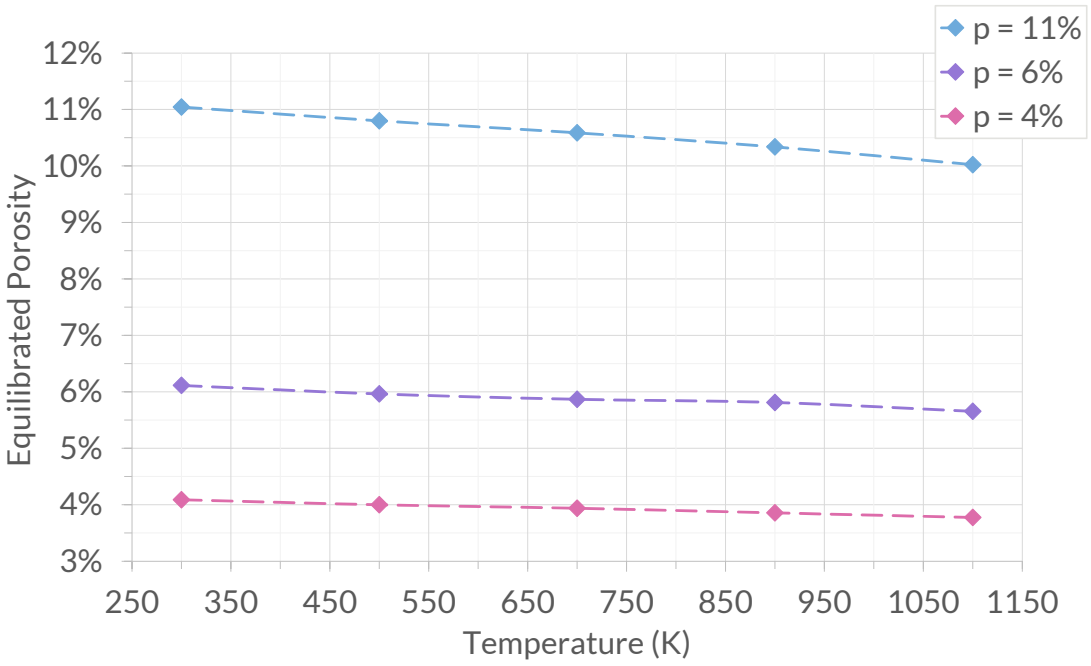

Figure 7.2: The equilibrated supercell porosity of the simulated supercells with 4.0%, 6.0%, and 11.0% atoms removed as compared to the perfect crystal density, with respect to temperature. Calculated from simulations in x with $L = 60$ unit cells.

lower porosity.

In Fig. 7.4 we see the supercell volume as a function of porosity for each of the studied temperatures. There are small changes in the volume observed which are better shown in Fig. 7.5 showing the supercell volume normalised to the perfect supercell at each temperature. We see that volume increases with porosity for $T = 300$ K but for all higher temperatures, there is a trend of decreasing volume with increasing temperature. We also see that for the same porosity $p = 2.83\%$, the volume is larger for supercells containing many voids versus single voids at $T = 300$ K and 500 K and smaller for higher temperatures.

7.3.2 Thermal Conductivity

Fig. 7.6 shows the calculated thermal conductivity in each spatial direction as a function of the temperature for a range of porosities, $p = 4.0\%$, 6.0%, and 11.0%,

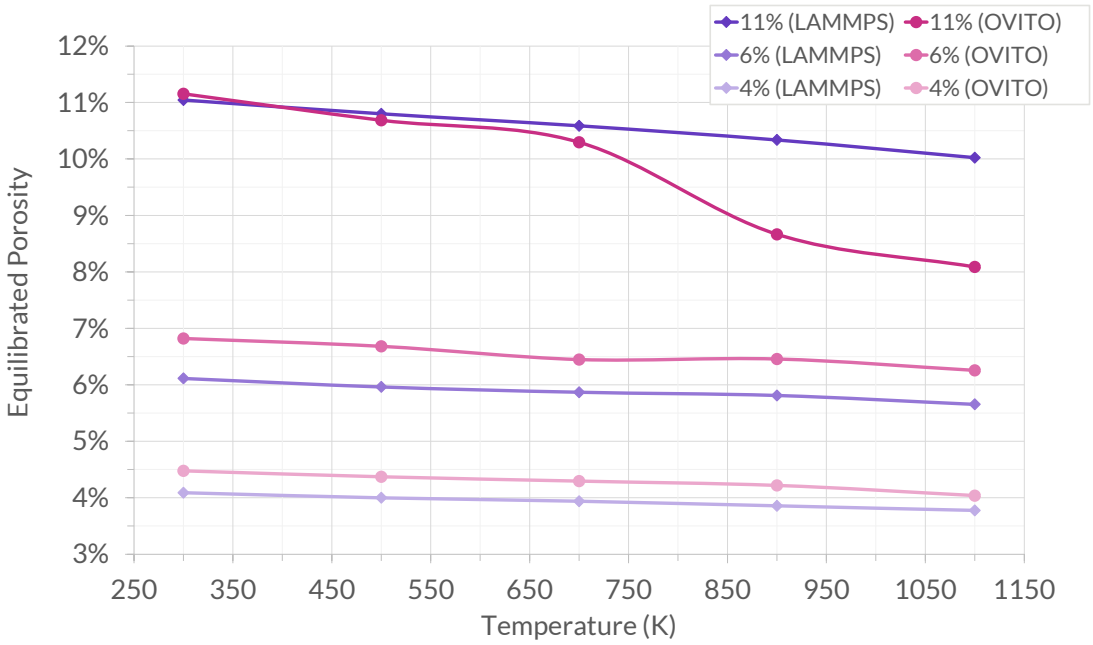

Figure 7.3: Comparison of calculated porosity by LAMMPS and by OVITO. The equilibrated supercell porosity of the simulated supercells with 4.0%, 6.0%, and 11.0% atoms removed as compared to the perfect crystal density, with respect to temperature. Calculated from simulations in x with $L = 60$ unit cells.

along with the perfect crystal results from Chapter 4. As shown in Fig. 7.6 we predict that the thermal conductivity decreases as the temperatures increases, however, this is less pronounced at the higher porosities. The hollow points presented in Figs. 7.6b and 7.6c are simulations where the crystal had melted at the hottest part of the simulation supercell. To enable the calculation of thermal conductivity using the Müller-Plathe methods involves the creation of a "hot" chunk and a "cold" chunk. When the cross sectional area of the supercell is small, due to the inclusion of the shorter a axis, the change in temperatures of these chunks is larger, which leads to the "hot" chunk reaching temperatures of >1600 K, which combined with nucleation points provided by the voids allows melt initiation that does not occur in the perfect crystal. A diagram of an example supercell where this has occurred is seen in Fig. 7.7. We have chosen to include this information to highlight how localised melting or a

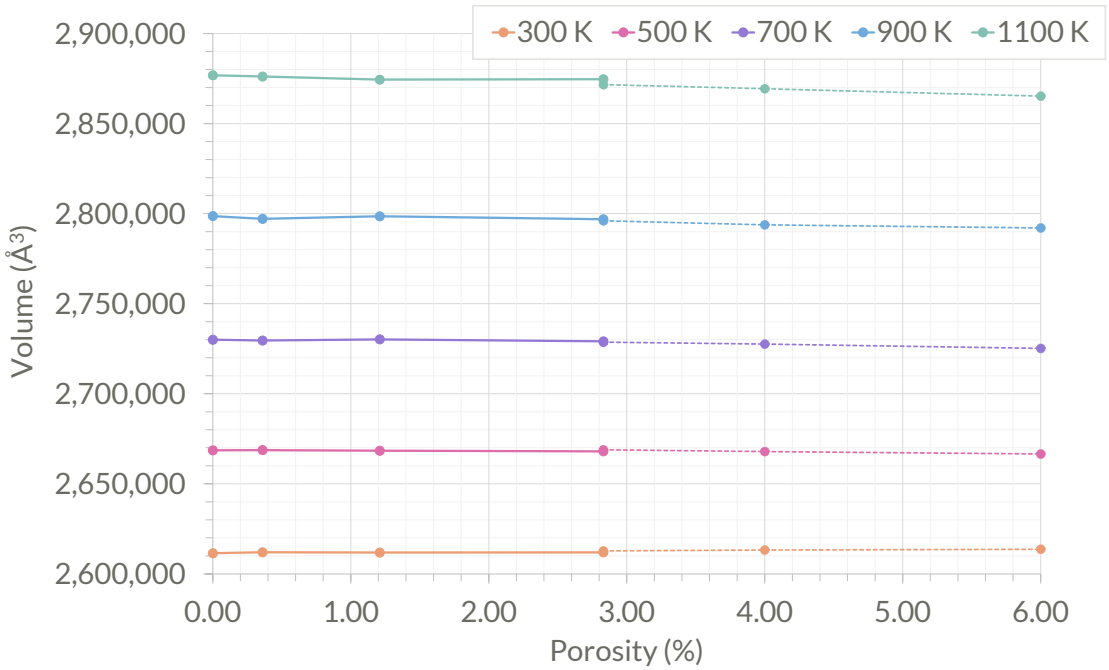

Figure 7.4: Supercell volume as a function of porosity for each of the studied temperatures. Where solid lines connect single void data and dashed lines connect many voids data. For this figure the same supercell size is compared. Calculated from simulations in x with $L = 60$ unit cells.

reduction in porosity might change the thermal conductivity of the material and that these types of changes may be responsible for the increased thermal conductivity at higher temperatures observed from experiment, as discussed in Chapter 4.

For calculations along the x-direction we see a slightly different trend between porosities than in the y- or z-directions. The calculated thermal conductivities for $p = 2.83\%$ and 4.00% largely overlap. This is again likely due to the larger cross-sectional area in x (see Fig. 4.2) leading to less inhibition of heat flow due to the presence of voids making the difference of 1.17% negligible.

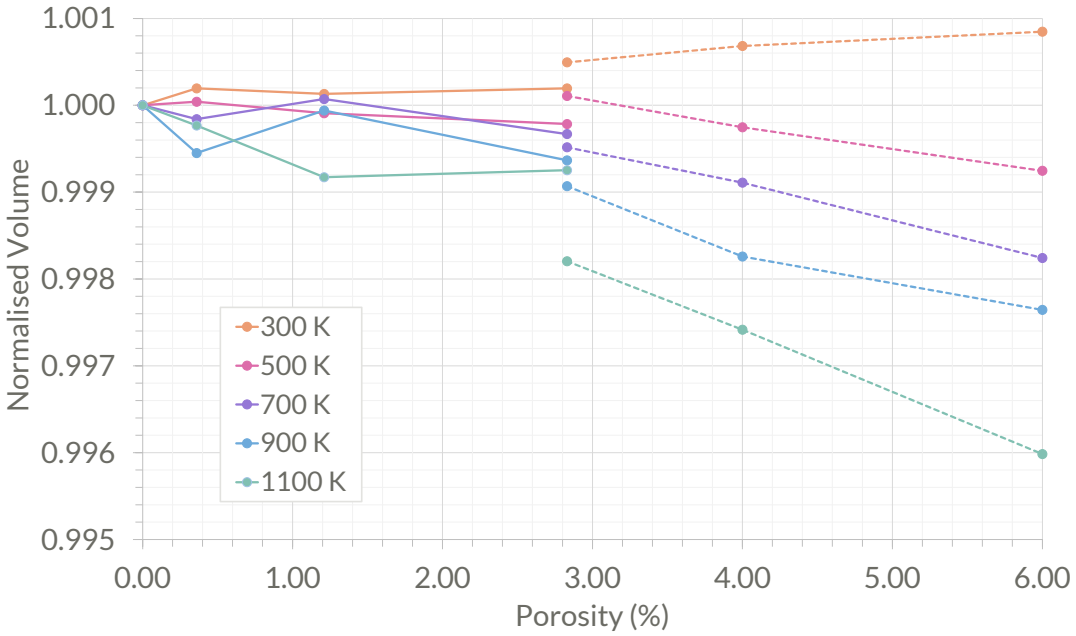

Figure 7.5: Supercell volume normalised to the perfect crystal supercell as a function of porosity for each of the studied temperatures. Where solid lines connect single void data and dashed lines connect many voids data. For this figure the same supercell size is compared. Calculated from simulations in x with $L = 60$ unit cells.

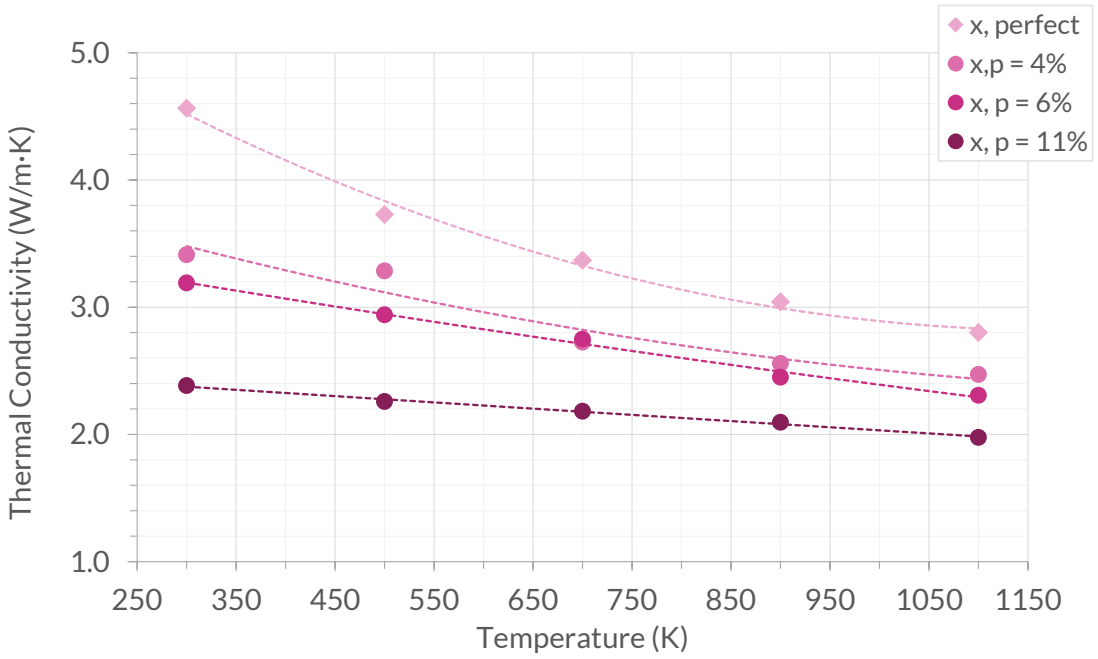
x, perfect
x,p = 4%
x, p = 6%
x, p = 11%
Thermal Conductivity (W/m·K)
5.0
4.0
3.0
2.0
1.0
250
350
450
550
650
750
850
950
1050
1150
Temperature (K)

(7.6a) x

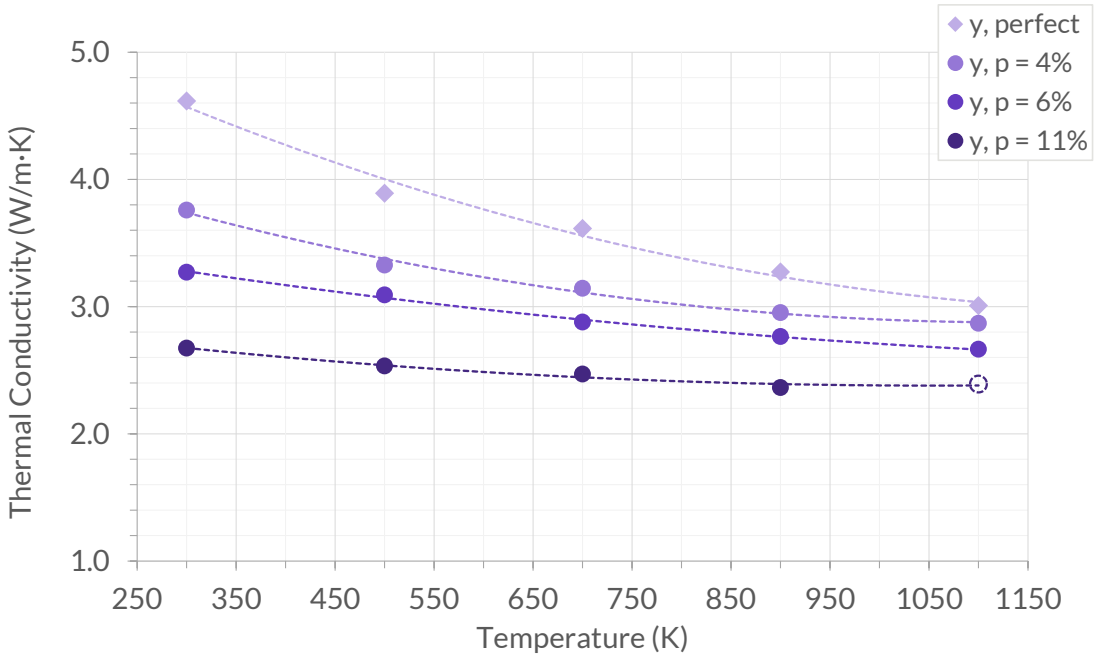
y, perfect
y, p = 4%
y, p = 6%
y, p = 11%
Thermal Conductivity (W/m·K)
5.0
4.0
3.0
2.0
1.0
250
350
450
550
650
750
850
950
1050
1150
Temperature (K)

(7.6b) y

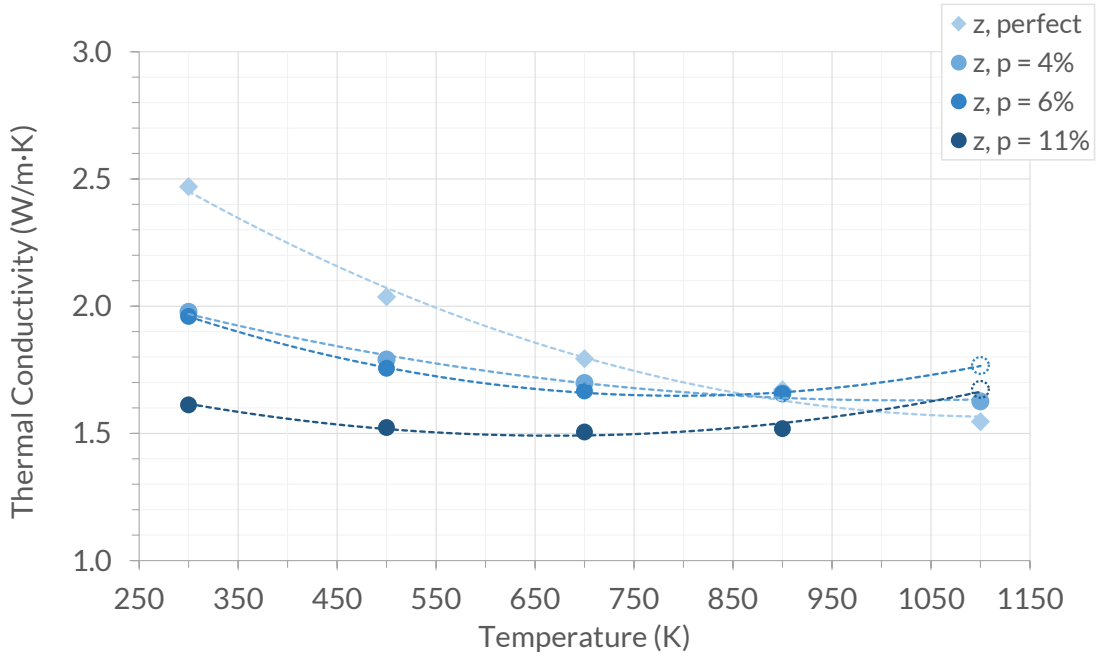

(7.6c) z

Figure 7.6: Calculated thermal conductivity for many randomly distributed voids of radius $r = 5$ Å- 10 Å, for porosities of $p = 4.0\%$, 6.0%, and 11.0%, in each of the spatial directions x, y, and z. Values extrapolated from simulations of cells sizes of 10×10 cross-section and $L = 40$, 60, and 100 unit cells in direction of calculation. Hollow points indicate simulations where the hottest regions of the simulation cell have melted (see main text for details).

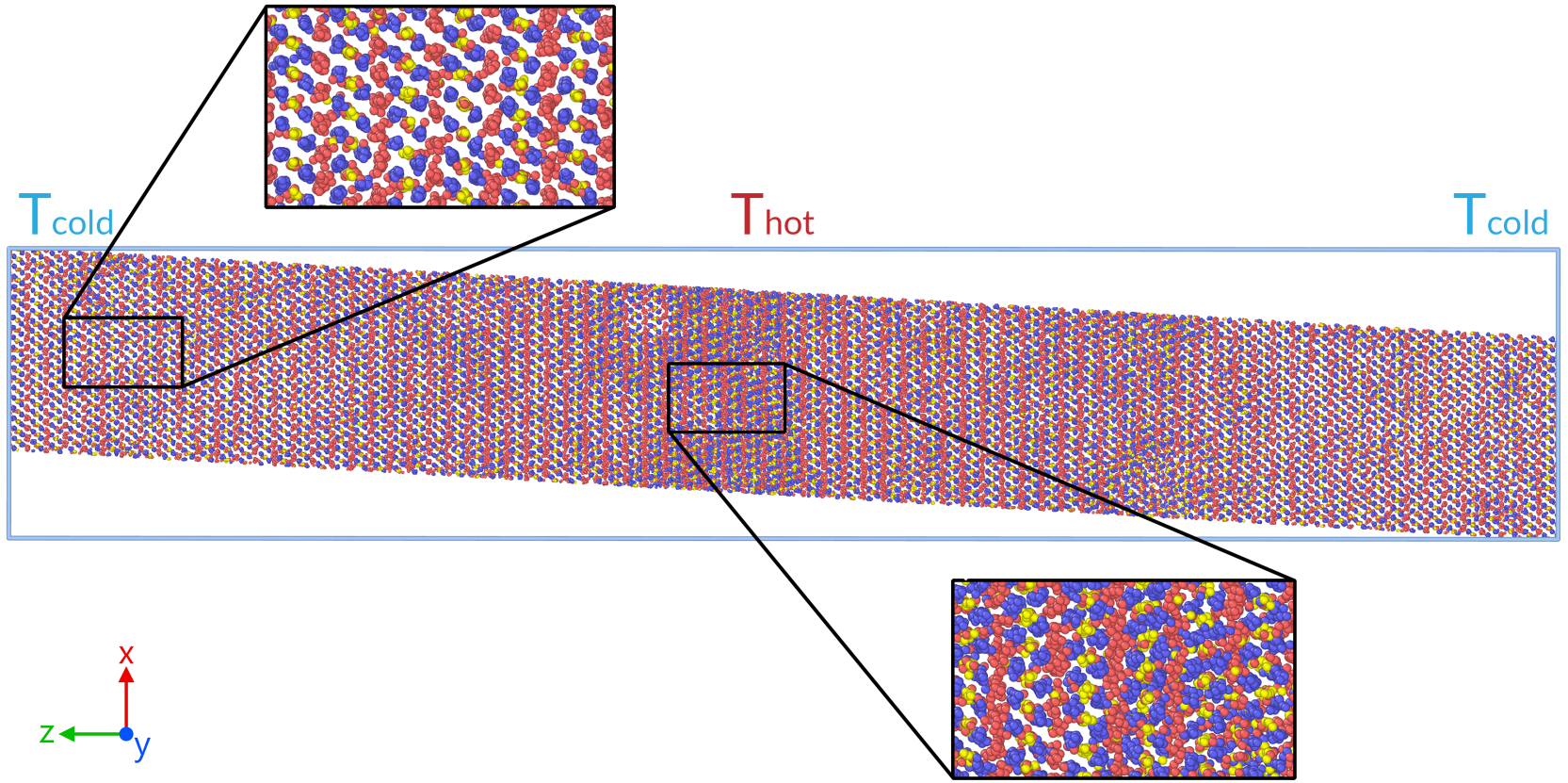

Figure 7.7: A supercell of Li_2TiO_3 of size 20×20×40 unit cells, at the last frame of the simulation at $T = 1100$ K. The crystal structure of the Li_2TiO_3 at the lower temperature region and the hotter temperature region are highlighted.

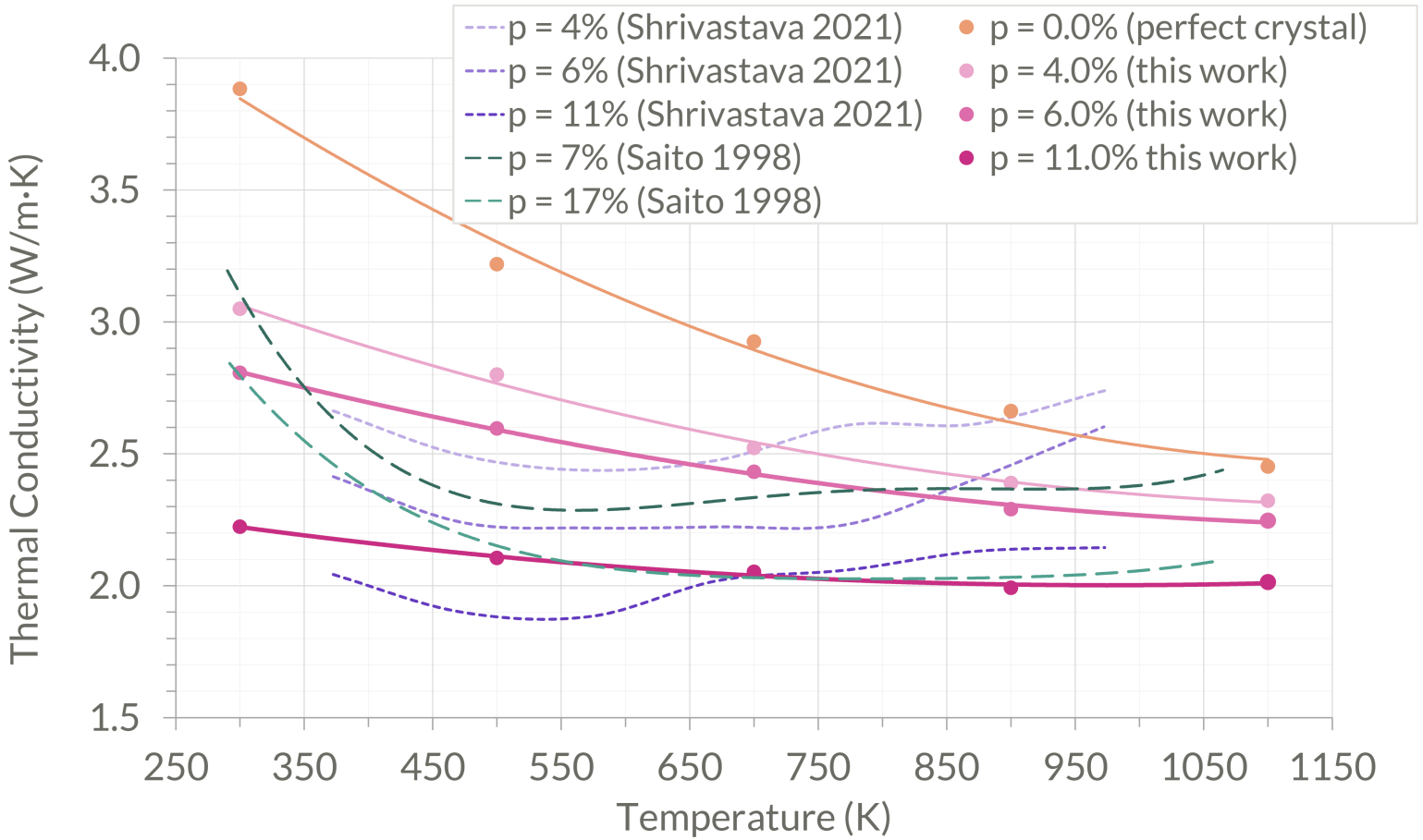

Figure 7.8: Calculated thermal conductivity of increased porosity/concentration of voids and perfect Li_2TiO_3 as a function of temperature. Values extrapolated from simulations of cells sizes of 10×10 cross-section and L = 40, 60, and 100 unit cells in direction of calculation. Shown alongside fourth-order polynomial fit of experimental data from [137, 157]

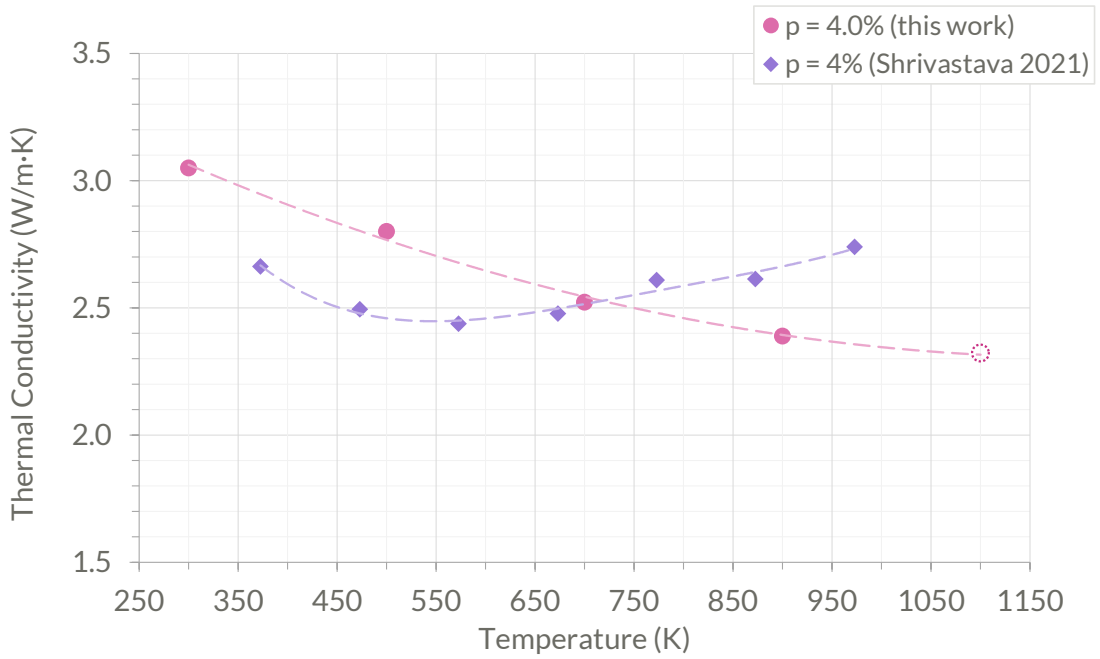
p = 4.0% (this work)
p = 4% (Shrivastava 2021)
Thermal Conductivity (W/m·K)
3.5
3.0
2.5
2.0
1.5
250
350
450
550
650
750
850
950
1050
1150
Temperature (K)

(7.9a) $p = 4\%$

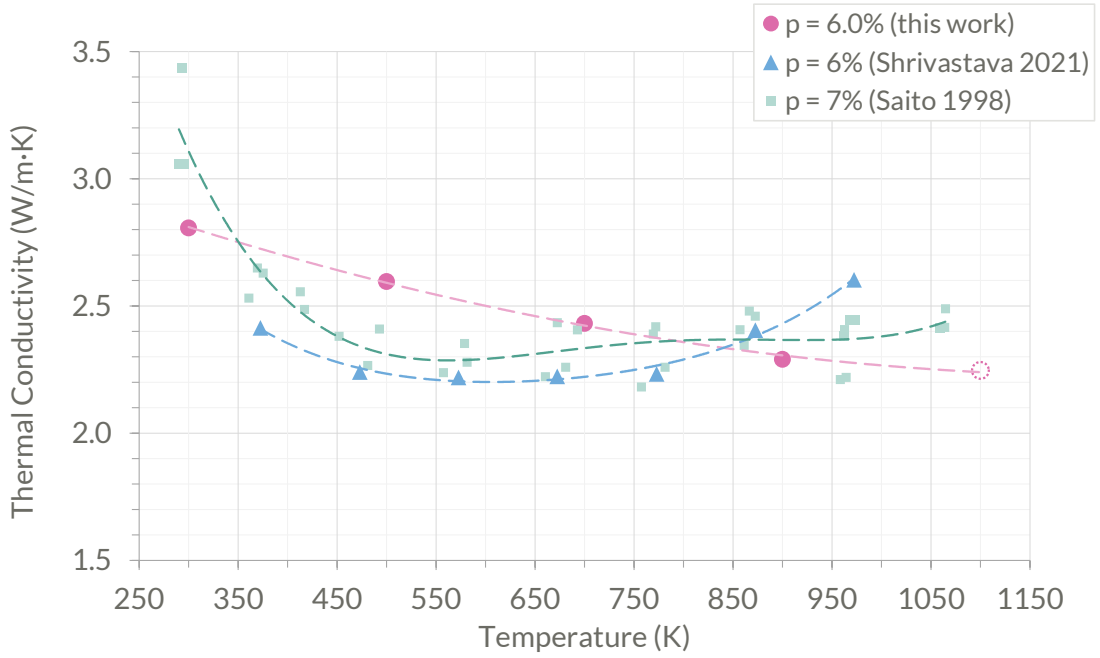
p = 6.0% (this work)
p = 6% (Shrivastava 2021)
p = 7% (Saito 1998)
Thermal Conductivity (W/m·K)
3.5
3.0
2.5
2.0
1.5
250
350
450
550
650
750
850
950
1050
1150
Temperature (K)

(7.9b) $p = 6\%$

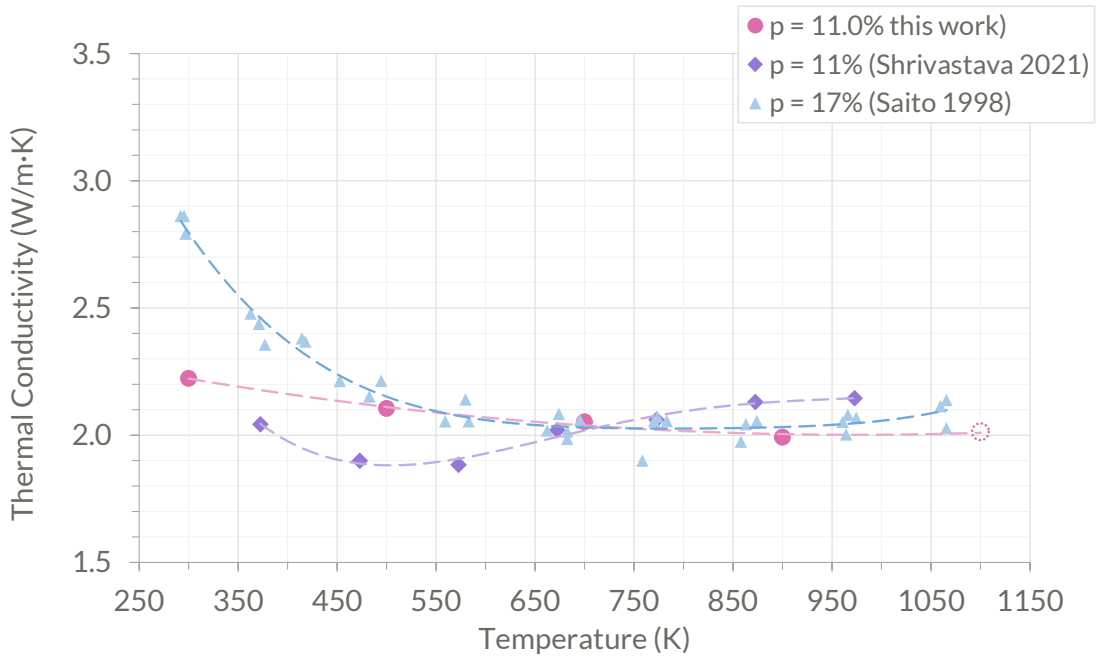

(7.9c) $p = 11\%$

Figure 7.9: Calculated thermal conductivity of concentration of voids (porosity $p = 4\%$, 6%, 11%) as a function of temperature. Hollow points indicate the inclusion of simulations where the hottest regions of the simulation cell have melted (see the main text for details). Shown alongside experimental data from [137, 157].

In order to perform a comparison of our results with experiments, which typically examine polycrystalline samples where the grains are randomly orientated, we calculate an average of the thermal conductivities in the x, y and z directions. In Fig. 7.8 the average extrapolated thermal conductivity with respect to temperature for the three simulated porosities is presented, along with the perfect crystal results, seen in Chapter 4, for comparison. The plot shows that the overall thermal conductivity decreases with increasing temperature. The use of randomly distributed voids shows good agreement with experiment. This allows a comparison of our data with the work of Shrivastava *et al.* and Saito *et al.*. An overview of the results obtained in this chapter and seen in the literature can be seen in Fig. 7.8. To look at each porosity in more detail this has been further split up into three separate graphs showing the 4%, 6%, and 11% porosities in Fig. 7.9.

Fig. 7.9a shows a comparison between the data obtained for a porosity of 4% in this chapter with the experimental results of Shrivastava *et al.* with the same porosity. The values predicted for the thermal conductivity agree well with these previous experimental data; however, the trend is quite different. While Shrivastava *et al.* find that the thermal conductivity increases from about 550 K, we do not see this effect in our simulations.

Similarly, Fig. 7.9b shows that our predicted thermal conductivities for Li_2TiO_3 with a porosity of 6% are in good agreement with both Shrivastava *et al.* as well as Saito *et al.*'s sample with a porosity of 7%, however, again we do not observe the increase in thermal conductivity at high temperature seen in the experimental results.

In Fig. 7.9c we compared the 11% data obtained in this chapter to experimental results from Shrivastava *et al.* for 11%, as well as from Saito *et al.* for 7%, and 17%. Saito *et al.* measures a much higher thermal conductivity at low temperature for their 17% porosity samples than Shrivastava *et al.* for their 11% samples and our calculated thermal conductivity. At high temperature, the thermal conductivity

determined by Saito *et al.* for their 17% porosity sample is very similar to our data, but there is again an increase in the thermal conductivity measured by Shrivastava *et al.* which we do not observe.

In Fig. 7.10 we see the thermal conductivity with respect to porosity. For all temperatures the thermal conductivity is reduced with increasing porosity. In Fig. 7.11 we compare the thermal conductivity with respect to porosity of the single voids vs the many voids. A single data set of $p = 2.83\%$ many voids was run for $L = 60$ supercells to allow comparison to the largest single void data from the previous chapter. We see that the trend between thermal conductivity and porosity is largely the same, with the steepest change occurring between the perfect crystal and the smallest void of radius $r = 10$ Å

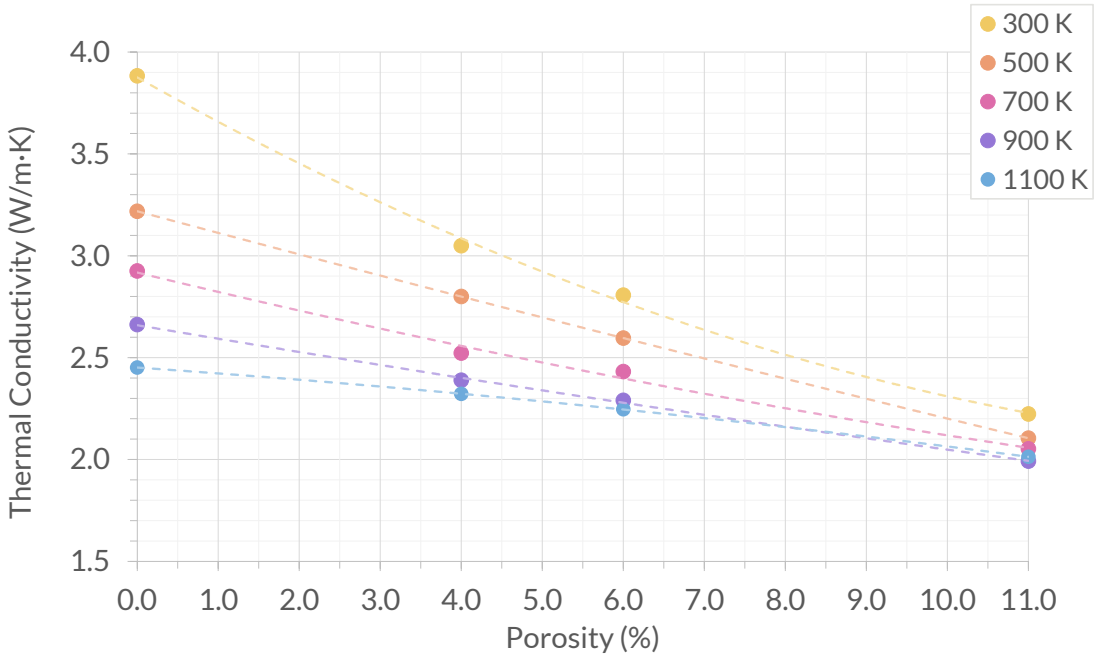

Figure 7.10: The extrapolated average calculated thermal conductivity with respect to porosity for each studied temperature for supercells containing many randomly distributed voids.

This difference between large single voids and many small voids is further investigated in Fig. 7.12. We compare the calculated thermal conductivities for $p = 2.83\%$

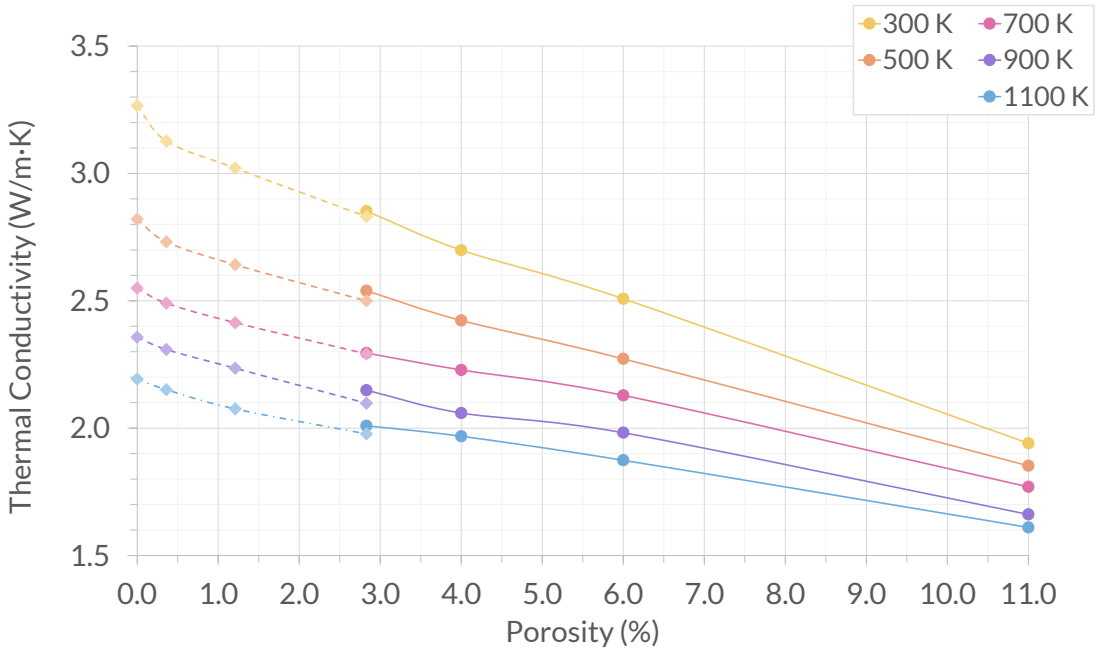

Figure 7.11: The average calculated thermal conductivity with respect to porosity for each studied temperature for supercells containing single voids (dashed lines) and many randomly distributed voids (solid lines). N.B. this is for the same supercell size not the extrapolated values, so that comparison can be made with the single voids data from the previous chapter. For supercells of $L = 60$.

as obtained from supercells containing a single void and those containing many voids. We see that the calculated values are slightly lower for the single larger void than for the many smaller voids. This suggests that void size is a factor as well as the porosity in the overall thermal conductivity.

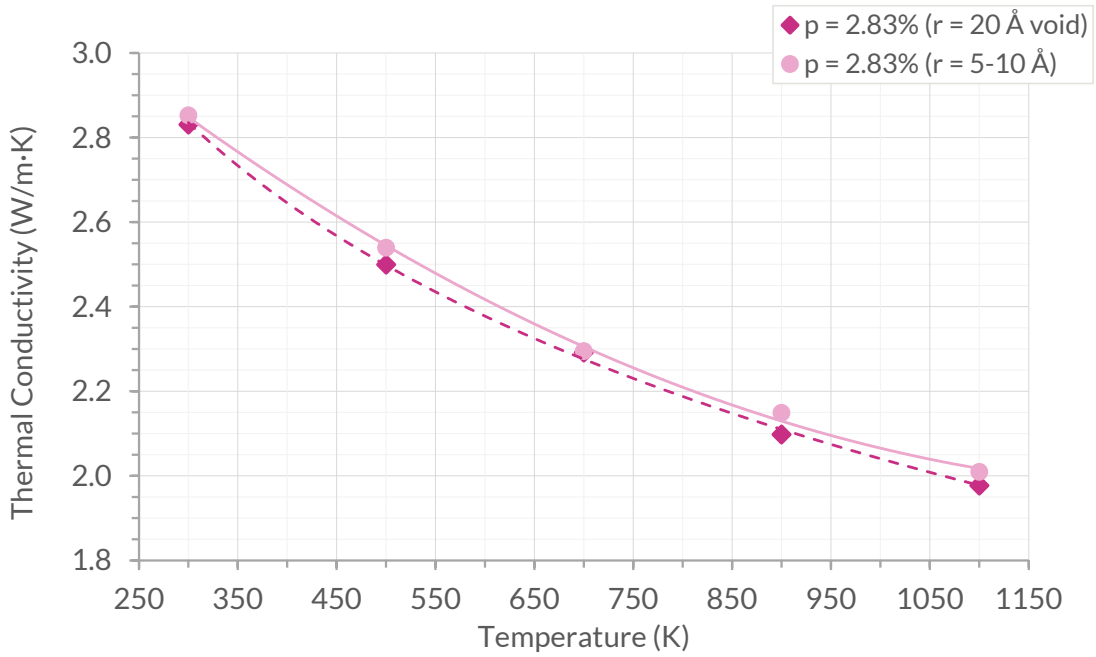

Figure 7.12: Comparison between the thermal conductivity calculations for the single void (r = 20 Å) and the many voids (radius range r = 5-10 Å) for the same simulated porosity p = 2.83%.

7.3.3 Thermal Diffusivity

To examine the thermal diffusivity, it is necessary to first determine the specific heat capacity for Li_2TiO_3 as predicted by the potential. This is plotted in Fig. 7.13 for the perfect crystal and our supercells containing different levels of porosity alongside experimental data from the literature. Immediately evident from Fig. 7.13 is that the pair potential does a relatively poor job of reproducing C_p at low temperature; however, it provides a much improved match to the experimental data at high temperature. The origin of this discrepancy is likely the parameterisation of the potential itself, which was not fitted to the specific heat. It is widely appreciated that empirical pair potentials may fail to reproduce properties that they have not been fitted to [159, 160]. It is also interesting to note that there are small differences in the specific heat capacity with porosity, particularly at low temperature.

Using these calculated values of C_p, the thermal diffusivities can be determined

using Eq. 2.7 and in Fig. 7.14 the thermal diffusivity is shown, along with experimental data from the literature. The thermal diffusivity decreases with increasing temperature. Due to the inclusion of material density into the calculation of the thermal diffusivity, this value should be easily comparable to experimental data using samples of various porosities. In general, we see good agreement between the values calculated in this chapter and the literature [136, 137, 157]. However, at low temperature the predicted thermal diffusivity is slightly lower than experiment and this is likely due to the potential overestimating the specific heat. It may be anticipated that the inclusion of the density in Eq. 2.7 should remove any impact of porosity on the thermal diffusivity; however, we predict that porosity does have a small effect on the thermal diffusivity and this is also evident in the experimental results.

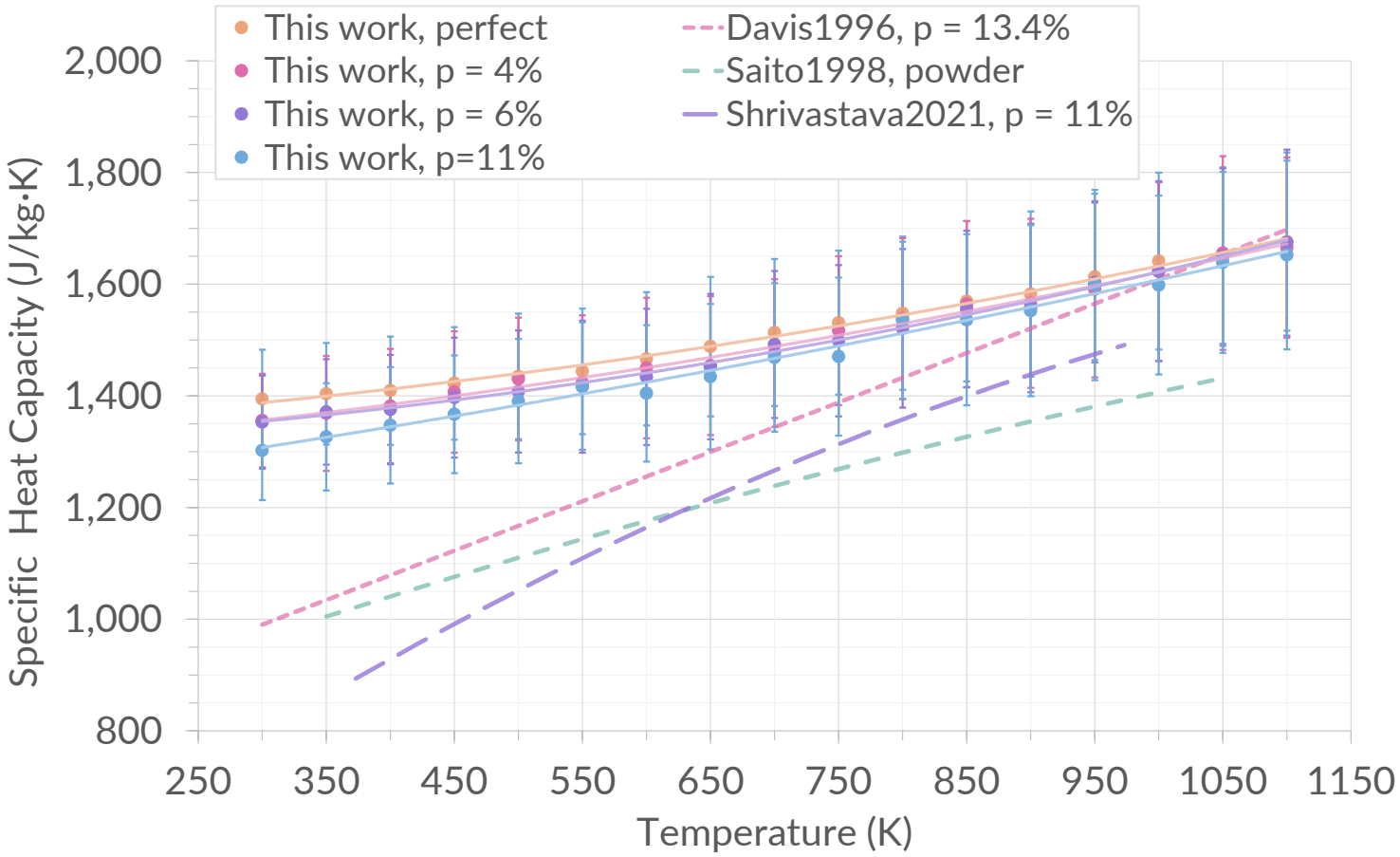

Figure 7.13: The calculated isobaric specific heat capacity with respect to temperature, using 10×10×10 unit cells of porosity $p = 0$ (perfect crystal), 4, 6, and 11% in NPT conditions. The uncertainty of each data point was calculated by the standard deviation of the difference of means. Shown alongside experimental data from the literature [136, 137, 157].

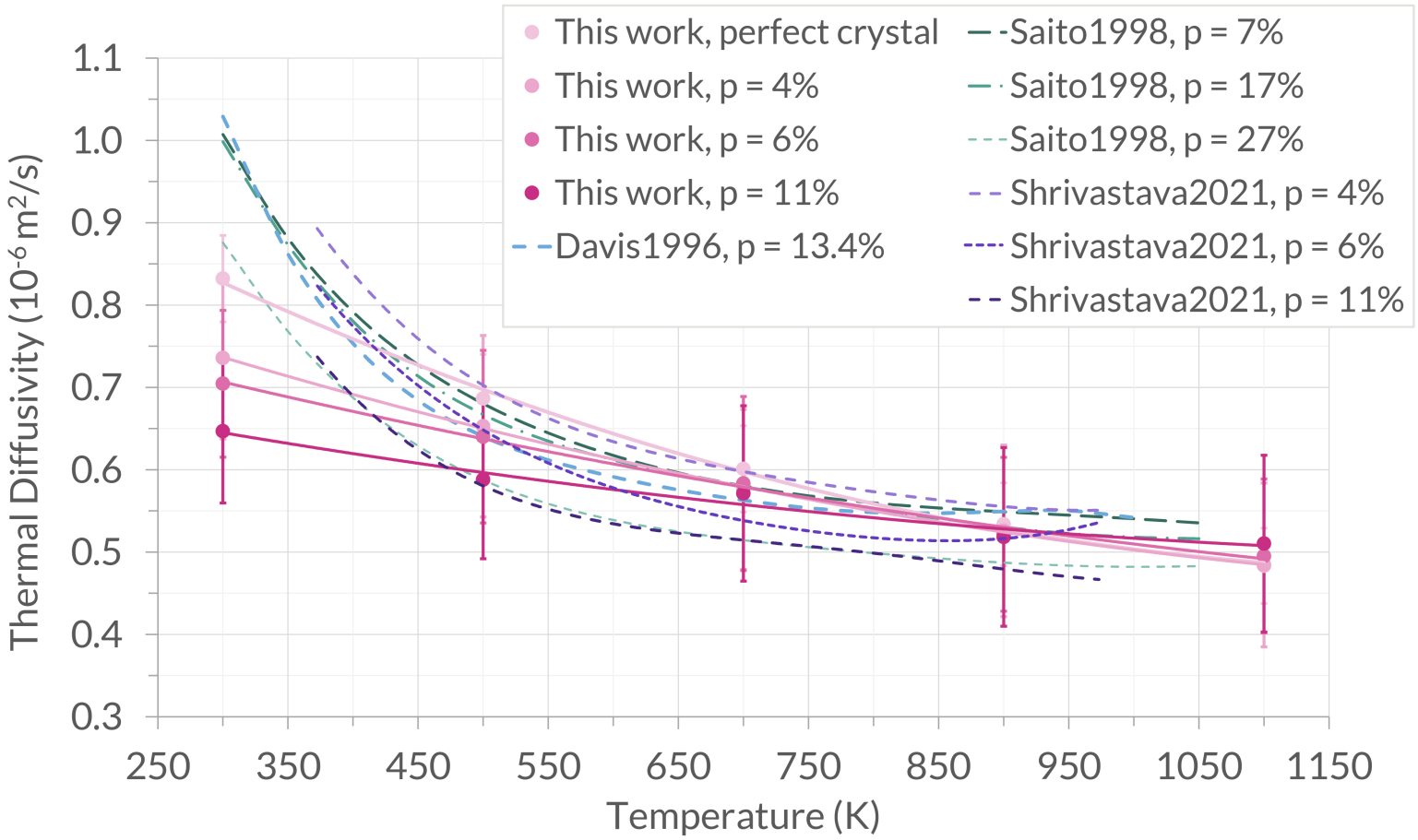

Figure 7.14: The calculated diffusivity with respect to temperature, using Eq. 2.7 with thermal conductivity values for the perfect crystal from Chapter 4 and for porosities $p = 4$, 6, and 11% from this work, shown alongside the polynomial fit of experimental data from the literature [136, 137, 157].

7.4 Summary

In this chapter, we have used molecular dynamics simulations to examine how the introduction of porosity will impact the thermal conductivity of Li_2TiO_3 ceramic breeder material. Our simulations predict that the thermal conductivity will decrease with increasing porosity at all temperatures in the range examined, in agreement with experimental data. We also find that the thermal conductivity at each porosity as a function of temperature also decreases with increasing temperature, which is in contrast to some experimental analyses that show an increase in thermal conductivity at higher temperatures despite an initial decrease that is more consistent with our results. We speculate that this increase is not due to any intrinsic increase in thermal transport with increasing temperature but due to the sintering of the experimental samples during testing reducing the porosity of the samples, a phenomena that would not be captured in the simulations of this work, where the porosity is set at each temperature simulated. Whether such sintering would be seen during reactor operation will depend on the operating temperature of the material and how well sintered the material is prior to introduction to a reactor.

8

Conclusions

8.1 Summary

In this thesis we have demonstrated that atomistic simulation can be used to provide information that is not easily accessible by experiment, as well as add context to experimental observations. The thermal conductivity of Li_2TiO_3 can be well modelled using NEMD. We have characterised the anisotropy in the thermal conductivity, as predicted by the anisotropic crystal structure of Li_2TiO_3. We consistently observe lower thermal conductivity in the z direction, compared with x, and y, for all simulated scenarios in this work; the bulk crystal, non-stoichiometry for Li rich and Li poor, single voids, and increasing porosity. The thermal conductivity of the bulk crystal was calculated to provide a direct comparison to the subsequent systems including defects. The anisotropic thermal conductivity is directly caused by the differences in the crystal structure of Li_2TiO_3 along the z-axis vs the x and y. The difference in crystal structure ultimately means that the bonding is difference and hence the elastic properties of the material. This anisotropy could potentially be exploited by using particularly oriented tiles of Li_2TiO_3 instead of spheres of randomly oriented Li_2TiO_3. This could maximise the thermal conductivity that can be achieved in the blanket module.

Studying the effect of non-stoichiometry in Li_2TiO_3 was an insightful look into the effect of many types of point defects, and the multiple stages expected in the lifetime of a blanket material; the lithium enriched starting material down to the lithium burn up from use. Non-stoichiometry is accommodated by lithium defects and antisites which is in excellent agreement with DFT despite the potential not having been fitted to the defect energies. We observe that there is no significant difference in the thermal conductivity at operational temperatures between the non-stoichiometric systems and the bulk crystal. This suggests that neither enriching the blanket with Li nor Li burnup is a significant concern in terms of the efficiency of heat transfer through the material. The previously discussed literature which suggested that non-stoichiometry increases thermal conductivity [138, 149, 152] is likely related to grain sizes being bigger in the non-stoichiometric samples. Since the change in stoichiometry does not cause a significant drop in thermal conductivity this will have implications for reactor efficiency and thermal stresses in the pebbles themselves.

Introducing single, charge-neutral, voids allowed the investigation of thermal transport effects of increased void size. The thermal conductivity was decreased by increased void size, as expected due to the lack of conductive media in the voids. To study the effect of porosity, we took the methodology for creating a single void, and applied it to form supercells with many smaller voids, made up to a desired percentage. This allowed for more comparable results to the literature. We find that the thermal conductivity decreases with decreased void size, and do not observe recovery in the thermal conductivity at higher temperatures as seen in some of the literature. This implies that this trend is not intrinsic to the crystal structure of Li_2TiO_3 as the large majority of its thermal conductivity is the phonon component, which is simulated in this work. It is unlikely the increase in thermal conductivity seen in the literature can be attributed to the photon component alone. We suggest that this may be due to annealing in the experiment samples which would not be

observed in simulation work at small timescales. The porosity of Li_2TiO_3 is found to be directly related to the thermal conductivity and thus the porosity of the blanket material should be carefully chosen not to reduce the thermal conductivity by too much, and greatly reduce the efficiency of electricity generation for the entire reactor. The porosity appears to have the most significant impact on the thermal conductivity of the factors considered here. There is a trade-off to be made here, in that open porosity is desirable to contribute to tritium release, but this will have an impact on the thermal conductivity. It is also important to note that it is unknown whether the pebbles will undergo in-reactor sintering, or whether they have been thoroughly sintered beforehand so this may not happen in reactor.

8.2 Future work

This work has made a concerted effort to describe the effects of various defect types on heat transfer through Li_2TiO_3. However, there remain other specific behaviours induced by the crystal structure than remain unexplored. Firstly, from reviewing fabrication methods for Li_2TiO_3, we see the wide array of different grain sizes that can be expected in the material. As seen in Chapter 4, our calculated thermal conductivity for Li_2TiO_3 is higher than is observed experimentally; this is due to grain boundaries. The phonon grain boundary resistance in UO_2 is examined by Kim, Shim, and Kaviany [161], observing the decrease in thermal conductivity by phonon scattering. A broader study with polycrystals is done by Shen *et al.* [162] for Li_4SiO_4. This highlights the importance of understanding how grain size and grain boundaries affect the thermal conductivity, which will need to be investigated in future work.

Furthermore, it would be appropriate to supplement this work with analysis on how the thermal conductivity is affected by larger group of different defects as could be investigated by running damage cascade simulations in Li_2TiO_3. This is

a computationally costly endeavour due to the large supercell sizes and timescales likely to be required. However, the realistic arrangement of defects that would be produced would be a valuable insight into the combined effects of various defects.

The empirical pair potential employed in this work has demonstrated a perhaps surprising efficacy to reproduce the defect chemistry of the material, however, it does a very poor job of reproducing the specific heat at low temperatures. It is widely appreciated that potentials employing specific forms, such as the Buckingham potential employed here, are good at reproducing the properties that they are fitted to and perform less well for other properties. Therefore, we would recommend developing an improved potential for Li_2TiO_3, conceivably using something like a machine learning approach. Chan *et al.* [163] discuss the use of machine learning to improve and speed up the development of interatomic potentials for a range of materials. By using machine learning the training procedures can optimised, which can otherwise require years of development.

There is much discussion in the field about composite ceramics, such as Li_2TiO_3-Li_4SiO_4. At the beginning of this thesis, Li_2TiO_3 was chosen from these two leading ceramic breeders for this work, however, Li_4SiO_4 remains a good choice for a breeder blanket material. Combining the two materials together has the potential to allow blanket designs to benefit from the advantages of both ceramics instead of having to settle for one, e.g. the thermal conductivity could be improved while also improving the Li content. The effect of thermal conductivity in Li_2TiO_3-Li_4SiO_4 could be similarly calculated as done in this work with the development of a suitable interatomic potential which could again potentially be more easily developed by utilising machine learning techniques.

The figures obtained in this thesis for the thermal conductivity of Li_2TiO_3 can be integrated into higher order tokamak models such as that for the HCPB TBM in ITER, and thus could improve predictions of the thermal conductivity and other properties of the test blanket.

Bibliography

[1] M. Kovari, M. Coleman, I. Cristescu, and R. Smith. "Tritium resources available for fusion reactors". In: *Nuclear Fusion* 58.2 (2017), p. 026010.

[2] R. L. Murray and K. E. Holbert. *Nuclear Energy - An Introduction to the Concepts, Systems, and Applications of Nuclear Processes (7th Edition)*. Elsevier, 2015. Chap. 26, pp. 477–489.

[3] G. Federici, L. Boccaccini, F. Cismondi, M. Gasparotto, Y. Poitevin, and I. Ricapito. "An overview of the EU breeding blanket design strategy as an integral part of the DEMO design effort". In: *Fusion Engineering and Design* 141 (2019), pp. 30–42.

[4] T. Ihli, T. Basu, L. Giancarli, S. Konishi, S. Malang, F. Najmabadi, S. Nishio, A. Raffray, C. Rao, A. Sagara, and Y. Wu. "Review of blanket designs for advanced fusion reactors". In: *Fusion Engineering and Design* 83.7 (2008). Proceedings of the Eight International Symposium of Fusion Nuclear Technology, pp. 912–919.

[5] G. Federici, W. Biel, M. Gilbert, R. Kemp, N. Taylor, and R. Wenninger. "European DEMO design strategy and consequences for materials". In: *Nuclear Fusion* 57.9 (2017), p. 092002.

[6] K. Miyamoto. *Plasma Physics for Controlled Fusion*. 2nd ed. Springer-Verlag Berlin Heidelberg, 2016.

[7] M. Kikuchi, K. Lackner, and M. Q. Tran, eds. *Fusion Physics*. Non-serial Publications. Vienna: International Atomic Energy Agency, 2012.

[8] LibreTexts, Physics. URL: https://phys.libretexts.org/.

[9] S. M. Gonzalez de Vicente, N. A. Smith, L. El-Guebaly, S. Ciattaglia, L. Di Pace, M. Gilbert, R. Mandoki, S. Rosanvallon, Y. Someya, K. Tobita, and D. Torcy. "Overview on the management of radioactive waste from fusion facilities: ITER, demonstration machines and power plants". In: *Nuclear Fusion* 62.8 (2022), p. 085001.

[10] H. Abu-Shawareb *et al.* "Achievement of Target Gain Larger than Unity in an Inertial Fusion Experiment". In: *Phys. Rev. Lett.* 132 (2024), p. 065102.

[11] P. H. Rebut and B. E. Keen. "The JET Experiment: Evolution, Present Status, and Prospects". In: *Fusion Technology* 11.1 (1987), pp. 13–42.

[12] B. Penaflor, J. Ferron, R. Johnson, and D. Piglowski. "Current status of the upgraded DIII-D real-time digital plasma control system". In: *Fusion Engineering and Design* 71.1 (2004). 4th IAEA Technical Meeting on Control, Data Acquistion, and Remote Participation for Fusion Research, pp. 47–52.

[13] A. Sykes, R. Akers, L. Appel, E. Arends, P. Carolan, N. Conway, G. Counsell, G. Cunningham, A. Dnestrovskij, Y. Dnestrovskij, A. Field, S. Fielding, M. Gryaznevich, S. Korsholm, E. Laird, R. Martin, M. Nightingale, C. Roach, M. Tournianski, M. Walsh, C. Warrick, H. Wilson, S. You, M. Team, and N. Team. "First results from MAST". In: *Nuclear Fusion* 41.10 (2001), p. 1423.

[14] S. McNamara, O. Asunta, J. Bland, P. Buxton, C. Colgan, A. Dnestrovskii, M. Gemmell, M. Gryaznevich, D. Hoffman, F. Janky, J. Lister, H. Lowe, R. Mirfayzi, G. Naylor, V. Nemytov, J. Njau, T. Pyragius, A. Rengle, M. Romanelli, C. Romero, M. Sertoli, V. Shevchenko, J. Sinha, A. Sladkomedova, S. Sridhar, Y. Takase, P. Thomas, J. Varje, B. Vincent, H. Willett, J. Wood, D. Zakhar, D. Battaglia, S. Kaye, L. Delgado-Aparicio, R. Maingi, D. Mueller,

M. Podesta, E. Delabie, B. Lomanowski, O. Marchuk, and the ST40 Team. "Achievement of ion temperatures in excess of 100 million degrees Kelvin in the compact high-field spherical tokamak ST40". In: *Nuclear Fusion* 63.5 (2023), p. 054002.

[15] P.-H. Rebut. "ITER: the first experimental fusion reactor". In: *Fusion Engineering and Design* 30.1 (1995), pp. 85–118.

[16] R. Kemp, R. Wenninger, G. Federici, H. Reimerdes, R. Ambrosino, R. Brown, and M. Coleman. "Exploring a broad spectrum of design options for DEMO". In: *Fusion Engineering and Design* 136 (2018). Special Issue: Proceedings of the 13th International Symposium on Fusion Nuclear Technology (ISFNT-13), pp. 970–974.

[17] J. D. Lawson. "Some Criteria for a Power Producing Thermonuclear Reactor". In: *Proceedings of the Physical Society. Section B* 70.1 (1957), p. 6.

[18] J. F. S. L. J. Wittenberg and G. L. Kulcinski. "Lunar Source of 3He for Commercial Fusion Power". In: *Fusion Technology* 10.2 (1986), pp. 167–178.

[19] Dreamstime (Stock Images). URL: https://www.dreamstime.com/matter-different-states-example-water-molecular-form-solid-liquid-gas-plasma-vector-diagram-educational-science-use-image155298471.

[20] A. Fridman and L. A. Kennedy. *Plasma Physics and Engineering*. Taylor & Francis Group, 2011.

[21] ENDF. URL: https://www-nds.iaea.org/exfor/endf.htm.

[22] J. D. Strachan *et al.* "Fusion power production from TFTR plasmas fueled with deuterium and tritium". In: *Phys. Rev. Lett.* 72 (22 1994), pp. 3526–3529.

[23] H. Wilson, I. Chapman, T. Denton, W. Morris, B. Patel, G. Voss, C. Waldon, and the STEP Team. "STEP—on the pathway to fusion commercialization". In: *Commercialising Fusion Energy*. 2053-2563. IOP Publishing, 2020, 8-1 to 8–18.

[24] D. Clery. *The new shape of fusion.* URL: https://www.science.org/doi/10.1126/science.348.6237.854.

[25] M. Osakabe, Y. Takeiri, T. Morisaki, G. Motojima, K. Ogawa, M. Isobe, M. Tanaka, S. Murakami, A. Shimizu, K. Nagaoka, H. Takahashi, K. Nagasaki, H. Takahashi, T. Fujita, Y. Oya, M. Sakamoto, Y. Ueda, T. Akiyama, H. Kasahara, S. Sakakibara, R. Sakamoto, M. Tokitani, H. Yamada, M. Yokoyama, and Y. Yoshimura. "Current Status of Large Helical Device and its Prospect for Deuterium Experiment". In: *Fusion Science and Technology* 72.3 (2017), pp. 199–210.

[26] T. S. Pedersen, T. Andreeva, H.-S. Bosch, S. Bozhenkov, F. Effenberg, M. Endler, Y. Feng, D. Gates, J. Geiger, D. Hartmann, H. Hölbe, M. Jakubowski, R. König, H. Laqua, S. Lazerson, M. Otte, M. Preynas, O. Schmitz, T. Stange, Y. Turkin, and the W7-X Team. "Plans for the first plasma operation of Wendelstein 7-X". In: *Nuclear Fusion* 55.12 (2015), p. 126001.

[27] D. J. Campbell, T. Akiyama, R. Barnsley, M. Bassan, L. R. Baylor, L. Bertalot, F. Escourbiac, L. M. Giancarli, P. Gitton, J. Guirao, M. Kocan, V. Krasilnikov, U. Kruezi, M. Lehnen, S. Maruyama, Y. Ma, M. Merola, N. Mitchell, C. S. Pitcher, A. R. Raffray, R. Reichle, P. Shigin, A. Sirinelli, V. Udintsev, J. G. van der Laan, G. Vayakis, A. Wallander, M. Walsh, C. Watts, and the ITER Organization, Domestic Agencies and Collaborators, I.T.E.R. "Innovations in Technology and Science R&D for ITER". In: *Journal of Fusion Energy* 38.1 (2019), pp. 11–71.

[28] G. McCracken and P. Stott. *Fusion: The energy of the universe.* en. Complementary science series. San Diego, CA: Elsevier Academic Press, 2005.

[29] L. Giancarli, M. Dalle Donne, and W. Dietz. "Status of the European breeding blanket technology". In: *Fusion Engineering and Design* 36.1 (1997), pp. 57–74.

[30] D. Rapisarda, I. Fernández-Berceruelo, A. García, J. García, B. Garcinuño, M. González, C. Moreno, I. Palermo, F. Urgorri, and A. Ibarra. "The European Dual Coolant Lithium Lead breeding blanket for DEMO: status and perspectives". In: *Nuclear Fusion* 61.11 (2021), p. 115001.

[31] F. A. Hernández, P. Pereslavtsev, G. Zhou, Q. Kang, S. D'Amico, H. Neuberger, L. V. Boccaccini, B. Kiss, G. Nádasi, L. Maqueda, I. Cristescu, I. Moscato, I. Ricapito, and F. Cismondi. "Consolidated design of the HCPB Breeding Blanket for the pre-Conceptual Design Phase of the EU DEMO and harmonization with the ITER HCPB TBM program". In: *Fusion Engineering and Design* 157 (2020), p. 111614.

[32] K. N. Goswami and S. T. Murphy. "Influence of Lithium Vacancy Defects on Tritium Diffusion in β-Li_2TiO_3 ". In: *The Journal of Physical Chemistry C* 124.23 (2020), pp. 12286–12294.

[33] F. Hernández, P. Pereslavtsev, Q. Kang, P. Norajitra, B. Kiss, G. Nádasi, and O. Bitz. "A new HCPB breeding blanket for the EU DEMO: Evolution, rationale and preliminary performances". In: *Fusion Engineering and Design* 124 (2017). Proceedings of the 29th Symposium on Fusion Technology (SOFT-29) Prague, Czech Republic, September 5-9, 2016, pp. 882–886.

[34] J. H. Lienhard IV and J. H. Lienhard V. *A heat transfer textbook*. 5th ed. Dover Publications, 2020.

[35] L. Snead, S. Zinkle, and D. White. "Thermal conductivity degradation of ceramic materials due to low temperature, low dose neutron irradiation". In: *Journal of Nuclear Materials* 340.2 (2005), pp. 187–202.

[36] J.-P. Crocombette and L. Proville. "Thermal conductivity degradation induced by point defects in irradiated silicon carbide". In: *Applied Physics Letters* 98.19 (2011), p. 191905.

[37] M. Qin, S. Middleburgh, M. Cooper, M. Rushton, M. Puide, E. Kuo, R. Grimes, and G. Lumpkin. "Thermal conductivity variation in uranium dioxide with gadolinia additions". In: *Journal of Nuclear Materials* 540 (2020), p. 152258.

[38] J. Fourier. *The analytical theory of heat*. Cambridge University Press, 1878.

[39] F. P. Incropera, D. P. Dewitt, T. L. Bergman, and A. S. Lavine. *Fundamentals of Heat and Mass Transfer*. 6th ed. John Wiley & Sons, 2007.

[40] W. D. Callister Jr. and D. G. Rethwisch. *Materials Science and Engineering: An Introduction*. 10th ed. John Wiley & Sons, 2018.

[41] C. Kittel. *Introduction to Solid State Physics*. 8th ed. John Wiley & Sons, 2005.

[42] J. R. Hook and H. E. Hall. *Solid State Physics*. 2nd ed. John Wiley & Sons, 1991.

[43] H. Rosenberg. *Low Temperature Solid State Physics: Some Selected Topics*. Clarendon Press, 1965.

[44] Y. Ding and B. Xiao. "Anisotropic elasticity, sound velocity and thermal conductivity of TiO_2 polymorphs from first principles calculations". In: *Computational Materials Science* 82 (2014), pp. 202–218.

[45] Z. Wan, Y. Yu, H. F. Zhang, T. Gao, X. J. Chen, and C. J. Xiao. "First-principles study of electronic, dynamical and thermodynamic properties of Li2TiO3". In: *The European Physical Journal B* 85.6 (2012).

[46] N. Roux, S. Tanaka, C. Johnson, and R. Verrall. "Ceramic breeder material development". In: *Fusion Engineering and Design* 41.1 (1998), pp. 31–38.

[47] J. van der Laan, H. Kawamura, N. Roux, and D. Yamaki. "Ceramic breeder research and development: progress and focus". In: *Journal of Nuclear Materials* 283-287 (2000). 9th Int. Conf. on Fusion Reactor Materials, pp. 99–109.

[48] C. Johnson and G. Hollenberg. "Recent advances in the development of solid breeder blanket materials". In: *Journal of Nuclear Materials* 123.1 (1984), pp. 871–881.

[49] I. Palermo, J. Gómez-Ros, G. Veredas, J. Catalán, F. Ogando, J. Sanz, and L. Sedano. "Preliminary neutronic assessment of a helium-cooled Li_8PbO_6 breeding blanket design for DEMO". In: *Fusion Engineering and Design* 87.2 (2012), pp. 195–199.

[50] R. Knitter, P. Chaudhuri, Y. Feng, T. Hoshino, and I.-K. Yu. "Recent developments of solid breeder fabrication". In: *Journal of Nuclear Materials* 442.1, Supplement 1 (2013). Fifteenth International Conference on Fusion Reactor Materials, S420–S424.

[51] M. Zmitko, Y. Poitevin, L. Boccaccini, J.-F. Salavy, R. Knitter, A. Möslang, A. Magielsen, J. Hegeman, and R. Lässer. "Development and qualification of functional materials for the EU Test Blanket Modules: Strategy and R&D activities". In: *Journal of Nuclear Materials* 417.1 (2011). Proceedings of ICFRM-14, pp. 678–683.

[52] S. Konishi, M. Enoeda, M. Nakamichi, T. Hoshino, A. Ying, S. Sharafat, and S. Smolentsev. "Functional materials for breeding blankets—status and developments". In: *Nuclear Fusion* 57.9 (2017), p. 092014.

[53] C. Alvani, S. Casadio, A. D. Bartolomeo, J. D. Lulewicz, and N. Roux. "Li_2TiO_3 pebbles reprocessing, recovery of ^6Li as Li_2CO_3". In: *Journal of Nuclear Materials* 307-311 (2002), pp. 837–841.

[54] L. Giancarli, V. Barabash, D. Campbell, S. Chiocchio, J.-J. Cordier, A. Dammann, G. Dell'Orco, J. Elbez-Uzan, J. Fourneron, J. Friconneau, M. Gasparotto, M. Iseli, C.-Y. Jung, B.-Y. Kim, D. Lazarov, B. Levesy, M. Loughlin, M. Merola, J.-C. Nevière, R. Pascal, W. Ring, I. Schneiderova, S. Willms, A. Siarras, W. Shu, J. Snipes, and J. van der Laan. "Progress and

challenges of the ITER TBM Program from the IO perspective". In: *Fusion Engineering and Design* 109-111 (2016). Proceedings of the 12th International Symposium on Fusion Nuclear Technology-12 (ISFNT-12), pp. 1491–1497.

[55] R. Knitter, M. Kolb, U. Kaufmann, and A. Goraieb. "Fabrication of modified lithium orthosilicate pebbles by addition of titania". In: *Journal of Nuclear Materials* 442.1, Supplement 1 (2013). Fifteenth International Conference on Fusion Reactor Materials, S433–S436.

[56] O. Leys, J. M. Leys, and R. Knitter. "Current status and future perspectives of EU ceramic breeder development". In: *Fusion Engineering and Design* 164 (2021), p. 112171.

[57] G. Zhou, F. A. Hernández, P. Pereslavtsev, B. Kiss, A. Retheesh, L. Maqueda, and J. H. Park. "The European DEMO Helium Cooled Pebble Bed Breeding Blanket: Design Status at the Conclusion of the Pre-Concept Design Phase". In: *Energies* 16.14 (2023).

[58] G. Izquierdo and A. R. West. "Phase equilibria in the system Li_2O-TiO_2". In: *Materials Research Bulletin* 15.11 (1980), pp. 1655–1660.

[59] J. C. Mikkelsen Jr. "Pseudobinary Phase Relations of $Li_2Ti_3O_7$". In: *Journal of the American Ceramic Society* 63.5-6 (1980), pp. 331–335.

[60] H. Kleykamp. "Phase equilibria in the Li–Ti–O system and physical properties of Li_2TiO_3". In: *Fusion Engineering and Design* 61-62 (2002), pp. 361–366.

[61] M. Kolb, K. Mukai, R. Knitter, and T. Hoshino. "Li_4SiO_4 based breeder ceramics with Li_2TiO_3, $LiAlO_2$ and $LiXLaYTiO_3$ additions, part I: Fabrication". In: *Fusion Engineering and Design* 115 (2017), pp. 39–48.

[62] B. Konar, M.-A. Van Ende, and I.-H. Jung. "Critical evaluation and thermodynamic optimization of the Li-O, and Li_2O-SiO_2 systems". In: *Journal of the European Ceramic Society* 37.5 (2017), pp. 2189–2207.

[63] K. Kataoka, Y. Takahashi, N. Kijima, H. Nagai, J. Akimoto, Y. Idemoto, and K. Ohshima. "Crystal growth and structure refinement of monoclinic Li_2TiO_3". In: *Materials Research Bulletin* 44.1 (2009), pp. 168–172.

[64] G. Lang. "Die Kristallstruktur einiger Vertreter der Verbindungs-klasse $Me^I_2Me^{IV}O_3$ als Beitrag zur Aufklrung der Ordnungsphase von Li_2TiO_3". In: *Zeitschrift für anorganische und allgemeine Chemie* 276 (1954), pp. 77–94.

[65] K. Azuma, C. Dover, D. C. Grinter, R. Grau-Crespo, N. Almora-Barrios, G. Thornton, T. Oda, and S. Tanaka. "Scanning Tunneling Microscopy and Molecular Dynamics Study of the Li_2TiO_3 (001) Surface". In: *The Journal of Physical Chemistry C* 117.10 (2013), pp. 5126–5131.

[66] S. T. Murphy, P. Zeller, A. Chartier, and L. Van Brutzel. "Atomistic Simulation of the Structural, Thermodynamic, and Elastic Properties of Li_2TiO_3". In: *The Journal of Physical Chemistry C* 115.44 (2011), pp. 21874–21881.

[67] S. T. Murphy and N. D. M. Hine. "Point Defects and Non-stoichiometry in Li_2TiO_3". In: *Chemistry of Materials* 26.4 (2014), pp. 1629–1638.

[68] M. Kobayashi, K. Toda, Y. Oya, and K. Okuno. "Dependency of irradiation damage density on tritium migration behaviors in Li_2TiO_3". In: *Journal of Nuclear Materials* 447.1 (2014), pp. 1–8.

[69] M. Kobayashi, Y. Oya, K. Munakata, and K. Okuno. "Developing a tritium release model for Li_2TiO_3 with irradiation-induced defects". In: *Journal of Nuclear Materials* 458 (2015), pp. 22–28.

[70] M. Vijayakumar, S. Kerisit, Z. Yang, G. L. Graff, J. Liu, J. A. Sears, S. D. Burton, K. M. Rosso, and J. Hu. "Combined 6,7 Li NMR and Molecular Dynamics Study of Li Diffusion in Li_2TiO_3". In: *The Journal of Physical Chemistry C* 113.46 (2009), pp. 20108–20116.

[71] S. T. Murphy. "Tritium solubility in Li_2TiO_3 from first-principles simulations". In: *Journal of Physical Chemistry C* 118 (2014), pp. 29525–29532.

[72] M. Suhail, B. Puliyeri, P. Chaudhuri, R. Annabattula, and N. Swaminathan. "Molecular Dynamics Simulation of Primary Damage in β-Li_2TiO_3". In: *Fusion Engineering and Design* 136 (2018). Special Issue: Proceedings of the 13th International Symposium on Fusion Nuclear Technology (ISFNT-13), pp. 914–919.

[73] C. Wong, S. Malang, S. Nishio, R. Raffray, and A. Sagara. "Advanced high performance solid wall blanket concepts". In: *Fusion Engineering and Design* 61-62 (2002), pp. 283–293.

[74] N. Roux, G. Hollenberg, C. Johnson, K. Noda, and R. Verrall. "Summary of experimental results for ceramic breeder materials". In: *Fusion Engineering and Design* 27 (1995). Proceedings of the Third International Symposium on Fusion Nuclear Technology, pp. 154–166.

[75] J.-D. Lulewicz and N. Roux. "First results of the investigation of Li_2ZrO_3 and Li_2TiO_3 pebbles". In: *Fusion Engineering and Design* 39-40 (1998), pp. 745–750.

[76] K. Xu, C. Qi, and B. Wang. "Recent Progress in Research of Solid Tritium Breeder Materials Li_2TiO_3: A Review". In: *Coatings* 12.8 (2022).

[77] J. van der Laan, H. Kawamura, N. Roux, and D. Yamaki. "Ceramic breeder research and development: progress and focus". In: *Journal of Nuclear Materials* 283-287 (2000). 9th Int. Conf. on Fusion Reactor Materials, pp. 99–109.

[78] D. Mandal, M. Shenoi, and S. Ghosh. "Synthesis & fabrication of lithium-titanate pebbles for ITER breeding blanket by solid state reaction & spherodization". In: *Fusion Engineering and Design* 85.5 (2010), pp. 819–823.

[79] Y.-H. Park, K.-M. Min, S. Cho, M.-Y. Ahn, and Y.-M. Lee. "Li_2TiO_3 powder synthesis by solid-state reaction and pebble fabrication for tritium breeding material". In: *Fusion Engineering and Design* 124 (2017). Proceedings of the

29th Symposium on Fusion Technology (SOFT-29) Prague, Czech Republic, September 5-9, 2016, pp. 730–734.

[80] B. M. Tripathi, T. Mohanty, D. Prakash, A. Tyagi, and P. Sinha. "Monoclinic β-Li_2TiO_3 nanocrystalline particles employing novel urea assisted solid state route: Synthesis, characterization and sintering behavior". In: *Journal of Nuclear Materials* 490 (2017), pp. 167–173.

[81] H. Guo, H. Wang, R. Chen, Z. Huang, Y. Gong, Y. Zeng, Y. Jiang, J. Qi, Q. Shi, and T. Lu. "Low-cost fabrication of Li_2TiO_3 tritium breeding ceramic pebbles via low-temperature solid-state precursor method". In: *Ceramics International* 45.14 (2019), pp. 17114–17119.

[82] Z. Wen, X. Wu, X. Xu, J. Lin, and Z. Gu. "Research on the preparation of ceramic tritium breeders in SICCAS". In: *Fusion Engineering and Design* 85.7 (2010). Proceedings of the Ninth International Symposium on Fusion Nuclear Technology, pp. 1551–1555.

[83] A. Shrivastava, T. Kumar, R. Shukla, and P. Chaudhuri. "Li_2TiO_3 pebble fabrication by freeze granulation & freeze drying method". In: *Fusion Engineering and Design* 168 (2021), p. 112411.

[84] D. Mandal, N. Ghuge, and M. Jadeja. "Development and demonstration of a semi-automatic system for the bulk production of lithium titanate (Li_2TiO_3) pebbles by solid state reaction process (SSRP)". In: *Fusion Engineering and Design* 159 (2020), p. 111871.

[85] I. Carbajal-Ramos, J. Zacur, J. Andrade-Gamboa, N. Palacios, M. Rodriguez, and F. Gennari. "Physicochemical stability under inert and reductive atmospheres of Li_2TiO_3 produced from Li_2CO_3 obtained from Argentinean brines". In: *Fusion Engineering and Design* 130 (2018), pp. 148–154.

[86] X. Wu, Z. Wen, B. Lin, and X. Xu. "Sol–gel synthesis and sintering of nano-size Li_2TiO_3 powder". In: *Materials Letters* 62.6 (2008), pp. 837–839.

[87] X. Wu, Z. Wen, J. Han, X. Xu, and B. Lin. "Fabrication of Li_2TiO_3 pebbles by water-based sol–gel method". In: *Fusion Engineering and Design* 83.1 (2008), pp. 112–116.

[88] X. Wu, Z. Wen, X. Xu, J. Han, and B. Lin. "Fabrication and improvement of the density of Li_2TiO_3 pebbles by the optimization of a sol–gel method". In: *Journal of Nuclear Materials* 393.1 (2009), pp. 186–191.

[89] T. Vittal Rao, Y. Bamankar, S. Mukerjee, and S. Aggarwal. "Preparation and characterization of Li_2TiO_3 pebbles by internal gelation sol–gel process". In: *Journal of Nuclear Materials* 426.1 (2012), pp. 102–108.

[90] A. Deptuła, M. Brykała, W. Łada, T. Olczak, B. Sartowska, A. Chmielewski, D. Wawszczak, and C. Alvani. "Preparation of spherical particles of Li_2TiO_3 (with diameters below 100 µm) by sol–gel process". In: *Fusion Engineering and Design* 84.2 (2009). Proceeding of the 25th Symposium on Fusion Technology, pp. 681–684.

[91] G. Tan, X. Hu, S. Wang, X. Yang, Y. Li, Z. Yang, and Y. Zhang. "A process for fabrication of Li_2TiO_3 ceramic pebbles with high mechanical properties via non-hydrolytic sol-gel method". In: *Ceramics International* 46.17 (2020), pp. 27686–27694.

[92] W. Zhang, Q. Zhou, L. Xue, and Y. Yan. "Fabrication of Li_2TiO_3 pebbles with small grain size via hydrothermal and improved dry-rolling methods". In: *Journal of Nuclear Materials* 464 (2015), pp. 389–393.

[93] W. Liu, J. Di, W. Zhang, L. Xue, and Y. Yan. "Influence of titanium sources on the microstructures and properties of Li_2TiO_3 ceramics prepared by hydrothermal method". In: *Fusion Engineering and Design* 138 (2019), pp. 364–371.

[94] Q. Zhou, Y. Mou, X. Ma, L. Xue, and Y. Yan. "Effect of fuel-to-oxidizer ratios on combustion mode and microstructure of Li_2TiO_3 nanoscale powders". In: *Journal of the European Ceramic Society* 34.3 (2014), pp. 801–807.

[95] C. Jung, J. Park, S. Oh, H. Park, Y. Kim, D. Kim, and J. Kim. "Synthesis of Li_2TiO_3 ceramic breeder powders by the combustion process". In: *Journal of Nuclear Materials* 253.1 (1998), pp. 203–212.

[96] A. Sinha, S. Nair, and P. Sinha. "Single step synthesis of Li_2TiO_3 powder". In: *Journal of Nuclear Materials* 399.2 (2010), pp. 162–166.

[97] A. Shrivastava, M. Makwana, P. Chaudhuri, and E. Rajendrakumar. "Preparation and Characterization of the Lithium Metatitanate Ceramics by Solution-Combustion Method for Indian LLCB TBM". In: *Fusion Science and Technology* 65.2 (2014), pp. 319–324.

[98] J. Lulewicz and N. Roux. "Fabrication of Li_2TiO_3 pebbles by the extrusion–spheronisation–sintering process". In: *Journal of Nuclear Materials* 307-311 (2002), pp. 803–806.

[99] C.-L. Yu, W. Liu, L.-T. Yang, D.-Y. Wang, K. Wu, Z.-P. Zhang, X.-F. Wang, and K. Yanagisawa. "Additives affecting properties of β-Li_2TiO_3 pebbles in a modified indirect wet chemistry process". In: *Journal of Nuclear Materials* 480 (2016), pp. 310–313.

[100] T. Hoshino, K. Kenichi, Y. Natori, F. Oikawa, N. Nakano, M. Nakamura, K. Sasaki, A. Suzuki, T. Terai, and K. Tatenuma. "Development of advanced tritium breeding material with added lithium for ITER-TBM". In: *Journal of Nuclear Materials* 417 (2011), pp. 684–687.

[101] S.-J. Lee, Y.-H. Park, and M.-W. Yu. "Fabrication of Li_2TiO_3 pebbles by a freeze drying process". In: *Fusion Engineering and Design* 88.11 (2013), pp. 3091–3094.

[102] E. J. Maginn and J. R. Elliott. "Historical Perspective and Current Outlook for Molecular Dynamics As a Chemical Engineering Tool". In: *Industrial & Engineering Chemistry Research* 49.7 (2010), pp. 3059–3078.

[103] A. Rahman. "Correlations in the Motion of Atoms in Liquid Argon". In: *Phys. Rev.* 136 (1964), A405–a411.

[104] A. P. Thompson, H. M. Aktulga, R. Berger, D. S. Bolintineanu, W. M. Brown, P. S. Crozier, P. J. in 't Veld, A. Kohlmeyer, S. G. Moore, T. D. Nguyen, R. Shan, M. J. Stevens, J. Tranchida, C. Trott, and S. J. Plimpton. "LAMMPS - a flexible simulation tool for particle-based materials modeling at the atomic, meso, and continuum scales". In: *Computer Physics Communications* 271 (2022), p. 108171.

[105] P. Hirel. "Atomsk: A tool for manipulating and converting atomic data files". In: *Computer Physics Communications* 197 (2015), pp. 212–219.

[106] M. E. Tuckerman and G. J. Martyna. "Understanding Modern Molecular Dynamics: Techniques and Applications". In: *Journal of Physical Chemistry B* 104 (1999), pp. 159–178.

[107] T. Apostolova, E. Artacho, F. Cleri, M. Cotelo, M. L. Crespillo, F. D. Pieve, V. Dimitriou, F. Djurabekova, D. M. Duffy, G. García, M. García-Lechuga, B. Gu, T. Jarrin, E. Kaselouris, J. Kohanoff, G. Koundourakis, N. Koval, V. Lipp, L. Martin-Samos, N. Medvedev, A. Molina-Sánchez, D. Muñoz-Santiburcio, S. T. Murphy, K. Nordlund, E. Oliva, J. Olivares, N. A. Papadogiannis, A. Redondo-Cubero, A. R. de Mena, A. E. Sand, D. Sangalli, J. Siegel, A. V. Solov'yov, I. A. Solov'yov, J. Teunissen, E. Vázquez, A. V. Verkhovtsev, S. Viñals, and M. D. Ynsa. *Tools for investigating electronic excitation: experiment and multi-scale modelling*. Universidad Politécnica de Madrid. Instituto de Fusión Nuclear Guillermo Velarde, 2021.

[108] L. Verlet. “Computer "Experiments" on Classical Fluids. I. Thermodynamical Properties of Lennard-Jones Molecules”. In: *Phys. Rev.* 159 (1967), pp. 98–103.

[109] W. C. Swope, H. C. Andersen, P. H. Berens, and K. R. Wilson. “A computer simulation method for the calculation of equilibrium constants for the formation of physical clusters of molecules: Application to small water clusters”. In: *The Journal of Chemical Physics* 76.1 (1982), pp. 637–649.

[110] S. Kim. “Issues on the Choice of a Proper Time Step in Molecular Dynamics”. In: *Physics Procedia* 53 (2014). 26th Annual CSP Workshop on “Recent Developments in Computer Simulation Studies in Condensed Matter Physics”, CSP 2013, pp. 60–62.

[111] J. W. Gibbs. *Elementary principles in statistical mechanics*. Charles Scribner’s Sons, 1902.

[112] S. Nosé. “A unified formulation of the constant temperature molecular dynamics methods”. In: *The Journal of Chemical Physics* 81 (1984), pp. 511–519.

[113] W. G. Hoover. “Canonical dynamics: Equilibrium phase-space distributions”. In: *Phys. Rev. A* 31 (1985), pp. 1695–1697.

[114] R. LeSar. *Introduction to computational materials science: fundamentals to applications*. Cambridge University Press, 2013.

[115] P. P. Ewald. “Die Berechnung optischer und elektrostatischer Gitterpotentiale”. In: *Annalen der Physik* 369.3 (1921), pp. 253–287.

[116] T. Darden, D. York, and L. Pedersen. “Particle mesh Ewald: An N·log(N) method for Ewald sums in large systems”. In: *The Journal of Chemical Physics* 98.12 (1993), pp. 10089–10092.

[117] R. W. Hockney and J. W. Eastwood. *Computer simulation using particles*. Bristol: Hilger, 1988, 1988.

[118] D. Wolf, P. Keblinski, S. R. Phillpot, and J. Eggebrecht. "Exact method for the simulation of Coulombic systems by spherically truncated, pairwise r^{-1} summation". In: *The Journal of Chemical Physics* 110.17 (1999), pp. 8254–8282.

[119] M. Born and J. E. Mayer. "Zur Gittertheorie der Ionenkristalle". In: *Zeitschrift für Physik* 75 (1932), pp. 1–18.

[120] R. A. Buckingham and J. E. Lennard-Jones. "The classical equation of state of gaseous helium, neon and argon". In: *Proceedings of the Royal Society of London. Series A. Mathematical and Physical Sciences* 168.933 (1938), pp. 264–283.

[121] J. E. Lennard-Jones. "Cohesion". In: *Proceedings of the Physical Society* 43.5 (1931), pp. 461–482.

[122] J. E. Jones and S. Chapman. "On the determination of molecular fields. –I. From the variation of the viscosity of a gas with temperature". In: *Proceedings of the Royal Society of London. Series A, Containing Papers of a Mathematical and Physical Character* 106.738 (1924), pp. 441–462.

[123] J. E. Jones and S. Chapman. "On the determination of molecular fields. –II. From the equation of state of a gas". In: *Proceedings of the Royal Society of London. Series A, Containing Papers of a Mathematical and Physical Character* 106.738 (1924), pp. 463–477.

[124] M. Matsui and M. Akaogi. "Molecular Dynamics Simulation of the Structural and Physical Properties of the Four Polymorphs of TiO_2". In: *Molecular Simulation* 6.4-6 (1991), pp. 239–244.

[125] B. G. Dick and A. W. Overhauser. "Theory of the Dielectric Constants of Alkali Halide Crystals". In: *Phys. Rev.* 112 (1958), pp. 90–103.

[126] N. Kuganathan, A. Kordatos, M. Fitzpatrick, R. Vovk, and A. Chroneos. "Defect process and lithium diffusion in Li_2TiO_3". In: *Solid State Ionics* 327 (2018), pp. 93–98.

[127] F. Müller-Plathe. "A simple nonequilibrium molecular dynamics method for calculating the thermal conductivity". In: *The Journal of Chemical Physics* 106.14 (1997), pp. 6082–6085.

[128] D. W. Hahn. *Heat conduction*. eng. 3rd ed. Hoboken, N.J.: Wiley, 2012.

[129] H. Casimir. "Note on the conduction of heat in crystals". In: *Physica* 5.6 (1938), pp. 495–500.

[130] C. Oligschleger and J. C. Schön. "Simulation of thermal conductivity and heat transport in solids". In: *Phys. Rev. B* 59 (1999), pp. 4125–4133.

[131] P. K. Schelling, S. R. Phillpot, and P. Keblinski. "Comparison of atomic-level simulation methods for computing thermal conductivity". In: *Phys. Rev. B* 65 (2002), p. 144306.

[132] W. Jost. "Diffusion and Electrolytic Conduction in Crystals (Ionic Semiconductors)". In: *The Journal of Chemical Physics* 1.7 (1933), pp. 466–475.

[133] N. F. Mott and M. J. Littleton. "Conduction in polar crystals. I. Electrolytic conduction in solid salts". In: *Transactions of the Faraday Society* 34 (1938), pp. 485–499.

[134] M. J. Rushton. "Simulations of Glass and Ceramic Systems for Nuclear Waste Applications". PhD thesis. Imperial College London, 2006.

[135] M. Sanjeev, M. R. Gilbert, and S. T. Murphy. "Anisotropic thermal conductivity in Li_2TiO_3 ceramic breeder materials". In: *Fusion Engineering and Design* 170 (2021), p. 112710.

[136] J. Davis and A. Haasz. "Thermal diffusivity/conductivity of AECL Li_2TiO_3 ceramic". In: *Journal of Nuclear Materials* 232.1 (1996), pp. 65–68.

[137] S. Saito, K. Tsuchiya, H. Kawamura, T. Terai, and S. Tanaka. "Density dependence on thermal properties of Li_2TiO_3 pellets". In: *Journal of Nuclear Materials* 253.1 (1998), pp. 213–218.

[138] T. Hoshino, M. Dokiya, T. Terai, Y. Takahashi, and M. Yamawaki. "Non-stoichiometry and its effect on thermal properties of Li_2TiO_3". In: *Fusion Engineering and Design* 61-62 (2002), pp. 353–360.

[139] M. Zhao, X. Ren, and W. Pan. "Mechanical and thermal properties of simultaneously substituted pyrochlore compounds $(Ca_2Nb_2O_7)_x(Gd_2Zr_2O_7)_{1-x}$". In: *Journal of the European Ceramic Society* 35.3 (2015), pp. 1055–1061.

[140] G. Samolyuk and P. Edmondson. "First principles study of the stability and thermal conductivity of novel Li-Be hybrid ceramics". In: *Acta Materialia* 215 (2021), p. 117052.

[141] J. Reimann and S. Hermsmeyer. "Thermal conductivity of compressed ceramic breeder pebble beds". In: *Fusion Engineering and Design* 61-62 (2002), pp. 345–351.

[142] M. Sanjeev, M. R. Gilbert, and S. T. Murphy. "Thermal conductivity of non-stoichiometric Li_2TiO_3". In: *Journal of Nuclear Materials* 572 (2022), p. 154037.

[143] T. Hoshino. "Pebble fabrication of super advanced tritium breeders using a solid solution of $Li_{2+x}TiO_{3+y}$ with Li_2ZrO_3". In: *Nuclear Materials and Energy* 9 (2016), pp. 221–226.

[144] H. Guo, H. Wang, R. Chen, Y. Gong, M. Yang, D. Ye, Y. Shi, Q. Shi, and T. Lu. "Characterization of Li-rich Li_2TiO_3 ceramic pebbles prepared by rolling method sintered in air and vacuum". In: *Journal of Nuclear Materials* 546 (2021), p. 152786.

[145] S. Sato, T. Nishitani, and C. Konno. "Effects of lithium burn-up on TBR in DEMO reactor SlimCS". In: *Fusion Engineering and Design* 87.5 (2012). Tenth International Symposium on Fusion Nuclear Technology (ISFNT-10), pp. 680–683.

[146] Y.-z. Hao, Q.-l. Zhang, J. Zhang, C.-r. Xin, and H. Yang. "Enhanced sintering characteristics and microwave dielectric properties of Li_2TiO_3 due to nano-size and nonstoichiometry effect". In: *J. Mater. Chem.* 22 (2012), pp. 23885–23892.

[147] J. Bian and Y. Dong. "Sintering behavior, microstructure and microwave dielectric properties of $Li_{2+x}TiO_3$ ($0 \leq x \leq 0.2$)". In: *Materials Science and Engineering: B* 176.2 (2011), pp. 147–151.

[148] F. Kröger and H. Vink. "Relations between the Concentrations of Imperfections in Crystalline Solids". In: ed. by F. Seitz and D. Turnbull. Vol. 3. Solid State Physics. Academic Press, 1956, pp. 307–435.

[149] K. Mukai, K. Sasaki, T. Hashimoto, A. Suzuki, T. Hoshino, and T. Terai. "Effect of Li/Ti ratio on microstructure and thermal diffusivity of lithium titanate for solid breeding material". In: *Fusion Engineering and Design* 86.9 (2011). Proceedings of the 26th Symposium of Fusion Technology (SOFT-26), pp. 2643–2646.

[150] C.-L. Yu, D.-P. Gao, and K. Yanagisawa. "Vacancy and Substitution Defects of β-Li_2TiO_3 Prepared by Hydrothermal Method". In: *Chemistry Letters* 43.3 (2014), pp. 369–370.

[151] Ģ. Vītiņš, G. Ķizāne, A. Lūsis, and J. Tīliks. "Electrical conductivity studies in the system Li_2TiO_3-$Li_{1.33}Ti_{1.67}O_4$". In: *Journal of Solid State Electrochemistry* 6.5 (2002), pp. 311–319.

[152] N. Roux. In: *Proceeding of Sixth International Workshop on Ceramic Breeder Blanket Interactions, 22–24 October 1997, Mito City, Japan* (1998), p. 139.

[153] J. D. Gale and A. L. Rohl. "The General Utility Lattice Program (GULP)". In: *Molecular Simulation* 29.5 (2003), pp. 291–341.

[154] J. Ball, S. Murphy, R. Grimes, D. Bacorisen, R. Smith, B. Uberuaga, and K. Sickafus. "Defect processes in $MgAl_2O_4$ spinel". In: *Solid State Sciences* 10.6 (2008), pp. 717–724.

[155] IUPAC. *Compendium of Chemical Terminology, 3rd ed.* Online version 3.0.1, 2019. International Union of Pure and Applied Chemistry, 2006.

[156] A. F. Ismail, K. C. Khulbe, and T. Matsuura. *Gas Separation Membranes: Polymeric and Inorganic*. Springer, 2015.

[157] A. Shrivastava, R. Shukla, and P. Chaudhuri. "Effect of porosity on thermal conductivity of Li_2TiO_3 ceramic compact". In: *Fusion Engineering and Design* 166 (2021), p. 112318.

[158] M. Sanjeev, M. R. Gilbert, and S. T. Murphy. "Molecular dynamics simulations of the effect of porosity on heat transfer in Li_2TiO_3". In: *Fusion Engineering and Design* 202 (2024), p. 114344.

[159] A. Chernatynskiy, C. Flint, S. B. Sinnott, and S. R. Phillpot. "Critical assessment of UO_2 classical potentials for thermal conductivity calculations". In: *Journal of Materials Science* 47.21 (2012), pp. 7693–7702.

[160] R. K. Behera and C. S. Deo. "Atomistic models to investigate thorium dioxide (ThO_2)". In: *Journal of Physics: Condensed Matter* 24.21 (2012), p. 215405.

[161] W. K. Kim, J. H. Shim, and M. Kaviany. "UO_2 bicrystal phonon grain-boundary resistance by molecular dynamics and predictive models". In: *International Journal of Heat and Mass Transfer* 100 (2016), pp. 243–249.

[162] Y. Shen, T. Gao, X. Tian, X. Chen, C. Xiao, and T. Lu. "Constructing three-dimensional (3D) nanocrystalline models of Li_4SiO_4 for numerical modeling and simulation". In: *Scientific Reports* 5.1 (2015).

[163] H. Chan, B. Narayanan, M. J. Cherukara, F. G. Sen, K. Sasikumar, S. K. Gray, M. K. Y. Chan, and S. K. R. S. Sankaranarayanan. "Machine Learning Classical Interatomic Potentials for Molecular Dynamics from First-Principles Training Data". In: *The Journal of Physical Chemistry C* 123.12 (2019), pp. 6941–6957.